

Jagiellonian University  
Faculty of Physics, Astronomy and Applied Computer Science

---

**EVOLUTION OF MAGNETIC FIELDS IN DWARF GALAXIES**  
NUMERICAL SIMULATIONS OF COSMIC-RAY DRIVEN DYNAMO

by

Hubert Siejkowski

A thesis, written under the supervision of  
prof. dr hab. Katarzyna Otmianowska-Mazur,  
submitted to the Jagiellonian University  
for the degree of Doctor of Philosophy

Kraków 2012

*To my wife, for all her love, patience and support.*

*I thank my supervisor Katarzyna Otmianowska-Mazur for help, support and guidance, Marian Soida for many discussions and finding code bugs, Dominik Bomans for hospitality, and keeping me up to date with observations and helping to understand its implications for the modelling.*

## Abstract

Observations of Milky Way and many other galaxies reveal the magnetic field as an important component of the interstellar medium. The question of the origin of such strong magnetic fields has been investigated since many years. The most plausible explanation is due to the operation of a process called large scale magnetic dynamo. This process uses the turbulent kinetic energy driven by the supernovae explosion to twist and fold the magnetic field lines, and as a result the total flux increases. Due to the global differential rotation the newly created chaotic magnetic field is being regularised and contributes to the large scale magnetic field. The crucial parameters of this process is the angular velocity and the shape of the rotation curve, as well as the supernova rate.

This thesis are devoted to investigate the operation of the large scale dynamo in one of the smallest galaxies in the Universe. The dwarf galaxies are low mass objects, and therefore they rotates very slowly. This makes them very unfavourable place to host a dynamo action, but still in several dwarf galaxies strong magnetic fields are observed. Additionally this galaxies can be also seen as the local proxies of the high redshift building blocks of more massive galaxies according to the current paradigm of the hierarchical galaxy formation. Therefore investigation of the magnetic field evolution of dwarf galaxies not only can explain the current observations but as well can bring more light on the very young Universe, while the first galaxies were formed.

I present a 3D global-galactic model of a dwarf galaxy which consists of two gravitational components: the stars and the dark matter halo. To describe the halo potential two different models are use, namely the “modified isothermal sphere” and the purely phenomenological profile proposed by Burkert. The system is incorporated to the numerical code, which solves a set of MHD equations with an additional cosmic-ray component described in terms of the fluid approximation. The supernova are injected to the system by introducing a 3D Gaussian distribution into the CR fluid. The system initially have magnetic field set to zero and to seed the dynamo small magnetic dipoles are injected with the very first supernovae.

The results show that the final magnetic field depends strongly on the rotation speed. Only the fastest rotating models reach within 6 Gyr of simulation the equilibrium level between the magnetic field and thermal gas pressure. The final magnetic field is about few  $\mu\text{G}$  and the dominating component is the toroidal magnetic field while the vertical structures are very weak. The simulation results are compared with the observations of galaxies such as IC 10, NGC 1569, NGC 6682 and NGC 4449. The simulations of the cosmic ray driven dynamo in global model of dwarf galaxy show that the observed magnetic field can be explained in terms of this process.

# Contents

<b>Contents</b>	<b>i</b>
<b>List of Tables</b>	<b>iii</b>
<b>List of Figures</b>	<b>iv</b>
<b>1 Magnetic fields in the Universe</b>	<b>1</b>
<b>2 Galactic magnetism</b>	<b>4</b>
2.1 Observations of galactic magnetic fields . . . . .	4
2.1.1 Spiral, barred and flocculent galaxies . . . . .	6
2.1.2 Milky Way . . . . .	9
2.1.3 Elliptical galaxies . . . . .	10
2.2 Dwarf galaxies . . . . .	10
2.3 Magnetic dynamo . . . . .	13
2.3.1 Cosmic ray driven dynamo . . . . .	15
<b>3 Numerical model</b>	<b>17</b>
3.1 MHD equations . . . . .	17
3.2 Cosmic ray component . . . . .	17
3.3 Gravitational potential . . . . .	18
3.4 Supernovae . . . . .	19
3.5 Numerical code . . . . .	21
3.6 Initial conditions . . . . .	22
3.7 Model parameters and setups . . . . .	23
3.7.1 Reference models . . . . .	23
3.7.2 Supernovae modulation . . . . .	26
3.7.3 Temperature of the ISM . . . . .	26
<b>4 Results</b>	<b>28</b>
4.1 The ISM evolution . . . . .	28
4.2 Magnetic field evolution . . . . .	32

4.2.1	Dependence on the rotational velocity . . . . .	32
4.2.2	Dependence on the SN modulation . . . . .	41
4.2.3	Dependence on the speed of sound . . . . .	44
4.2.4	Polarization maps . . . . .	45
4.3	Pressure equilibrium . . . . .	51
<b>5</b>	<b>Discussion</b>	<b>53</b>
5.1	Cosmic ray driven dynamo in galaxies . . . . .	53
5.1.1	Growth rate of the magnetic field . . . . .	53
5.1.2	Modulation of the supernova rate . . . . .	55
5.1.3	Dark matter profile and the magnetic fields . . . . .	56
5.1.4	Equilibrium in the ISM . . . . .	57
5.1.5	Magnetic field structure . . . . .	57
5.2	Comparison between models and observations . . . . .	58
5.2.1	NGC 1569 . . . . .	60
5.2.2	NGC 4449 . . . . .	61
5.2.3	IC 10 and NGC 6822 . . . . .	62
<b>6</b>	<b>Conclusions</b>	<b>63</b>
<b>A</b>	<b>Star formation rate and supernova rate</b>	<b>65</b>
	<b>Bibliography</b>	<b>68</b>

# List of Tables

2.1	Characteristics of observed dwarf galaxies. . . . .	12
3.1	The summary of constant parameters of the dwarf galaxy model. . . . .	24
3.2	The summary of dwarf galaxy model parameters. . . . .	24
3.3	Parameters of the reference models. . . . .	25
3.4	Parameters of SNe modulation models. . . . .	27
4.1	Results for the reference models. . . . .	39
4.2	Results for models with different SN modulation. . . . .	44
4.3	Results for models with different speeds of sound. . . . .	48
A.1	Models of the Initial Mass Functions. . . . .	66

# List of Figures

2.1	Radio observations of M 51 and NGC 1097. . . . .	6
2.2	Radio observations of NGC 6946 and NGC 4414. . . . .	7
2.3	Radio observations of NGC 891 and NGC 5775. . . . .	7
2.4	Regular magnetic field in M 51 derived by fitting a model to observed polarization angles. . . . .	8
2.5	Magnetic field pattern in Milky Way. . . . .	9
2.6	Radio observations of NGC 4449 and NGC 1569. . . . .	11
2.7	Magnetic fields dependence on star formation rate and rotation velocity deduced from observations dwarfs. . . . .	13
2.8	Rotation curves of NGC 6822 and NGC 4449. . . . .	14
2.9	Schematic view of the possible magnetic field configurations in a galaxy. . . . .	15
3.1	Profiles of the gravitational potentials described by Kuzmin's disk, "modified isothermal sphere" and Burkert's profile. . . . .	20
3.2	A scheme of supernovae activity modulation. . . . .	21
3.3	Test of CR diffusion along inclined magnetic field in an uniform medium. . . . .	21
3.4	Test of CR diffusion in a stratified medium. . . . .	22
3.5	The rotation curves for the reference models. . . . .	25
4.1	Number of supernovae explosion in $xy$ plane summed over all simulation time for the model v40. . . . .	29
4.2	Rotation curves in $t = 4.14$ Gyr for the reference models. . . . .	30
4.3	Snapshots of the gas an velocity evolution in a dwarf galaxy. . . . .	31
4.4	Vertical distribution of the gas density in the model v40 for selected timesteps. . . . .	32
4.5	Snapshots of the evolution of the cosmic ray energy. . . . .	33
4.6	The evolution of the magnetic field for models with different rotation speed. . . . .	35
4.7	Snapshots of the evolution of the toroidal magnetic field for v40. . . . .	37
4.8	Snapshots of the magnetic field evolution in model v40. . . . .	38
4.9	Evolution of the magnetic field for model v20. . . . .	40
4.10	The evolution of the magnetic field for models with different rotation speeds and modulation times (MIS). . . . .	42

4.11	The evolution of the magnetic field for models with different rotation speeds and modulation times (Burkert). . . . .	43
4.12	The evolution of the magnetic field for models with different rotation speed and speed of sound for models v30, v30b and v40. . . . .	46
4.13	The evolution of the magnetic field for models with different rotation speed and speed of sound for models v50, v60 and v70. . . . .	47
4.14	Polarization maps for selected timesteps for the model v40. . . . .	49
4.15	Polarization maps for selected timesteps for the model v20. . . . .	50
4.16	Evolution of the pressure ratios in the galaxy for the reference models. . . . .	52
4.17	Evolution of the pressure ratios in the galaxy for the models with $\hat{c}_s = 5.8$ and $8.1 \text{ km s}^{-1}$ . . . . .	52
5.1	Dependence of the $e$ -folding times of azimuthal flux evolution on the different times of SNe frequency evolution. . . . .	55
5.2	Relation between the $\nu_{\text{rot}}$ and total magnetic field in the model after 6 Gyr. . .	59
A.1	Relation between $\Sigma\text{SFR}$ (an observed quantity) and the $f_{\text{SN}}$ (a parameter of the CR driven dynamo). . . . .	67

# Magnetic fields in the Universe

The history of studying the magnetism phenomena dates back to 1600 when an English physicist, William Gilbert<sup>1</sup> published his work called *De Magnete, Magneticisque Corporibus, et de Magno Magnete Tellure*<sup>2</sup>. In his work, Gilbert introduces the magnetism study as a one of the science areas and states that one of the celestial bodies, Earth, itself is a magnet. Nowadays we know that Earth not only has magnetic field on its surface, which helps us to distinguish the cardinal directions, but also the field extends to the outer space and forms a protective magnetosphere. In 1908 a great discovery was made: George Ellery Hale<sup>3</sup> showed that for many years observed sunspots are strongly magnetized (Hale 1908). This discovery was very important for two reasons: it elucidates the physical basis of solar cycle and this was also a first detection of magnetic fields outside the Earth. The following decades brought us observations and theoretical predictions of magnetic fields in other planets and stars, and many different objects like: pulsars, black holes, accretion disks, dust clouds, Milky Way, galaxies (Rüdiger & Hollerbach 2004), clusters (Ryu et al. 2012) and others. Today we know magnetic fields are ubiquitous in the Universe. They can be also found in many objects in different scales starting from meters and kilometres up to kiloparsecs and even megaparsecs.

The aim of investigating the magnetic field in astrophysical context is not only finding it in different objects, but also, and most important, to understand its influence on the physical processes and objects' evolution. In the case of our Earth, the magnetic field creates a protective magnetosphere against the solar wind and charged particles, which can be dangerous for the biological organism (Wei et al. 2012; Randall et al. 2005). On the Sun the magnetic field also plays an important role. Every 11 years the polarity of the magnetic field in the Sun is reversed (e.g. Foukal 2004). This phenomenon is responsible

---

<sup>1</sup>1544–1603, he was also a physician and natural philosopher

<sup>2</sup>On the Magnet and Magnetic Bodies, and on That Great Magnet the Earth

<sup>3</sup>1868–1938, an American solar astronomer

for the amount of radiation coming to the Earth and the mean temperature on it (e.g. Maunder Minimum, Eddy 1976). This is also related to the so called space weather<sup>4</sup>, which is important for the communication systems, satellites, human spaceflight and many more.

Magnetic fields play also an important role in more distant objects. It helps to lose the matter of angular momentum and as the result of this it speeds up the matter accretion or collapse (e.g. Joos et al. 2012). This process is important in a big class of objects, called accretion disks (Li 2003). Accretion disk is usually formed around a central compact object, like neutron star or black hole, and is formed out of the surrounding matter falling due to gravitational force on that object. However it is necessary to have some additional dynamics in the disk to lose the angular momentum, this can be done via magnetic field which help to drive turbulence (e.g. MRI, Balbus 2009). In this type of objects very often jets are formed, which are a very collimated streams of matter flowing out of the polar regions of the central object. The magnetic field seems to be responsible also for this collimation (Ouyed & Pudritz 1997a,b).

The problem with angular momentum transport is also an issue in the case of forming new object, like planets or stars. The molecular clouds, from which new objects are created, can more easily collapse with aid of the magnetic field (McKee & Ostriker 2007). It seems also that magnetic field rules the direction of matter condensation in galaxies and therefore influence the creation of new stellar birth places (Li & Henning 2011).

The magnetic field itself is dynamic and can evolve and change with time. It has some embedded properties like helicity conservation (Vishniac & Cho 2001) or it could be transformed by physical process e.g. reconnection. The reconnection is currently deeply investigated by many researcher groups. The model proposed by Sweet (1958) and Parker (1957) is too slow with respect to the observations (Priest & Forbes 2000) and Petschek (1964) description is not stable and needs anomalous viscosity (Biskamp 1993). The model proposed by Lazarian & Vishniac (1999) assumes that the reconnection region is turbulent, and therefore this can significantly speed up the process (Kowal et al. 2009). In the reconnection zone some part of the magnetic field can be transformed into heat and particle acceleration. Reconnection events can be seen in the Earth magnetosphere (Ashour-Abdalla et al. 2011), on the Sun (e.g. coronal mass ejections) and in the laboratory (Zweibel & Yamada 2009). It is believed that it also plays a role in different objects, e.g. blazars where it can cause so called mini jets (Nalewajko et al. 2011).

This short introduction shows only that magnetic fields are very important and ubiquitous component of the Universe. Its presents and impact on physical processes can not be neglected and should be deeply investigated. This thesis are dedicated to study one of the problem in astrophysical magnetic fields which is the galactic magnetism in the case of one of the smallest objects of this type called dwarf galaxies. In the next chapters

---

<sup>4</sup>e.g. <http://www.spaceweather.com>

I will describe the current knowledge of the galactic magnetism, the properties of dwarf galaxies and a brief view on the dynamo theory focusing on one of the model namely, on cosmic-ray driven dynamo. Then I introduce a numerical model of a dwarf galaxy, computational methods which were used to simulate the evolution of the model and finally I present the results and draw conclusions.

# Galactic magnetism

Galaxies are very fascinating objects to study, because of many different physical processes which occurs in them. The galaxy image in the visual part of the electromagnetic spectrum is dominated by the optical light produced by stars, which contributes mostly to the visible galactic mass. The stars creates a system of compact objects which are gravitationally bound and move through the galaxy almost collisionless. The most significant and mysterious contribution to the galactic mass is due to a dark matter (DM). The dark matter can only interact with the visible matter via the gravitational force and is responsible for creating a huge halo in which the galaxy is embedded (Navarro et al. 1996). The interstellar matter (ISM), which fills the space between the stars, is only a few percent of the total mass (Sparke & Gallagher 2007). The ISM consists of gas in ionic, atomic and molecular form, dust, and cosmic rays. The ionization degree of the ionized part of ISM is between 30 and 100% (Ferrière 2001). Together with a magnetic field the ionized ISM gas creates a perfect system to be modelled in terms of magnetohydrodynamics (MHD). The effective mean free path of interstellar gas particles is small enough and therefore the fluid approximation is valid in very broad range of conditions. From observations we know that ISM gas, cosmic rays and magnetic fields are in a pressure equilibrium (Boulares & Cox 1990). To build a proper model of a galaxy one need to take every component in to account.

## 2.1 Observations of galactic magnetic fields

Galactic magnetic fields can be observed mostly by using polarization methods. One of them is observation of polarized infrared radiation emitted by dust grains. These grains are elongated and can be aligned by the magnetic field perpendicular to field lines (Lazarian & Cho 2005). They can also polarize an optical emission coming from the background stars (Davis & Greenstein 1951). For very strong fields and relatively close objects

it is possible to detect Zeeman splitting of radio spectral lines. These three methods are applicable only for observation of the Milky Way's and near by galaxies magnetic fields. For distant objects, and our Galaxy too, one can use the fourth method, namely synchrotron emission.

In the galaxy there is lots of cosmic-ray electrons produced by supernovae explosions and jets in e.g. micro quasars (O'C. Drury 2012). They are spinning around the magnetic field lines almost with a speed of light and emit the synchrotron radiation (Rybicki & Lightman 1986). It can be observed mostly at broad range of radio frequencies, but some most energetic electrons can emit light in infrared or even in higher frequencies. The intensity of this radiation is related to the electron density and magnetic field component in the sky plane of the observed region (Kraus 1966). The synchrotron emission observed by a telescope in a completely regular field within its beam is polarized with a degree as high as 75% (Pacholczyk 1970). The regular magnetic field in galaxies can be generated by e.g. a dynamo process. Polarized emission can emerge also from anisotropic magnetic field regions formed in compression or shearing gas flow, where frequently the magnetic field direction is reversed by  $180^\circ$  scales smaller than beam size. Any deviation of ordered field orientation within the beam reduce the degree of polarization. Unpolarized synchrotron radiation is a sign of tangled field lines with random directions shaped by turbulent gas motions. In observations one should deal with a mixture of ordered and random field, therefore three components of magnetic field are distinguished: regular, anisotropic and random (Beck 2007). Together, the regular and anisotropic magnetic fields are considered as the ordered component. The polarized synchrotron emission gives only the information about the orientation of magnetic field lines, but not about their direction. To find the direction one should measure the Faraday rotation.

At short radio wavelengths the magnetic field orientation is just perpendicular to the observed synchrotron polarization. At longer wavelengths one need to consider the Faraday rotation. The Faraday effect causes a rotation of the plane of polarization which is linearly proportional to the component of the magnetic field in the direction of propagation (Longair 2010). The rotation angle increases with the plasma density, the strength of the component of the regular field along the line of sight and the square of the observation wavelength. If one combine observations at few wavelengths it is possible to derive the magnetic field component parallel to the line of sight. It is also possible to find the direction of the magnetic field, because fields directed towards us cause an anti-clockwise sense of rotation, fields directed away from us a clockwise rotation. In the case of ordered component of magnetic field the regular field do Faraday rotation, but the anisotropic do not (Beck 2007). Combining observations of polarization of synchrotron radiation and Faraday rotation measurements yields in fully three dimensional picture of the magnetic field.

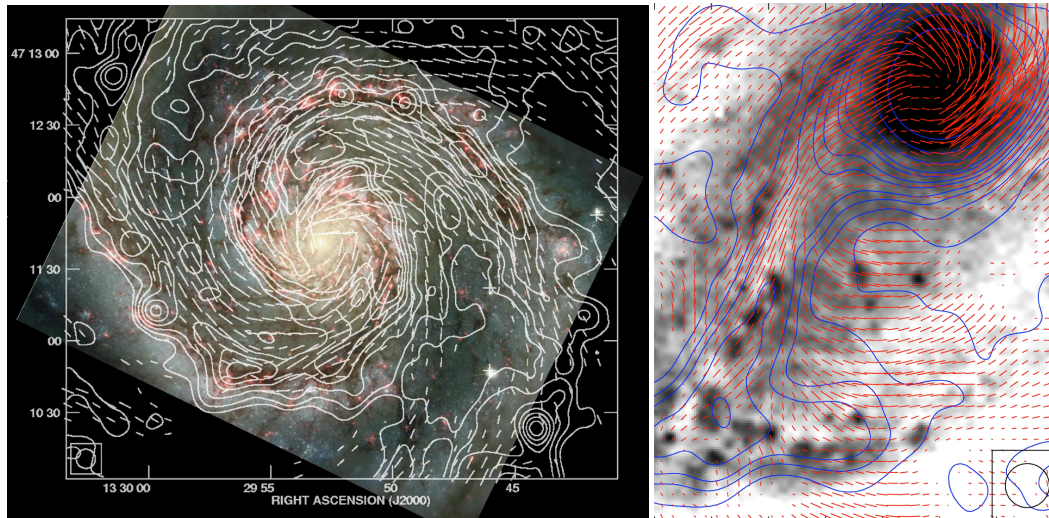


Figure 2.1: *Left panel:* Total radio emission and magnetic field vectors of M 51 observed at  $\lambda 6$  cm with VLA and Effelsberg and overlaid on a Hubble Space Telescope image [http://heritage.stsci.edu/2001/10, image credit: NASA and The Hubble Heritage Team (STScI/AURA)]. From Fletcher et al. (2011). *Right panel:* Total intensity contours and magnetic field vectors of NGC 1097 observed at  $\lambda 6.2$  cm with VLA. The length of the vectors is proportional to the polarized intensity. From Beck et al. (2005).

### 2.1.1 Spiral, barred and flocculent galaxies

Assuming the equipartition between energy densities of cosmic rays and magnetic fields it is possible to derive not only the orientation of the field but also its strength. The mean equipartition strength of the total field for a sample of 74 spiral galaxies (Niklas 1995; Beck 2005) is  $9 \mu\text{G}$ . In the case of grand-design spirals with massive star formation like M 51, M 83 and NGC 6946 the typical average strength is around  $15 \mu\text{G}$ . In prominent spiral arms the total equipartition field can be up to  $30 \mu\text{G}$ . The strongest magnetic field of value  $50\text{-}100 \mu\text{G}$  has been found in starburst galaxies like M 82 and *Antennae*, and in the starburst nuclear regions like in NGC 1097. For interacting galaxies the mean value of the total magnetic field strength is higher than this found in non-interacting objects. According to Drzazga et al. (2011) it is about  $15 \mu\text{G}$ . It is also worth notice that the mean value is changing with the interaction stage and is growing up to tens of  $\mu\text{G}$  and in the coalescence stage it drops rapidly to very low values.

The global structure of the magnetic fields in the disk plane forms almost in every galaxy a nice spiral pattern following the optical structure. However the most regular fields are slightly offset from the optical arms, like in M 51 (Fig. 2.1, left panel). It seems to be because the regular component is not resolved in the spiral arms due the tangling caused by increased turbulence. The turbulence is triggered by a star formation and supernova shock fronts which are mostly produced in the spiral arms. Similar patterns can be found in other objects like M 81 (Krause et al. 1989a) or M 83 (Beck 2005), where the

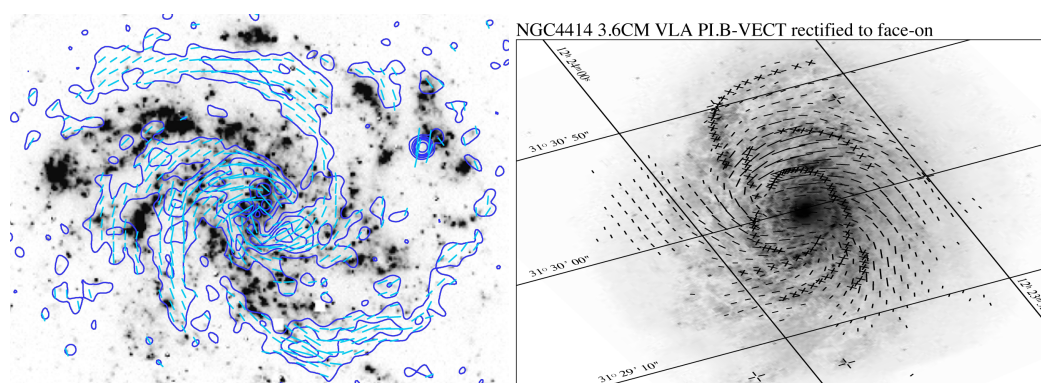


Figure 2.2: *Left panel:* Polarized synchrotron intensity (contours) and magnetic field orientation of NGC 6946 observed at  $\lambda 6.2$  cm with the VLA and combined with extended emission observed with the Effelsberg 100-m telescope (Beck & Hoernes 1996). The lengths of the vectors are proportional to the degree of polarization.  $H\alpha$  image in grey scale. *Right panel:* Magnetic field vectors derived from VLA observations of NGC 4414 overlaid on optical image from HST, both rectified to face-on view (Soida et al. 2002).

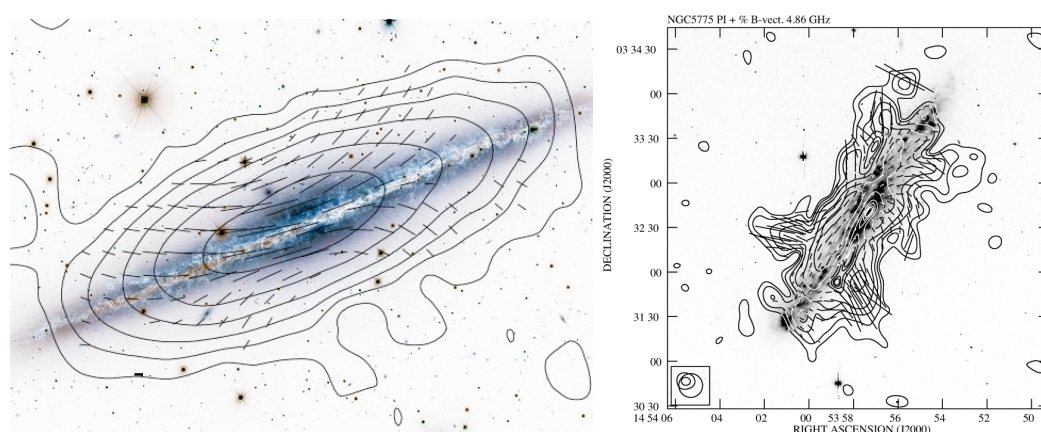


Figure 2.3: *Left panel:* Radio observations of galaxy NGC 891 at  $\lambda 3.6$  with 100 m Effelsberg telescope (Krause 2009). The contours show the total intensities while the vectors the magnetic field orientations. The radio map is overlaid on an optical image from Canada-France-Hawaii Telescope/(c)1999 CFHT/Coelum. *Right panel:* Polarized intensity map at 4.86 GHz observed with VLA of NGC 5775 with vectors of magnetic field orientation (Soida et al. 2011) superimposed on an  $H\alpha$  image.

regular pattern is slightly shifted to the inner edges of the optical arms. Observations of NGC 6946 (Fig. 2.2, left panel) reveal two distinct magnetic spiral arms located in the interarm region, without any association with gas and stars. The magnetic arms are almost parallel to the adjacent optical arms, and are less than 1 kpc wide. Magnetic field seems to be almost perfectly aligned, because the degree of polarization is exceptionally high, around 50%.

In the case of barred galaxies the velocity pattern and the magnetic field structure

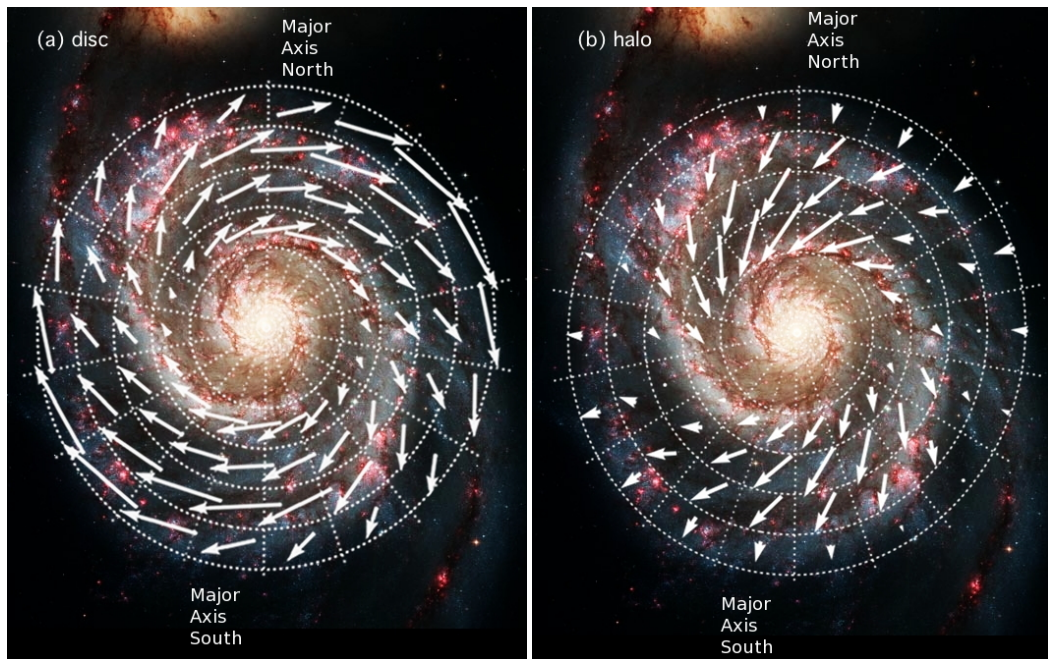


Figure 2.4: Regular magnetic field in M 51 derived by fitting a model to observed polarization angles at  $\lambda 3$ ,  $\lambda 6$ ,  $\lambda 18$ ,  $\lambda 20$  cm. *Left panel* shows the regular magnetic field in the disc and *right* in the halo. The length of the vectors is proportional to field strength and are overlaid on a Hubble Space Telescope optical image [image credit: NASA, ESA, S. Beckwith (STScI) and The Hubble Heritage Team (STScI/AURA)]. Figures from Fletcher et al. (2011).

is distorted by the gravitational potential of the bar. Observations of NGC 1097 and NGC 1365 (Beck et al. 2005) show that the polarized emission is the strongest in the galaxy centre, and the magnetic field is 20-30  $\mu\text{G}$  in the case of NGC 1365 and 60  $\mu\text{G}$  in NGC 1097. In the bar of NGC 1097 the magnetic field is aligned in the shearing flow causing a strong depolarization valleys, which are formed in front of the dust lanes (Fig. 2.1, right panel). In those regions the magnetic field vectors are rotated by almost  $90^\circ$  hence the polarized emission vanishes. In outer disk the magnetic fields forms a spiral structure along the optical arms also filling the interarm regions, with the maximum total magnetic field strength about 10  $\mu\text{G}$ .

Magnetic spiral structures can be also found in objects without prominent optical arms i.e. flocculent galaxies. In those objects the pattern of magnetic field is similar to that found in grand-designed galaxies (Knapik et al. 2000) suggesting that the dynamo works without assistance from density waves.

Another issue which is deeply studied is the vertical structure of the magnetic field in galaxies. Observations of several edge-on galaxies showed the magnetic field is mainly parallel to the disk along the mid plane of the disk. However away from the disk the magnetic field has vertical components increasing with the distance from the central re-

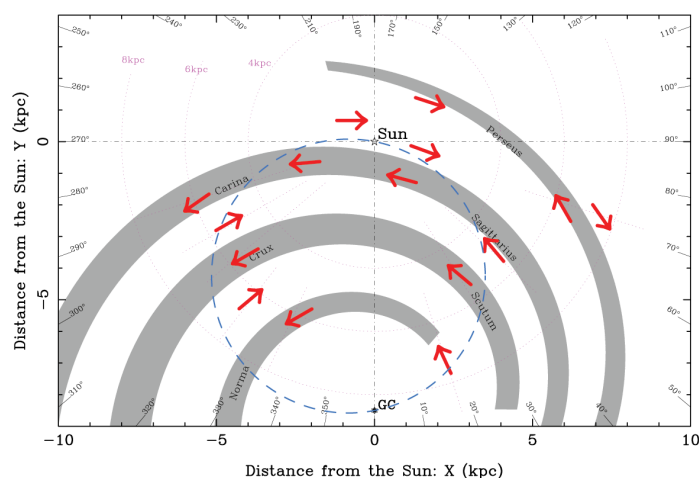


Figure 2.5: Magnetic field pattern (red arrows) in Milky Way inferred from observations of Faraday effect and dispersion measure of galactic pulsars. Spiral density waves are marked in grey. From Han et al. (2006).

gion. Such and X-shaped structure can be found in several galaxies, e.g. NGC 891 (Krause 2009) and NGC 5775 (Soida et al. 2011). Observations of these galaxies are shown in Fig. 2.3.

Recent observations and modelling of magnetic field structure in M 51 by Fletcher et al. (2011) reveals very intriguing results. The magnetic field in the disk plane seems to have a typical structure generated by the dynamo process and some slight deviations can be due to the interaction with neighbouring galaxy and prominent spiral arms. However the modelled field in the halo is surprising: it is directed inwards in the north, opposite to the direction of the disc field, and outwards in the south, same as the disc field, see Fig. 2.4. It is not clear what caused such structure in this galaxy. Fletcher et al. (2011) speculated that this can be related to: (i) two different dynamo regimes in disk and halo, (ii) a relic of magnetic field or (iii) advection of the disk field to the halo where the velocity field transforms it to the observed structure, this however needs further investigation.

### 2.1.2 Milky Way

The Milky Way is the "closest" galaxy to Earth, because we are part of this system and embedded in its environment. This makes it both easy and difficult to observe. It is easy because of the relatively short "distance", but because we are embedded in the system it is difficult to build whole picture of the large scale structure of the magnetic field and compare it with other galaxies. Mostly we built this picture by gathering many observations from different locations done with many techniques. One of them is to measure the Faraday effect of galactic and extragalactic objects. Such observations of 38 nearby galactic pulsars has shown the coherent component of the local magnetic field is primar-

ily toroidal with a strength  $B = 2.2 \pm 0.4 \mu\text{G}$  (Manchester 1974). The following years bring more such observations and multiply the sample by about 20. A new method to analyse such data was proposed by Frick et al. (2001). This method base on wavelet transformation and in their paper they conclude that the large scale structure of the Galactic magnetic field is quadrupolar. Wielebinski & Beck (2005) showed that the overall field structure follows the optical spiral arms which is distorted in some places close to star forming regions. They have found a large-scale field reversal of direction within the solar radius (Fig. 2.5). Sun et al. (2008) confirmed this result and showed that the field direction in the disk is the same as above and below the plane. According to radio synchrotron observations, optical polarizations and Zeeman splitting observations the mean value of magnetic field is  $6 \mu\text{G}$  near the Sun and increases to  $20\text{-}40 \mu\text{G}$  in the Galactic centre. In some structures, like radio filaments close to Galactic centre or massive star forming regions, strong deviations form the mean value of the magnetic field have been found, reaching even up to several mG strength (Heiles & Crutcher 2005).

### 2.1.3 Elliptical galaxies

There are strong indications that elliptical galaxies have  $\mu\text{G}$  magnetic fields, but with no positive detection of polarized synchrotron emission or any other manifestation of regular magnetic field (Moss & Shukurov 1996). Observations of these galaxies in radio is very difficult because of paucity of relativistic electrons, but still their presence is revealed using this technique and also by measuring the Faraday effect of background sources (Widrow 2002).

## 2.2 Dwarf galaxies

Dwarf galaxies are smaller, fainter and less massive than the spirals and ellipticals, but they are most numerous population in the Universe (Grebel 2001; Blanton et al. 2002). According to the hierarchical clustering scenario they were the primary building blocks of more massive objects. Via merging and mass accretion from the environment they form big spiral or barred galaxies and therefore dwarf galaxies are very important in the galaxies evolution. From the  $\Lambda\text{CDM}$  model of galaxy formation (Blumenthal et al. 1984) we know the predicted number of dwarfs around more massive objects, like e.g. our Galaxy. However the observations did not agree with this prediction because the number of observed dwarfs around Milky Way is less than expected. The "missing satellites problem" (e.g. Kravtsov 2010) seems to be resolved recently by finding ultra faint dwarfs in the Sload Digital Sky Survey data (Belokurov et al. 2007). The question of formation of this objects has been studied by e.g. Governato et al. (2010) and Łokas et al. (2012).

The magnetic fields in dwarf galaxies can play very important role. First, the observations show that the magnetic field is and important source of pressure for the ISM

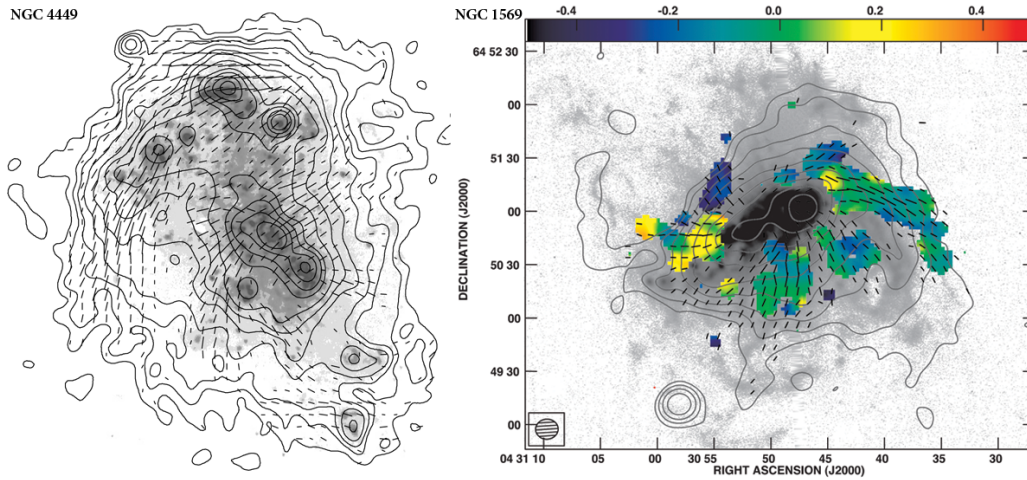


Figure 2.6: *Left panel:* radio observations of NGC 4449 by Chyży et al. (2000) with VLA. Total power contour map at 8.46 GHz with B-vectors of polarized intensity is superimposed on  $H\alpha$  image. *Right panel:* Radio observations of NGC 1569 done by Kepley et al. (2010) with VLA and WSRT. Rotation measure is marked in colour and it is given in units  $10^3 \text{ rad m}^{-2}$ . Total power contours and B-vectors are derived from  $\lambda 3 \text{ cm}$  data and are overlaid on an  $H\alpha$  image.

(Boulares & Cox 1990). It is often assumed that the ISM in galaxies is in equipartition with almost equally distributed energy into magnetic fields, cosmic rays and turbulence (Ferrière 2001). Second, these objects are less massive hence the gravitational potential well is shallower and this facilitate the gas to escape the galaxy in form of galactic winds (e.g. Mac Low & Ferrara 1999; Scannapieco & Brügggen 2010). This wind can also drag the magnetic field out of the disk to the intergalactic medium (IGM) since the magnetic field is frozen into the outflowing plasma. Possible magnetization of the IGM via the magnetized wind has been studied by Bertone et al. (2006) and in the case of dwarf galaxies by Kronberg et al. (1999). Simulations of cosmic ray dynamo process in dwarf galaxies (Siejkowski et al. 2010) show significant loss of the magnetic field from the domain and the outflow depends on the star formation rate. Studies of dwarf galaxy formation by Dubois & Teyssier (2010) also implies the IGM seeding via the galactic winds.

Strong magnetic fields were discovered in bright NGC 4449 with the total field strength of about  $12 \mu\text{G}$  and regular component of up to  $8 \mu\text{G}$  (Klein et al. 1996; Chyży et al. 2000). Kepley et al. (2010) reported about similar magnetic fields in NGC 1569. In other objects like NGC 6822, IC 10 (Chyży et al. 2003) and LMC (Klein et al. 1993; Gaensler et al. 2005) the observed magnetic fields are weaker, reaching a value about  $5\text{-}7 \mu\text{G}$ . The observed structure of the magnetic fields in dwarf galaxies is similar to this found in flocculent galaxies. In Fig. 2.6 I present the polarization maps of NGC 4449 (left panel) and NGC 1569 (right panel). They have large scale magnetic fields with a signs of spiral pattern, but no optical counterparts are present. It is worth noticed that these galaxies,

CHARACTERISTICS OF OBSERVED DWARF GALAXIES					
Galaxy name	$B_{\text{tot}}$ $\mu\text{G}$	SFR $10^{-3} \text{ M}_{\odot} \text{ yr}^{-1}$	Total mass $10^6 \text{ M}_{\odot}$	$v_{\text{rot}}$ $\text{km s}^{-1}$	Linear size kpc
Aquarius*	$<4.5 \pm 1.2$	0.046	5.4	13	$0.61 \times 0.30$
SagDIG*	$<4.1 \pm 1.1$	0.067	9.6	14	$0.88 \times 0.64$
Pegasus*	$<3.7 \pm 0.9$	0.300	58	17	$1.11 \times 0.60$
Leo A*	$<4.4 \pm 1.2$	0.032	11	18	$1.03 \times 0.62$
LGS 3*	$<4.0 \pm 1.0$	0.003	13	18	$0.36 \times 0.36$
GR 8*	$<3.6 \pm 0.9$	0.700	7.6	21	$0.70 \times 0.64$
WLM*	$<3.9 \pm 0.9$	1.000	150	23	$3.08 \times 1.07$
Sextans A*	$<3.1 \pm 0.8$	2.000	395	33	$2.26 \times 1.88$
Sextans B*	$<2.8 \pm 0.6$	2.000	885	38	$2.02 \times 1.39$
IC 1613*	$2.8 \pm 0.7$	3.000	795	37	$3.44 \times 3.08$
NGC 4449	$9.3 \pm 2.0$	470.000	70000	40	$6.66 \times 4.73^{\dagger}$
NGC 1569	$14.0 \pm 3.0$	320.000	297	42	$3.03 \times 1.52^{\dagger}$
IC 10*	$9.7 \pm 2.0$	60.000	1580	47	$1.31 \times 1.13$
NGC 6822*	$4.0 \pm 1.0$	21.000	1640	58	$2.25 \times 1.96$
SMC*	$3.2 \pm 1.0$	46.000	2400	60	$5.85 \times 3.22^{\dagger}$
LMC*	$4.3 \pm 1.0$	260.000	20000	72	$9.38 \times 8.00^{\dagger}$

Table 2.1: Magnetic fields estimation and physical parameters for sample of Local Group dwarfs and comparison objects. Subsequent columns show: the galaxy name the total magnetic field, the star formation rate, the total mass and the linear size. Members of the Local Group are marked with \*. Most of the data come from Chyży et al. (2011) except those marked with  $\dagger$  which are taken from NED database. The horizontal line separates the object list for galaxies with only upper limits on magnetic field (upper part) and with positive detection (lower part). Within each part objects are sorted ascending with respect to the rotational velocity.

especially NGC 1569, are under strong influence of infalling gas from the surrounding, which have a significant impact on the magnetic field structure.

Observations of these objects brought some insight about the dynamo process in dwarf galaxies, but all of these objects are optically bright and showed disturbed kinematics. Therefore the sample could be influenced by a strong selection effects. Chyży et al. (2011) completed a sample of dwarf and small irregular galaxies from the Local Group. In their paper they searched for different relations between the magnetic fields and other properties like star formation rate (SFR), velocity rotation, etc. This sample was intended to be a representative group of objects to investigate the typical conditions for dynamo process to occur. A list of objects from the sample is showed in Tab. 2.1.

Chyży et al. (2011) found that SFR regulates the strength of magnetic fields (see Fig. 2.7, left panel). This seems to be consistent with the predictions of the dynamo theory, where the generated magnetic field depends on the energy input (see Sec. 2.3.1). SFR determines the number of supernova explosions which contributes significantly to the turbulent energy. These results are very similar to the conclusions of the previous theo-

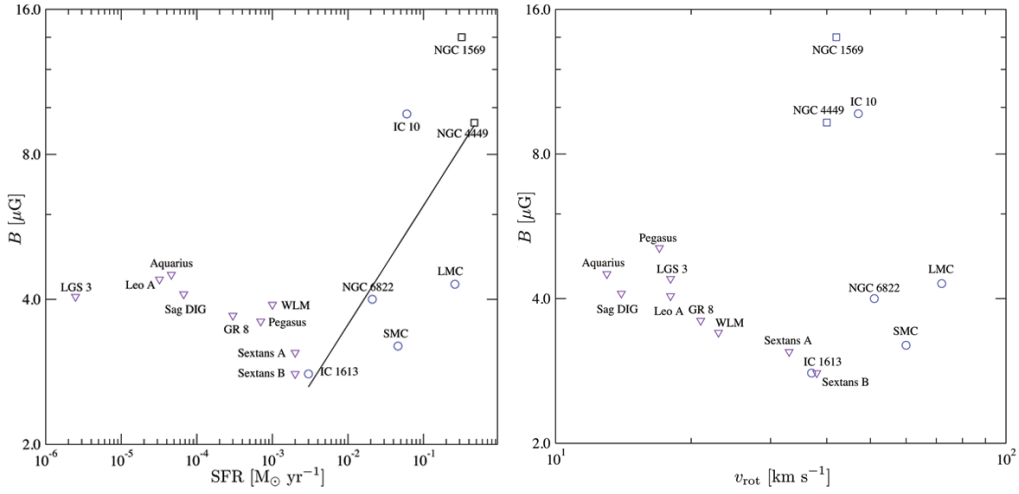


Figure 2.7: Magnetic fields dependence on star formation rate (*left panel*) and rotation velocity (*right panel*) deduced from observations by Chyży et al. (2011). The objects marked with triangles show only upper limits of the magnetic field strength.

retical study by Siejkowski et al. (2010).

Another key parameter of the dynamo process is the velocity of the rotation (see Sec. 2.3.1). Chyży et al. (2011) have investigated a possible relation between the maximum  $v_{\text{rot}}$  and magnetic field strength (see 2.7, right panel). For slow rotation ( $< 40$  km/s) all galaxies have weak fields, below  $4 \mu\text{G}$ . However faster rotating objects can have stronger or weaker fields, but this relation is probably distorted by the fact that objects with strong magnetic fields are undergoing a heavy star formation. The contribution to the turbulent energy by supernova explosions can cause a strong disturbances in the velocity pattern, therefore the estimation of the maximum rotation speed is difficult. For the comparison of the rotation curves for NGC 4449 (high SFR) and NGC 6822 (low SFR) see Fig. 2.8.

### 2.3 Magnetic dynamo

Magnetic dynamo is a process, which converts a kinetic energy of electrically conducting matter into magnetic field. For the first time in astrophysical context this process was applied by Larmor (1919) to explain magnetic fields in the Sun and Earth. The dynamo theory started to develop. Finally Parker (1971) propose that this process can also operate in galaxies. In literature the dynamos often are divided into small scale and large scale dynamos (Brandenburg & Subramanian 2005). Large scale dynamos generate magnetic fields with spatial coherence and also long-term temporal order e.g. the 11 year solar cycle. Otherwise the small scale dynamo, often called fluctuation dynamo, produce magnetic fields that are correlated on scales of the order of the energy carrying scale of the turbulence or smaller. The small scale dynamo is very important because it can grow the

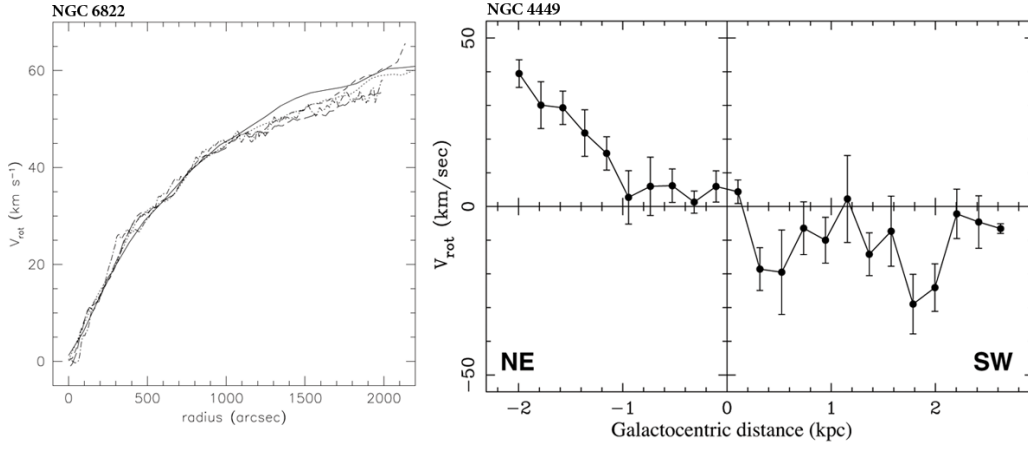


Figure 2.8: *Left panel:* Rotation curve of NGC 6822 derived from H<sub>I</sub> observations by Weldrake et al. (2003). *Right panel:* Rotation curve of NGC 4449 derive from H $\alpha$  data by Valdez-Gutiérrez et al. (2002).

magnetic fields in physical settings where the large scale dynamo do not operate. This can be related to objects with low rotation like e.g. galaxy clusters. This type of dynamo has larger growth rates than the large scale and therefore it can play a role in the Early Universe, where very weak primordial magnetic fields were generated. The observations described in Sec. 2.1.1 and 2.2 show that galaxies have a large scale magnetic fields, so the process which is responsible for producing and maintaining such fields is the large scale dynamo.

Galaxies create a perfect place to host a dynamo process. They have lots of kinetic energy stored in **(a)** a large scale differential rotation, **(b)** small scale turbulence induced by supernova explosions and **(c)** the ISM is ionized. According to Ferrière (2001) the ISM is a multi phase medium and its biggest volume fraction is filled with an ionized gas of temperature 6000 K and above. The **(a)**, **(b)** and **(c)** components make possible to initiate and maintain the large scale dynamo action in galaxies.

The dynamo theory is based on the induction equation (e.g. Jackson 1975):

$$\frac{\partial \mathbf{B}}{\partial t} = \nabla \times (\mathbf{v} \times \mathbf{B}) - \nabla \times (\eta \nabla \times \mathbf{B}), \quad (2.1)$$

where  $\eta = 1/\sigma\mu$  is the magnetic diffusivity with  $\sigma$  electrical conductivity and  $\mu$  permeability. If the  $\eta$  is constant the above equation simplifies to:

$$\frac{\partial \mathbf{B}}{\partial t} = \nabla \times (\mathbf{v} \times \mathbf{B}) + \eta \nabla^2 \mathbf{B}. \quad (2.2)$$

To get a dynamo solution one can use the mean field approximation (Moffatt 1978) or using the perturbation theory (Shukurov & Sokoloff 2008). However each of the model need initially non-zero magnetic field i.e.  $\mathbf{B}(t = 0) \neq 0$ . This not only an issue of initial conditions for equation solution but it is a big and still open question of the origin of

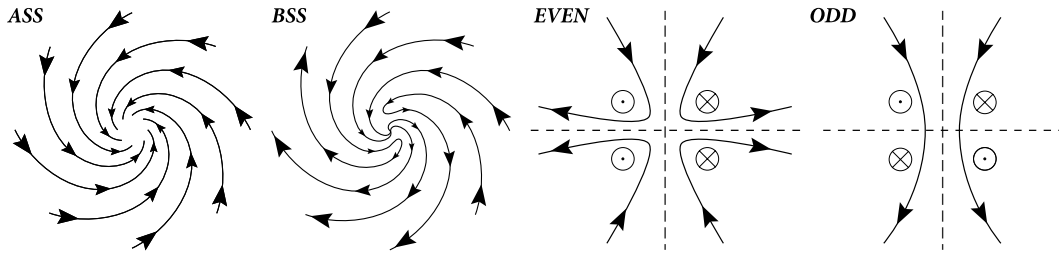


Figure 2.9: From left: axisymmetric (ASS) and bisymmetric (BSS) field configurations for disk systems; quadrupolar (even symmetry) and dipolar (odd symmetry) vertical field configurations. The toroidal field is indicated by  $\otimes$  (field out of the page) and  $\odot$  (field into the page). The horizontal and vertical dashed lines show disk midplane and rotation axis, respectively.

magnetic fields in the Early Universe. Widrow (2002) in his review introduced a current knowledge and possible explanation of the primordial magnetic fields.

The large scale dynamo is responsible for the shape of magnetic fields global structure. In the galaxy plane the azimuthal structure can be axisymmetric (ASS) or bisymmetric spiral (BSS), see Fig. 2.9 for details. Most of the galaxies have the ASS mode or the mixture of the ASS and the BSS. So far only in one galaxy the BSS structure has been found, namely in M 81 (Sokoloff et al. 1992). In the case of the vertical structure it can be dipolar (odd symmetry) or quadrupolar (even symmetry), see Fig. 2.9 for details. The vertical field with an odd symmetry is excited by dynamo in spherical objects like stars or planets. On the other side galaxies, i.e. very flat objects, the vertical field have the even symmetry.

### 2.3.1 Cosmic ray driven dynamo

The dynamo efficiency is characterized by the growth rate of the magnetic fields. This is especially important in the case of galactic dynamo, because the extremely weak primordial magnetic fields should be amplified within a galaxy lifetime. Observations shows that galaxies of redshift  $z = 1$  already have strong magnetic fields (Bernet et al. 2008). The solution of the mean field dynamo results however in small amplification time scales and additionally it does not assume any feedback of the magnetic fields on the medium (Widrow 2002), therefore alternatives scenarios has been developed. One of them is a process proposed by Gressel et al. (2008) where the dynamo is driven by the thermal instabilities cause by explosions of supernovae. They found that the  $e$ -folding time of the amplification mechanism is about  $\tau_e = 250$  Myr and is dependent on the rotation speed. A second approach suggested by Parker (1992) relies on the fact that the gaseous disc of a galaxy is unstable to perturbations of the magnetic field lines which lie parallel to the plane (Parker 1965). The unperturbed state consists of magnetic field embedded in the stratified and partially ionised medium (i.e. ISM), and the cosmic rays. If there is a kink

in the magnetic field lines which causes them to bulge out of the plane. The cosmic rays 'inflates' the kink, but the cold matter falls down to the galactic plane. The kink starts to be buoyant and grows creating a so called Parker loop. This mechanism can occur when the cosmic ray pressure is greater than the magnetic field pressure. The cosmic rays are efficiently produced in the supernova explosions so they can be responsible for creating such kink. If the 'inflated' Parker loop is growing in a rotating system the Coriolis force acts on it and cause a twist. The lines close to galactic plane starts to be oppositely directed and a reconnection event can occur creating a closed loop. If this process repeats many times it can lead to a significant increase of the total magnetic flux.

The cosmic ray driven dynamo has been numerically tested in the case of local shearing box approximation of a spiral galaxy (Hanasz et al. 2006). The  $e$ -folding time scale of the magnetic field amplification can be as fast as 140 Myr. An extensively parameter study of this local model is presented in Hanasz et al. (2009a). Hanasz et al. (2009b) and Kulpa-Dybeł et al. (2011) reported about cosmic ray driven dynamo in global simulations of spiral and barred galaxy, respectively. They found that the dynamo  $e$ -folding time in both cases is around 300 Myr. Siejkowski et al. (2010) apply this dynamo model to the low mass objects, like dwarfs and small irregular galaxies. The growth rate of the magnetic field is strongly dependent on the rotation speed, but for objects with  $v_{\text{rot}} > 40 \text{ km s}^{-1}$  the saturation of the dynamo is reached after 1,5-2 Gyr. The saturation occurs because the magnetic field pressure is comparable to the cosmic-ray pressure, and the Parker loops can not be so easily created. The  $e$ -folding time is also dependent on the supernova rate (SNR) and the time of quiescent state (no supernova activity). The bigger the SNR the faster the growth rate, but too much of the explosions can suppress the dynamo action, especially the creation of the regular component of the magnetic field.

The local simulations however give no hint about the large scale azimuthal and vertical structure of the magnetic fields. There have been attempts to determine such structure by joining few simulation boxes located at different radius Otmianowska-Mazur et al. (2009) but this method is not applicable to the small objects. Dwarf galaxies are very small (few kpc in diameter) and the rotation curve changes rapidly with radius, so to derive the global structure one should simulate a whole galaxy within a domain. The aim of this work is building a consistent with observations global model of a dwarf galaxy and simulate the cosmic-ray driven dynamo. In the next chapter I show a detailed description of the dwarf galaxy model.

## Numerical model

### 3.1 MHD equations

To simulate the dwarf galaxy model a numerical code called GODUNOV-MHD was employed. It solves a system of 3D magnetohydrodynamics equations in a conservative form (eg. Goedbloed & Poedts 2004):

$$\frac{\partial \rho}{\partial t} + \nabla \cdot (\rho \mathbf{v}) = 0 \quad (3.1)$$

$$\frac{\partial \rho \mathbf{v}}{\partial t} + \nabla \cdot \left[ \rho \mathbf{v} \mathbf{v} + \left( p + p_{\text{cr}} + \frac{B^2}{8\pi} \right) \mathbf{I} - \frac{\mathbf{B} \mathbf{B}}{4\pi} \right] = -\rho \nabla \phi \quad (3.2)$$

$$\frac{\partial \mathbf{A}}{\partial t} - \mathbf{v} \times (\nabla \times \mathbf{A}) - \eta \nabla \times (\nabla \times \mathbf{A}) = 0, \quad (3.3)$$

where:  $\rho$ ,  $p$  and  $\mathbf{v}$  are the gas density, pressure and velocity, respectively,  $p_{\text{cr}}$  is the cosmic-ray pressure (for details see Sec. 3.2),  $\mathbf{A}$  is the vector potential,  $\mathbf{B} \equiv \nabla \times \mathbf{A}$  is the magnetic field,  $\phi$  is the gravitational potential,  $\eta$  is the magnetic turbulent diffusivity and  $\mathbf{I}$  is the identity matrix. To close the system an isothermal equation of state is assumed:

$$p \equiv \frac{c_s^2}{\gamma} \rho \quad (3.4)$$

where  $c_s$  is the isothermal speed of sound and  $\gamma$  is the adiabatic index of the gas.

### 3.2 Cosmic ray component

The MHD equations describes the evolution of the plasma and magnetic field, but as mentioned in the Sec. 2.3.1 the cosmic-ray driven dynamo needs an additional component, namely the cosmic rays (CRs). If we assume that, as a result of scattering off magnetic field inhomogeneities, the CR particles participates completely in the motion

of the thermal gas then we can approximate this component as a fluid which evolution is described by the diffusion-advection transport equation (Schlickeiser & Lerche 1985):

$$\frac{\partial e_{\text{cr}}}{\partial t} + \nabla(e_{\text{cr}}\mathbf{v}) = \nabla(\hat{K}\nabla e_{\text{cr}}) - p_{\text{cr}}(\nabla \cdot \mathbf{v}) + Q, \quad (3.5)$$

where  $e_{\text{cr}}$  is the CR energy density,  $\hat{K}$  is the diffusion tensor,  $\mathbf{v}$  is the plasma velocity,  $p_{\text{cr}}$  is the CR pressure and  $Q$  is the source term of  $e_{\text{cr}}$ . CR pressure is related to the  $e_{\text{cr}}$  via the adiabatic CR index:

$$p_{\text{cr}} \equiv (\gamma_{\text{cr}} - 1)e_{\text{cr}}. \quad (3.6)$$

The diffusion of CRs is anisotropic (Giacalone & Jokipii 1999) with respect to the magnetic field, hence the diffusion tensor  $\hat{K}$  from Eq. 3.5 is defined as follows (Ryu et al. 2003):

$$K_{ij} = K_{\perp}\delta_{ij} + (K_{\parallel} - K_{\perp})n_i n_j, \quad (3.7)$$

where  $K_{\perp}$  and  $K_{\parallel}$  are the diffusion coefficients perpendicular and parallel to the local magnetic field, respectively, and  $n_i \equiv B_i/B$  is the  $i$ -th component of the vector tangent to the local magnetic field.

### 3.3 Gravitational potential

The dwarf galaxy potential well is given by two components dark matter (DM) halo and thin stellar disc. This type of galaxies do not have bulge (Governato et al. 2010) which is usually present in bigger objects, like grand designed spirals. The stars are distributed in infinitesimally thin Kuzmin's disk with surface density (eg. Binney & Tremaine 2008):

$$\Sigma_{*}(R) = \frac{aM_{*}}{2\pi(R^2 + a^2)^{3/2}} \quad (3.8)$$

where  $M_{*}$  is the total mass of stars,  $a$  is the radial scalelength and  $R$  is the radius in equatorial plane ( $z = 0$ ), i.e.  $R \equiv \sqrt{x^2 + y^2}$ . The potential well generated by this mass distribution is (Fig. 3.1):

$$\phi_{*}(R, z) = -\frac{GM_{*}}{\sqrt{R^2 + (a + |z|)^2}}. \quad (3.9)$$

In order to generate a flat rotation curve in outer regions of galaxy one needs to add a DM halo to the gravitationally potential. Often the DM halo in galaxies is approximated by a “modified isothermal sphere” (MIS) which belongs to a class of double (broken) power-low density distributions (see Mo et al. 2010). The density profile for this particular case is:

$$\rho_h^{\text{iso}}(r) = \frac{\rho_0}{1 + (r/r_0)^2}, \quad (3.10)$$

where  $\rho_0$  is the central density,  $r_0$  is the core radius and  $r$  is the distance to the centre  $r \equiv \sqrt{R^2 + z^2}$ . The halo mass as a function of radius is then:

$$M_h^{\text{iso}}(r) = \int_0^r dr' 4\pi r'^2 \rho_{DM}^{\text{iso}}(r') = 4\pi\rho_0 r_0^3 (x - \arctan x), \quad (3.11)$$

where  $x \equiv r/r_0$ . Using the Poisson's equation we can find the DM potential for the isothermal case:

$$\phi_h^{\text{iso}}(r) = 4\pi G \rho_0 r_0^2 \left[ \frac{1}{2} \ln(1 + x^2) + \frac{\arctan x}{x} \right], \quad (3.12)$$

where  $G$  is the gravitational constant.

Burkert (1995) showed that Eq. 3.11 do not agree with the DM mass distribution derived from the observations of neutral hydrogen rotation curves in four well studied dwarf galaxies. In his paper he propose a purely phenomenological DM density profile for dwarfs:

$$\rho_h^{\text{B}}(r) = \frac{\rho_0 r_0}{(r + r_0)(r^2 + r_0^2)} \quad (3.13)$$

where  $r_0$ ,  $\rho_0$  and  $x$  have the same meaning as in the isothermal sphere case. The mass distribution is then:

$$M_h^{\text{B}}(r) = \pi\rho_0 r_0^3 \left\{ -2\arctan x + 2\ln(1 + x) + \ln(1 + x^2) \right\}, \quad (3.14)$$

and the gravitational potential is:

$$\phi_h^{\text{B}}(r) = -\pi G \rho_0 r_0^2 \left\{ \pi - 2(1 + x^{-1})\arctan x + 2(1 + x^{-1})\ln(1 + x) - (1 - x^{-1})\ln(1 + x^2) \right\}. \quad (3.15)$$

The ‘‘modified isothermal sphere’’ and Burkert gravitational potentials are compared in Fig. 3.1.

### 3.4 Supernovae

In the cosmic-ray driven dynamo model the source term  $Q$  in Eq. 3.5 is attributed to the supernovae remnants (Hanasz et al. 2004) where the CR particles are accelerated. A fraction of the kinetic energy output of the SN explosion is converted into the acceleration of the cosmic rays in the shock front. The conversion rate is 10-30% (Dorfi 2000) of

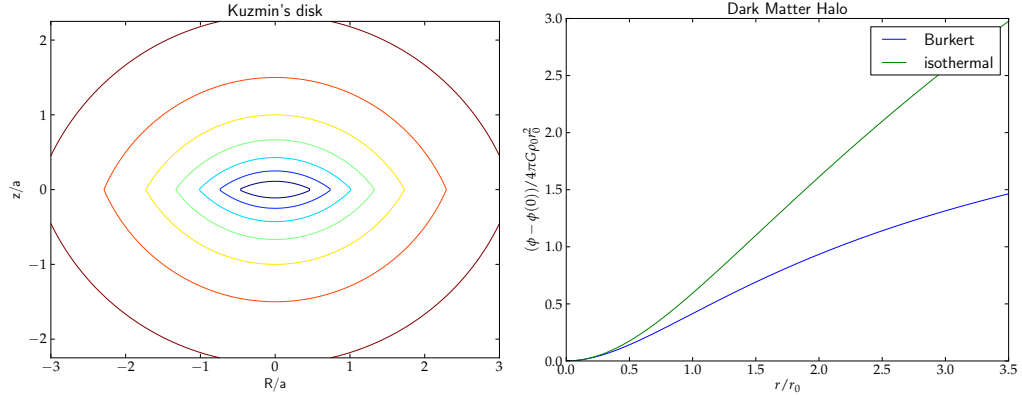


Figure 3.1: *Left panel:* contours of potential for a stellar component modelled by Kuzmin's disk profile (Eq. 3.9). *Right panel:* comparison of dark matter halo potential models of Burkert (blue line, Eq. 3.15) and modified isothermal sphere (green line, Eq. 3.12).

the kinetic energy. In this project it is assumed that the kinetic energy output of the SN explosion is  $10^{51}$  erg and the conversion rate is 10%.

In the model each SN explosion is modelled by a 3D Gaussian distribution of cosmic ray energy input and it is added to the source term  $Q$  in Eq. 3.5. Some of the explosions are magnetized and besides the input of CR energy, it injects a randomly oriented dipole magnetic field to the ISM. The shape of vector potential is then (eg. Griffiths 1999):

$$\mathbf{A}_{\text{dip}}(\mathbf{r}) = A_0 \frac{\hat{\mathbf{m}} \times \mathbf{r}}{r^3} \quad (3.16)$$

where  $A_0$  is the amplitude and  $\hat{\mathbf{m}}$  is the randomly oriented unit vector of the magnetic dipole moment. The magnetized SN explosions occurs only for the first  $t_{\text{mag}}$  time and only 10% of all explosions in that time are magnetized.

The position of SNe explosion is chosen randomly according to the local gas density. Schmidt (1959) and Kennicutt (1989) showed that in a simple self-gravitational picture the large-scale star formation rate volume density  $\rho_{\text{SFR}}$  scales with gas density as follows:

$$\rho_{\text{SFR}} \propto \rho^{3/2}. \quad (3.17)$$

Using this relation we can build a cumulative distribution function (CDF) of SN explosions in a galactic disk. Assuming a temporally constant SNe explosions frequency  $f_{\text{SN}}$  we can calculate a number of exploding stars and find their positions according to CDF in each time step. The  $f_{\text{SN}}$  is modulated in time and a schematic view of the SNe activity history is shown in Figure 3.2.

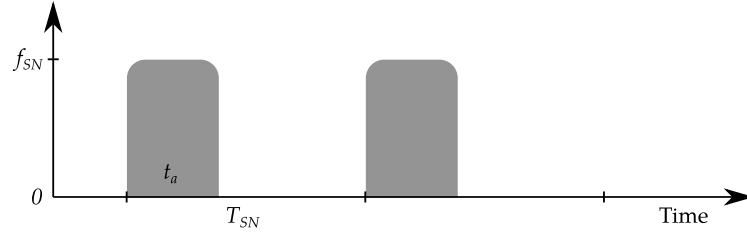


Figure 3.2: A scheme of supernovae activity modulation. In the each  $T_{SN}$  period only for time  $t_a$  the supernovae are active. This on-off modulation repeats in whole simulation.

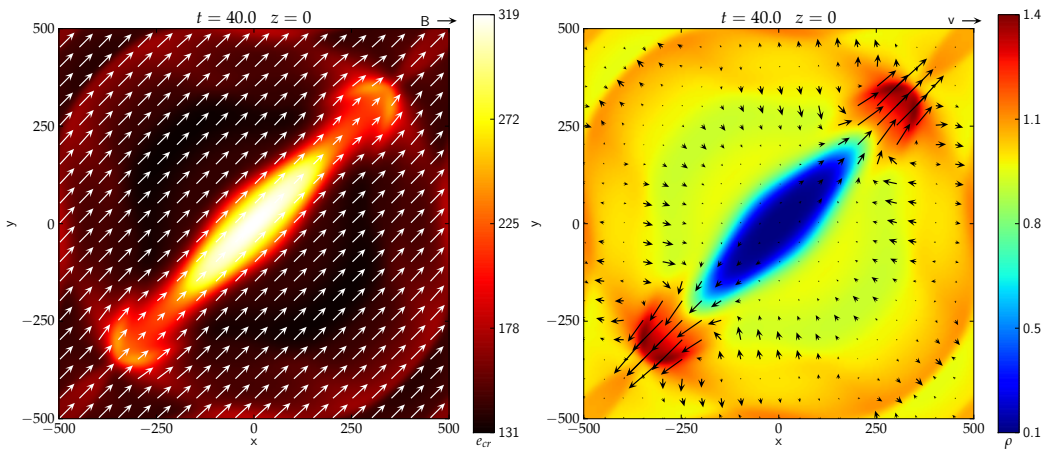


Figure 3.3: Test of CR diffusion along inclined magnetic field in an uniform medium (Hanasz & Lesch 2003, Sec. 4.3). *Left panel* shows the CR energy density with over plotted magnetic field. *Right panel* shows gas density and velocity field. Parameters and initial conditions of the simulation are taken from the original paper.

### 3.5 Numerical code

Simulations of the dwarf galaxy model is done in framework of the numerical code GODUNOV-MHD written by Grzegorz Kowal (Kowal et al. 2009). The code solves set of MHD equations in a 3D Cartesian domain. It is written in Fortran 90/95 and the parallelisation bases on MPI-2 interface (e.g. Gabriel et al. 2004) or OpenMP directives (e.g. Chapman et al. 2007).

The code solves system of MHD equations (Sec. 3.1) using the Godunov scheme (Godunov 1959) and approximated Riemann solvers: HLL (Harten et al. 1983) or HLLD (Mignone 2007). The spatial reconstruction of states is second order accurate (see e.g. LeVeque 2002) and the integration in time is calculated according to the Runge-Kutta method (see e.g. Del Zanna et al. 2003). The induction equation (Eq. 3.3) is integrated with the field-interpolated constrained transport (CT) scheme based on a staggered mesh (see Londrillo & Del Zanna 2000) to maintain the  $\nabla \cdot \mathbf{B} = 0$  numerically constrained. The GODUNOV-MHD code is extensively used in different astrophysical research fields simu-

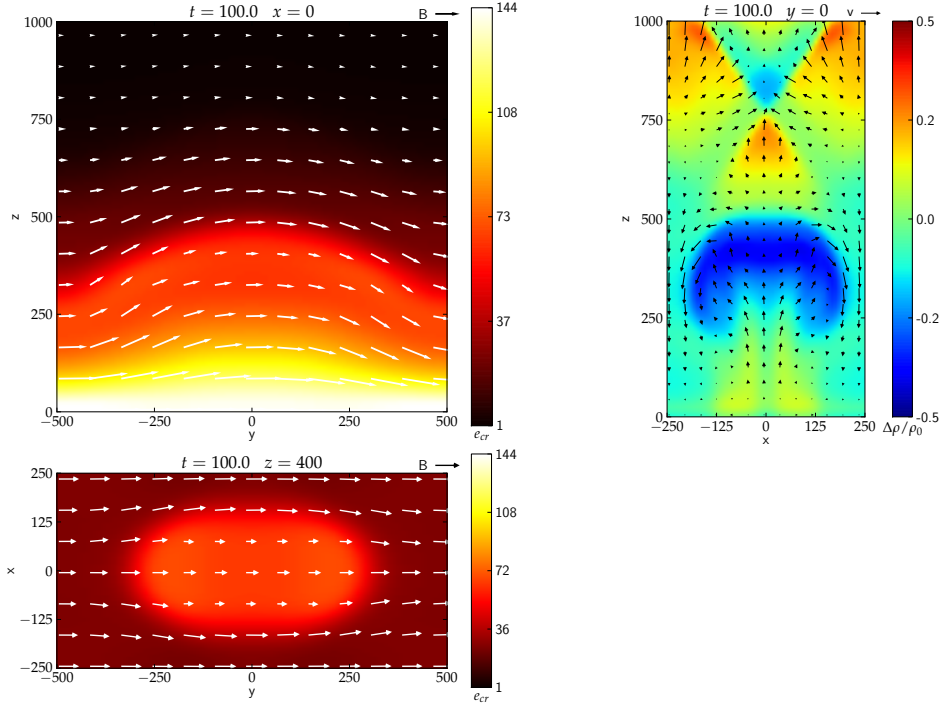


Figure 3.4: Test of CR diffusion in a stratified medium (Hanasz & Lesch 2003, Sec. 5). *Left panels* show CR energy density with over plotted magnetic field. *Right panel* show a density perturbation  $\Delta\rho/\rho_0$  in  $t = 100$  with over plotted velocity field, where  $\rho_0 = \rho(t = 0)$ . Parameters and initial conditions of the simulation are taken from the original paper.

lating the small scale phenomena of turbulent reconnection (Kowal et al. 2009), the large scale evolution of magnetic field in galaxies (e.g. Kulpa-Dybeł et al. 2011; Otmianowska-Mazur et al. 2011) and collisionless plasma in intra cluster medium (Kowal et al. 2011).

The cosmic-ray transport equation (Eq. 3.5) is incorporated to the code following the Hanasz & Lesch (2003) description. The scheme has been tested using the tests from the paper. The results of the active CR transport in uniform and stratified media are presented in Fig. 3.3 and 3.4, respectively.

### 3.6 Initial conditions

The dwarf galaxy is set to be in hydrostatic equilibrium in its initial state. First the gas density distribution in equatorial plane is assumed in a following form:

$$\rho(R, z = 0) = \frac{\rho_0}{\left[1 + \left(\frac{R}{R_c}\right)^2\right]^2}, \quad (3.18)$$

where  $\rho_0$  and  $R_c$  are the central gas density and core radius, respectively. Then to find the global gas distribution I use the "potential method" following Wang et al. (2010). The

gravitational potential is the sum of dark matter halo and stellar components,  $\phi = \phi_{\text{DM}} + \phi_*$ . The azimuthal rotation velocity in a galaxy is found by solving the equation:

$$v_{\text{rot}}^2 = R \left. \frac{\partial \phi}{\partial R} \right|_{z=0} + c_s^2 (1 + \alpha + \beta) \left. \frac{\ln \rho}{\ln R} \right|_{z=0}. \quad (3.19)$$

From the gas distribution the CR component distribution is found assuming they are in pressure equilibrium, namely  $\beta \equiv p_{\text{CR}}/p_{\text{gas}} = 1$ . The magnetic field in  $t = 0$  is set to be zero ( $\alpha \equiv p_{\text{mag}}/p_{\text{gas}} = 0$ ). To seed the dynamo action 10% of the SNe explosions are magnetized (Sec. 3.4). The magnetized explosions occurs only for the first time  $t_{\text{mag}}$ , and then they are stopped. For the cases where the dynamo process operate the contribution to the magnetic field from the magnetized explosions is negligible.

### 3.7 Model parameters and setups

The dwarf galaxy model described in details in latter sections is controlled by a number of parameters. All these parameters and their units are summarised in Tables 3.1 and 3.2. The three cardinal units i.e. time, length and mass are set to Gyr, kpc and  $10^6 M_{\odot}$ , respectively. The parameters showed in Table 3.1 are constant for all models presented in this work.

#### 3.7.1 Reference models

The basic distinction for the models is done according to the initial rotational velocity (see Table 3.3), which spans from 20 up to 70  $\text{km s}^{-1}$ . The different  $v_{\text{rot}}$  are achieved only by increasing the stellar mass and DM core density. To create more realistic models the object size, which is related to the  $R_C$  parameter, is also bigger for faster rotating objects. The rotation curves for those models are presented in Figure 3.5. The model name consists of letter ‘v’ which stands for the velocity and a number which is a value of the initial  $v_{\text{rot}}$ . The models with the letter ‘b’ use the purely phenomenological DM profile proposed by Burkert (Eq. 3.15).

In this reference models the assumed isothermal speed of sound is  $\hat{c}_s = 7 \text{ km s}^{-1}$  and corresponds to the temperature of a gas about 6000 K. The SN frequency is set to  $f_{\text{SN}} = 3000 \text{ kpc}^{-2} \text{ Gyr}^{-1}$  and is approximately equivalent to star formation surface density  $\Sigma_{\text{SFR}} = 4.7 \times 10^{-4} M_{\odot} \text{ yr}^{-1} \text{ kpc}^{-2}$  (see Appendix A). This number is representative for the dwarf galaxies sample from Chyży et al. (2011). The  $f_{\text{SN}}$  is modulated with a period  $T_{\text{SN}} = 0.2 \text{ Gyr}$ , and the SNe are active only for the beginning  $t_a = 0.04 \text{ Gyr}$  of each period (see Sec. 3.4).

THE SUMMARY OF CONSTANT PARAMETERS OF THE DWARF GALAXY MODEL			
Symbol	Description	Value	Unit
$K_{\parallel}$	parallel diffusion coefficient of the CR gas	10.0 $3 \times 10^{23}$	$\text{kpc}^2 \text{Gyr}^{-1}$ $\text{m}^2 \text{s}^{-1}$
$K_{\perp}$	perpendicular diffusion coefficient of the CR gas	1.0 $3 \times 10^{22}$	$\text{kpc}^2 \text{Gyr}^{-1}$ $\text{m}^2 \text{s}^{-1}$
$\eta$	magnetic diffusivity	0.1 $3 \times 10^{21}$	$\text{kpc}^2 \text{Gyr}^{-1}$ $\text{m}^2 \text{s}^{-1}$
$\rho_g$	central gas density	29.5 $2 \times 10^{21}$	$10^6 M_{\odot} \text{kpc}^{-3}$ $\text{kg m}^{-3}$
$\gamma$	gas adiabatic index	5/3	
$\gamma_{\text{cr}}$	CR gas adiabatic index	14/9	
$\alpha$	ratio of magnetic to gas pressure ( $p_{\text{mag}}/p_{\text{gas}}$ )	0	
$\beta$	ratio of CR to gas pressure ( $p_{\text{cr}}/p_{\text{gas}}$ )	1	
$t_{\text{mag}}$	period of time for magnetized SNe activity	0.6	Gyr
Numerics			
$N_x$	number of points in the domain in $x$ direction	256	
$N_y$	number of points in the domain in $y$ direction	256	
$N_z$	number of points in the domain in $z$ direction	128	
$C_{\text{max}}$	Courant-Friedrichs-Lewy condition (Courant et al. 1967)	0.6	

Table 3.1: The subsequent columns show: the symbol of the parameter, a brief description, the assumed value and its unit. For reader convenience some parameters are given also in the SI units.

THE SUMMARY OF DWARF GALAXY MODEL PARAMETERS		
Symbol	Description	Unit
$\hat{c}_s$	isothermal speed of sound, $\hat{c}_s \equiv c_s/\gamma$	$\text{kpc Gyr}^{-1}$
$M_*$	total mass of stars	$10^6 M_{\odot}$
$a$	radial scalelength of the stellar gravitational potential	kpc
$\rho_0$	central density of the DM gravitational potential	$10^6 M_{\odot} \text{kpc}^{-3}$
$r_0$	core radius of the DM gravitational potential	kpc
$R_C$	core radius of the gas density distribution	kpc
$f_{\text{SN}}$	SNe explosions frequency	$\text{kpc}^{-2} \text{Gyr}^{-1}$
$T_{\text{SN}}$	period of the SNe modulation	Gyr
$t_a$	duration of the SNe activity within one $T_{\text{SN}}$	Gyr

Table 3.2: The subsequent columns show: the symbol of the parameter, a brief description and the default unit.

PARAMETERS OF THE REFERENCE MODELS							
Model	$M_*$	$a$	$\rho_0$	$r_0$	DM profile	$M_h [M_\odot]$	$R_C$
v20	100	0.9	14.1	1.0	MIS	$1.5 \times 10^9$	1.2
v30	400	1.0	14.9	1.1	MIS	$1.9 \times 10^9$	1.2
v40	1000	1.4	12.7	1.4	MIS	$2.5 \times 10^9$	2.4
v50	2400	2.0	10.8	1.8	MIS	$3.3 \times 10^9$	2.4
v60	4000	2.0	9.4	2.2	MIS	$4.0 \times 10^9$	3.6
v70	6000	2.2	8.9	2.4	MIS	$4.7 \times 10^9$	3.6
v20b	100	0.9	23.8	1.2	Burkert	$0.7 \times 10^9$	1.2
v30b	400	1.0	23.8	1.2	Burkert	$0.8 \times 10^9$	1.2
v40b	1000	1.4	21.5	1.4	Burkert	$1.0 \times 10^9$	2.4
v50b	2400	2.0	18.1	1.8	Burkert	$1.6 \times 10^9$	2.4
v60b	4000	2.0	15.9	2.2	Burkert	$2.2 \times 10^9$	3.6
v70b	6000	2.2	15.0	2.4	Burkert	$2.6 \times 10^9$	3.6

Common parameters:

$$\hat{c}_s = 7 \text{ km s}^{-1}, f_{\text{SN}} = 3000 \text{ kpc}^{-2} \text{ Gyr}^{-1}, T_{\text{SN}} = 0.2 \text{ Gyr}, t_a = 0.04 \text{ Gyr}$$

Table 3.3: The meaning of the parameters and its units are described in the Table 3.2. The MIS in the column “DM profile” stands for “modified isothermal sphere” described by Eq. (3.12) and Burkert for profile defined by Eq. (3.15). The  $M_h = M_h(r < 10 \text{ kpc})$  is the total halo mass within the defined radius. To calculate the mass for MIS profile the Eq. (3.11) is used and for Burkert profile the Eq. (3.14). Parameters which are common for all models are listed below the table.

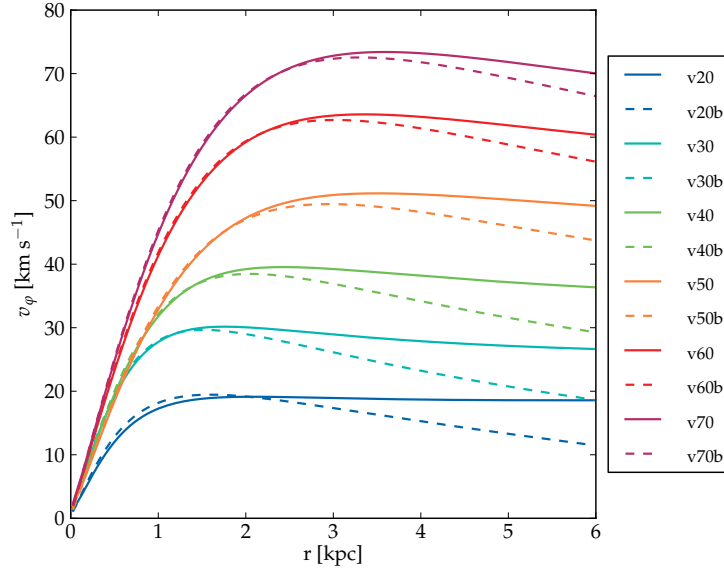


Figure 3.5: The rotation curves for the reference models. The solid lines mark the galaxies with “modified isothermal sphere” DM model and the dashed lines the phenomenological one proposed by Burkert (for details see Sec. 3.3).

### 3.7.2 Supernovae modulation

Using the reference models from previous section a new set is created, which regards to different star formation history. In this case only the parameters  $f_{\text{SN}}$ ,  $T_{\text{SN}}$  and  $t_a$  are changed, and the others are the same as in Table 3.3. The values of the parameters are set in a way that the number of supernovae,  $N_{\text{SN}}$ , in each model is the same, i.e.:

$$N_{\text{SN}} = f_{\text{SN}} T_{\text{SN}} \frac{t_a}{T_{\text{SN}}} = f_{\text{SN}} t_a = \text{const}, \quad (3.20)$$

but the  $t_a$  is longer than in the reference models. This configuration gives the same amount of energy input from SNe in all models and tests the dynamo action for objects which do not have strong starburst events peaked in time, but the star formation activity is lower but it lasts for longer times. The details of the models are presented in Table 3.4. The model name is correspond with the reference model but with a prefix of letter 'a' and a number which stands for fraction of SNe activity, i.e.  $t_a/T_{\text{SN}}$ .

### 3.7.3 Temperature of the ISM

Repeating the procedure form previous section I create models with different ISM temperatures. The temperature  $T$  of an ideal gas is described by the ideal gas law  $pV = NkT$ , where  $p$  is the pressure,  $V$  the volume and  $k$  the Boltzman's constant. If we assume that the ISM consists mostly from hydrogen atoms, i.e.  $N = V\rho/m_H$ , where  $m_H$  is the hydrogen mass. Substituting the pressure with the isothermal equation of state (Eq. 3.4), we find that:

$$kT = \frac{m_H c_s^2}{\gamma} = m_H \hat{c}_s. \quad (3.21)$$

Using this relation we can find that  $T = 4000$  K,  $T = 6000$  K and  $T = 8000$  K implies isothermal speed of sound equal to  $5.8 \text{ km s}^{-1}$ ,  $7 \text{ km s}^{-1}$  and  $8.1 \text{ km s}^{-1}$ , respectively. To test the dynamo dependence on the ISM temperature I setup a set of models for each of the above  $\hat{c}_s$  values utilizing the following reference models: v30, v30b, v40, v50, v60, v70. In total there is 12 new simulations.

PARAMETERS OF SNE MODULATION MODELS					
Model	Ref.	$f_{\text{SN}}$	$t_a$	$t_a/T_{\text{SN}}$	$\Sigma\text{SFR} [M_{\odot} \text{ yr}^{-1} \text{ kpc}^{-2}]$
a02v30	v30	3000	0.04	0.2	$4.7 \times 10^{-4}$
a02v40	v40				
a02v70	v70				
a02v30b	v30b				
a02v40b	v40b				
a02v70b	v70b				
a04v30	v30	1500	0.08	0.4	$2.3 \times 10^{-4}$
a04v40	v40				
a04v70	v70				
a04v30b	v30b				
a04v40b	v40b				
a04v70b	v70b				
a06v30	v30	1000	0.12	0.6	$1.6 \times 10^{-4}$
a06v40	v40				
a06v70	v70				
a06v30b	v30b				
a06v40b	v40b				
a06v70b	v70b				
a08v30	v30	750	0.16	0.8	$1.2 \times 10^{-4}$
a08v40	v40				
a08v70	v70				
a08v30b	v30b				
a08v40b	v40b				
a08v70b	v70b				

Table 3.4: Subsequent columns shows: the model name, the reference model name, the parameters of SNe modulation and the corresponding value of the surface density of the star formation rate according to Appendix A, assuming the model of the initial mass function from Kennicutt (1998). The parameters which are not mentioned here are the same as for the reference model from Table. 3.3.

## Results

In Section 3.7 I describe the detailed parameters of the dwarf galaxy models prepared for the purpose of this thesis, and in total there are 42 different setups. They were simulated on the computers supplied by the Polish Grid Infrastructure<sup>1</sup>. The main computations were done on the Zeus Supercomputer in ACC Cyfronet AGH. Zeus is a cluster platform with 13944 cores and 32TB of memory, connected over the Infiniband QDR. The core simulations (without the data analysis) took in total about 400 000 CPU hours. The visualisation, data analysis, code testing and debugging were performed on the Octopus cluster. Octopus is a system located in the Astronomical Observatory UJ built from 6 stations with 8 CPUs and 16GB of memory each. The visualization part and data plots are done using following Python modules: for reading the HDF5 files PyTables (Alted et al. 2002–), for operation on the arrays NumPy (Oliphant 2007) and for plotting the Matplotlib (Hunter 2007).

### 4.1 The ISM evolution

The supernovae is distributed according to the local density (Sec. 3.4). To verify this assumption a map of SNe distribution in the  $xy$  plane is plotted (Figure 4.1). The position of each supernova is tracked in the code, and after the whole simulation the number of explosions is summed over time. The distribution follows the density profile (as assumed), and the sharp cutoff at certain radius is caused by a density threshold which blocks the supernovae to explode in too dilute medium. Mostly dwarf galaxies do not have any structure such as spiral arms, and therefore the SNe explosions occurs in a whole disk. The presented result of SNe distribution is consistent with this statement.

The supernovae explosions influence the velocity field and can cause strong disturbance in the rotation curve as showed in Figure 2.8 for NGC 4449. To check the influence

---

<sup>1</sup><http://www.plgrid.pl>

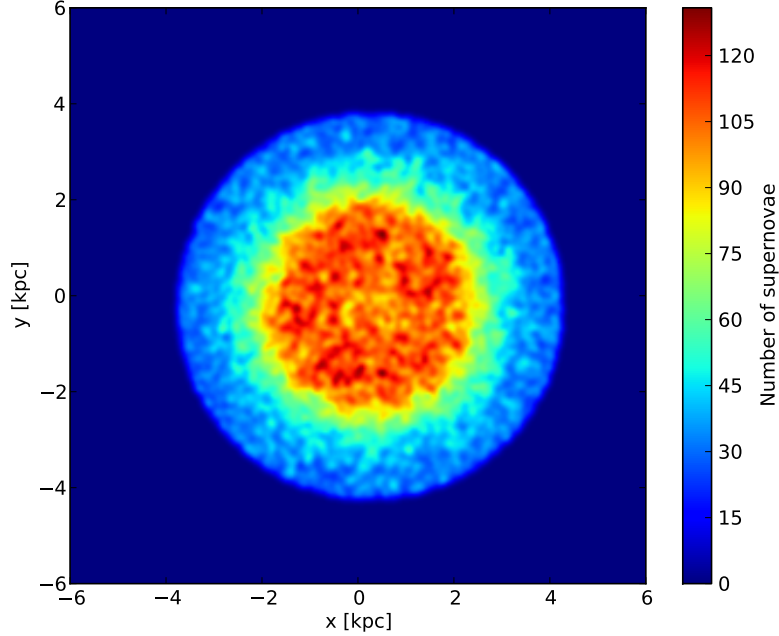


Figure 4.1: Number of supernovae explosion in  $xy$  plane summed over all simulation time for the model v40.

of SNe imposed to the system via the cosmic rays, the rotation curves for the reference models (Table 3.3) are plotted during one of the burst of SNe activity at  $t = 4.14$  Gyr (Figure 4.2). For slow rotation objects  $v_{\text{rot}} < 40 \text{ km s}^{-1}$  the influence is very low. Fast rotating objects however have highly disturbed rotation curve, especially the v70 and v70b models. The disturbances are not so strong as in the case of NGC 4449, but this can be explained by lower SNR in the model then it is observed in the galaxy. Also no other effects of extremely high SFR is taken in to account, e.g. the stellar winds which can deposit significantly amount of energy, mass and momentum in to the ISM (Leitherer et al. 1992).

Gas distribution in the disk for model v40 is shown in Figure 4.3. The first plot shows the initial state of the system at  $t = 0$ . There is only an azimuthal velocity component, i.e.  $v_z = 0$ . The next plots show the evolution of the ISM. Because of the supernovae activity the disk slightly expands in the  $xy$  plane and only small fluctuations appear. The snapshots at  $t = 4.10, 4.12$  and  $4.14$  Gyr show the disk while it is undergoing a burst of SNe explosions. The amount and size of fluctuations increase, but no prominent structures appear. Additionally, in the  $xz$  cuts one can see that the  $v_z$  component is directed away from the disk. For snapshots at  $t = 2.0$  and  $6.0$  Gyr, while there have not been any SNe explosions recently, the  $v_z$  direction is oriented towards the midplane of the disk. This represents a classic life cycle of the ISM: the SNe explosions drives a wind from the

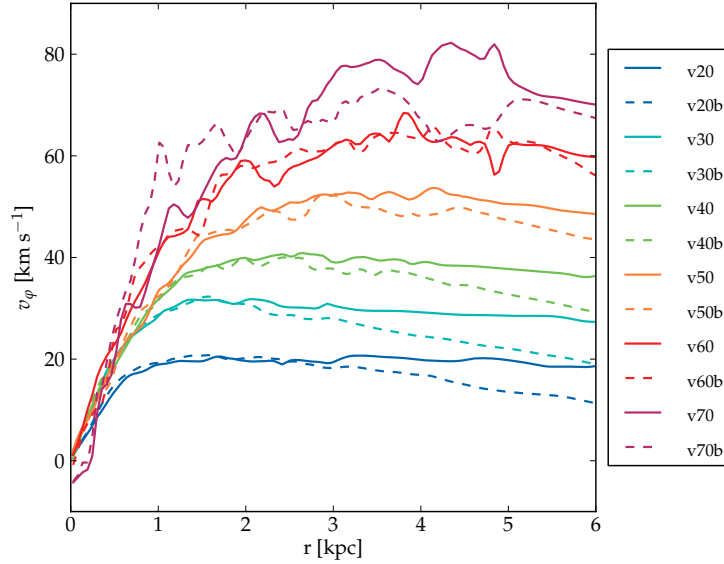


Figure 4.2: Rotation curves in  $t = 4.14$  Gyr for the reference models (Table 3.3) while they are ongoing SNe burst. For this period of time the SNe are active between 4.10 and 4.14 Gyr. The initial, non disturbed rotation curves are shown in Figure 3.5.

disk, and after they are stopped a part of the gas is flowing back to the disk. This forms a semi-closed cycle of the matter in a galaxy.

To show the evolution of the gas vertical structure in the galaxy the gas density for  $x = 0$  and  $y = 3$  kpc along the  $z$  direction is plotted at  $t = 0.0, 0.1, 0.2, 1.0, 3.5, 6.0$  Gyr for model v40 (Figure 4.4). The first (purple) line shows the initial condition while the system is in hydrostatic equilibrium. For the next timesteps the density in the disk midplane slightly decreases, but in the outskirts ( $z = 3$  kpc) the density increase almost by two orders of magnitude. This implies that the gaseous disk becomes more puffy because of the turbulence driven by the injected supernovae.

The initial state of the cosmic ray energy follows the density distribution (Figure 4.5). After the system evolves and the supernovae explode supplying additional energy some fluctuations appear. Weak and wide streams of cosmic ray energy form in the vertical direction; they start from the disk midplane and span up to the top and bottom domain boundaries (see Figure 4.5 at  $t = 2.0$  Gyr). This can be the channels of transferring the cosmic ray energy out of the system. In the snapshots while the supernovae are active ( $t = 4.12$  and 4.14 Gyr) the traces of explosion sites can be seen.

Above features of the ISM, rotation curves, supernovae distribution and cosmic ray gas evolution is common for other models described in this work. Only the size of the disk and the radius of the supernovae distribution is scaling with the mass of the galaxy and therefore this description is only limited to the model v40.

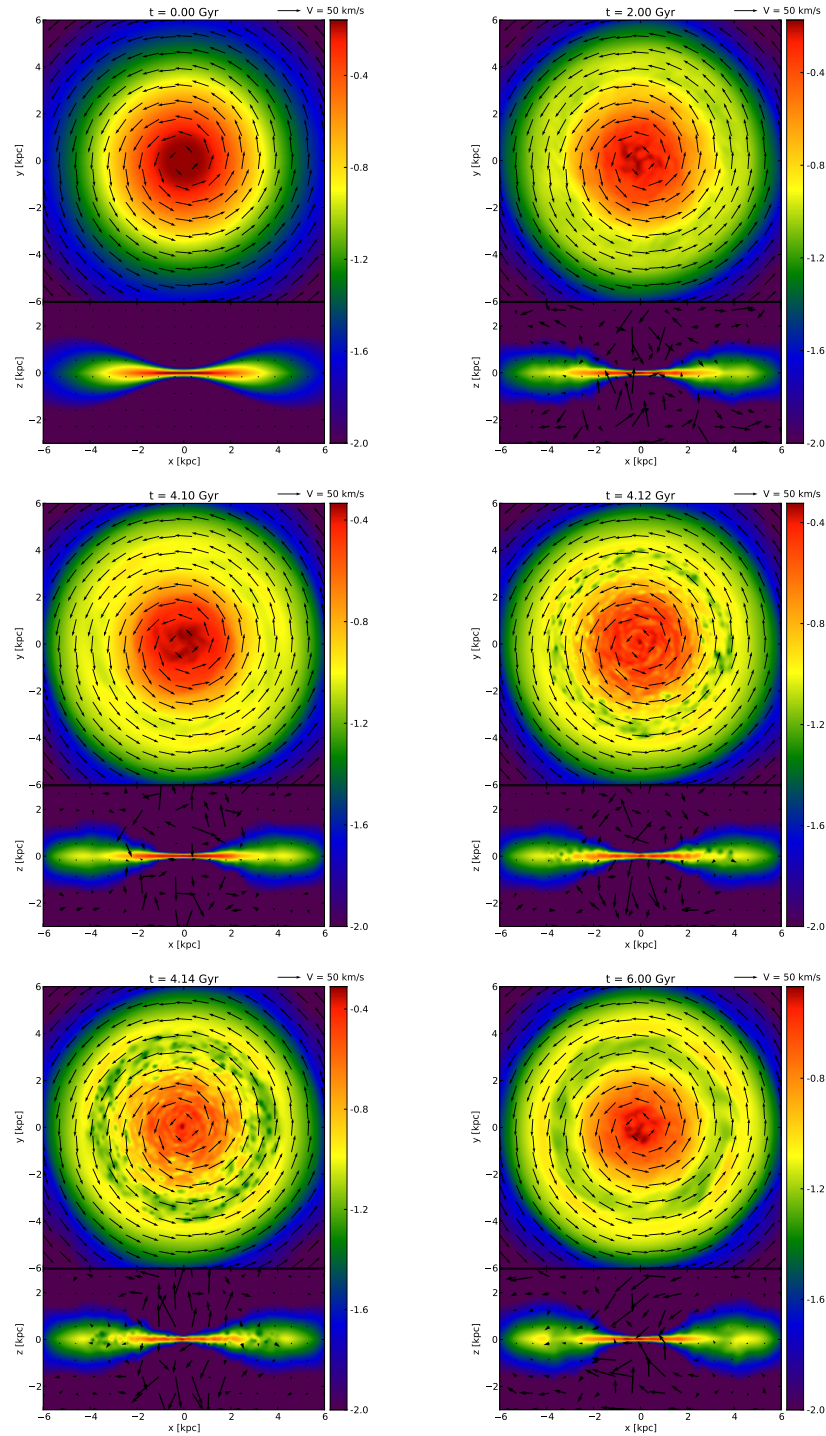


Figure 4.3: Snapshots of the gas an velocity evolution in a dwarf galaxy. The first snapshot shows the initial state and the others the system in the subsequent time steps for model v40. Each snapshots consists of two plots, the upper map shows the midplane of the disk and the lower one the vertical cut. The colours show the logarithm of the gas distribution in units of the hydrogen mass per cubic centimetre,  $1.0 n_H \text{ cm}^{-3}$  and the arrows show the velocity vectors in  $\text{km s}^{-1}$ . The vectors in  $xz$  cuts are multiplied by a factor of 5 to improve its readability.

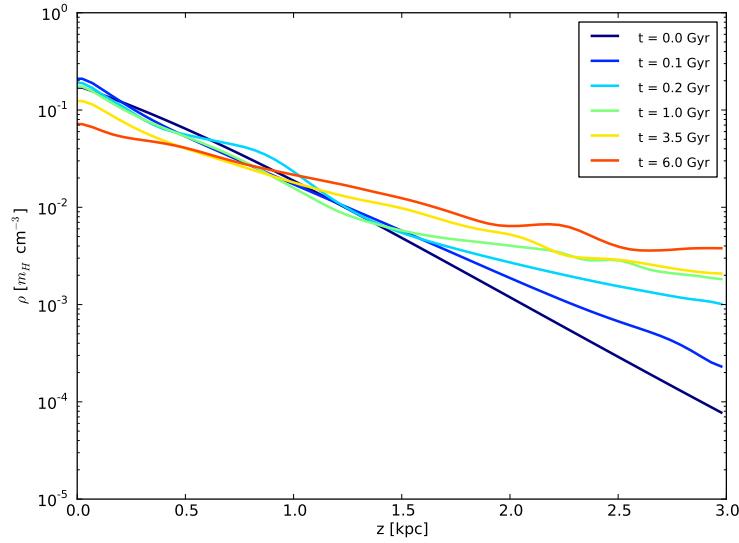


Figure 4.4: Vertical distribution of the gas density in the model v40 for selected timesteps. The line for  $t = 0$  Gyr represents the initial condition in the model.

## 4.2 Magnetic field evolution

### 4.2.1 Dependence on the rotational velocity

A quantity by which we can measure the growth of the magnetic field in the system is the magnetic field energy, i.e.  $E_B = B^2/2\mu_0$  and the magnetic azimuthal flux,  $B_\phi$ . The initial value (at  $t = 0$ ) of the  $E_B$  is zero and then the dynamo is seeded by injecting small magnetic dipoles connected with the supernova explosion. The evolution of  $E_B$  for models with different rotation curves is showed in Figure 4.6 (left panels). The first three peaks which can be seen in  $E_B$  evolution plots are due the injected magnetic field, and after the  $t_{\text{mag}} = 0.6$  Gyr this injection is stopped. In the case where dynamo operates the magnetic field supplied by stars seems to be negligible. Also from the numerical point of view, the injected magnetic field increases the  $\nabla \cdot \mathbf{B}$  and therefore one need to limit the amount of injected dipoles.

The slowest rotating galaxy models (v20 and v20b) do not show any amplification of the  $E_B$  (Fig. 4.6 a). Initially the  $E_B$  in the v20 model drops more than the v20b, but after the 6 Gyr they reach the same value. The v30 model starts to slightly amplify the magnetic energy while the v30b exhibits quite strong exponential growth. For these four models the ones which use the Burkert's profile as the dark matter model the final value is bigger than in the other case. To measure the effectiveness of the large scale dynamo also the total flux of the azimuthal magnetic flux is calculated (see right panels of Figure 4.6). The models v20b and v30b amplifies the azimuthal flux much more than the v20 and v30 ones (Fig. 4.6 b). The last two examples only maintain the  $B_\phi$  component which was

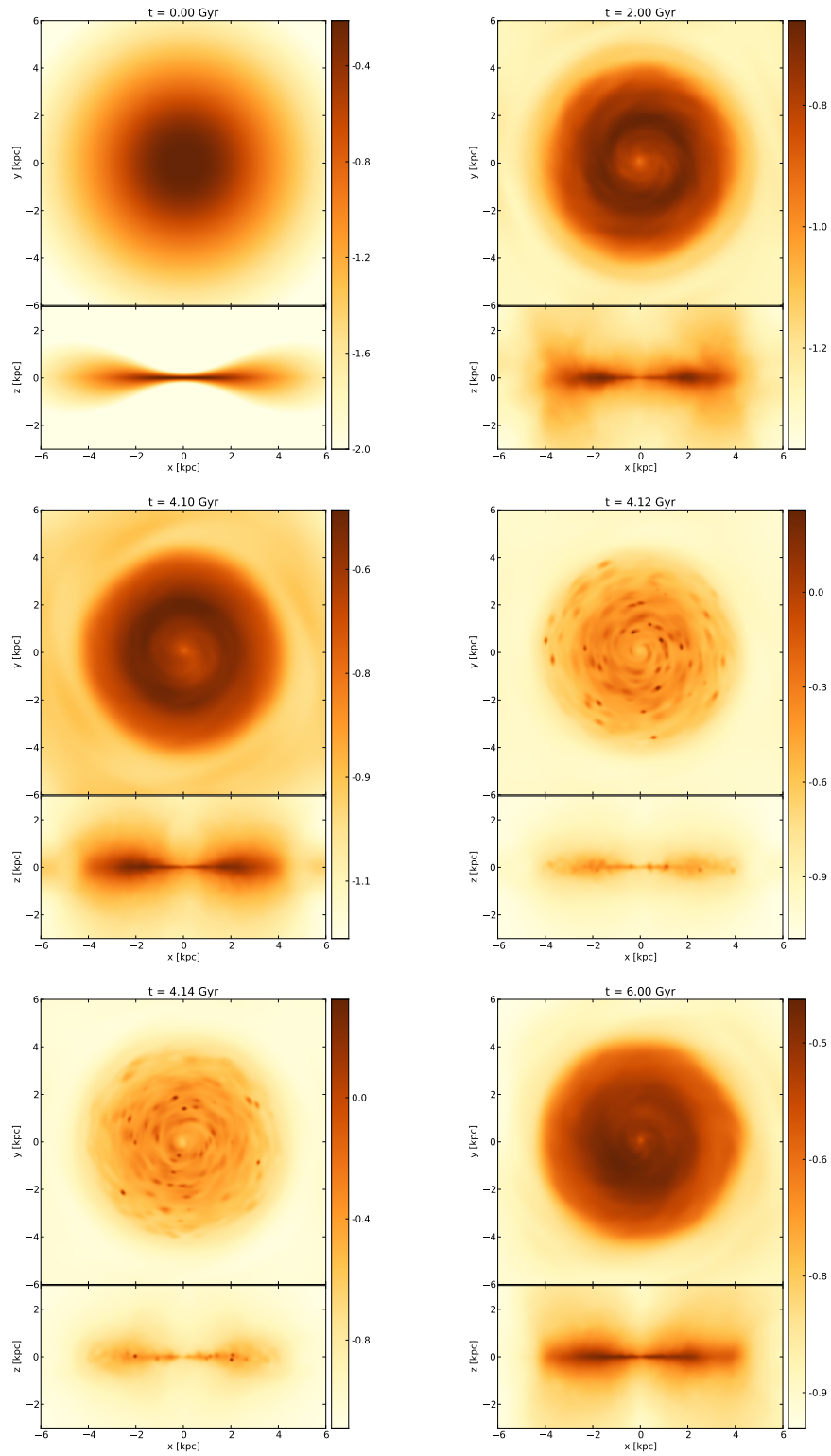


Figure 4.5: The evolution of the cosmic ray energy. The subsequent plots show the snapshots of cosmic ray energy distribution at particular time steps for model v40. Each snapshot show the energy distribution in the disk midplane and in the  $xz$  plane. The cosmic ray energy is expressed in  $\text{eV cm}^{-3}$  unit.

injected through the magnetized SNe explosions. The model v30 after  $t = 2$  Gyr starts to change the sign of the total azimuthal flux and after 0.5 Gyr the reversed sign stabilizes.

The models with mid rotating velocity show much stronger amplification of the magnetic field (Fig. 4.6 c, d). The models v40, v40b and v50b follow almost the same evolution of the  $E_B$  and  $B_\phi$ . The growth of both quantities is exponential in time. The v50 model however amplifies the magnetic field energy to two orders of magnitude lower value. Additionally the plot show some sawtooth pattern, which repeats in time, and after the  $t = 3.5$  Gyr the peaks are damped. Similar pattern is found in the  $B_\phi$  evolution but with significantly lower amplitude. In both cases the peaks are related with the activity of supernovae.

The evolution of  $E_B$  and  $B_\phi$  of the models with rotation speed around  $60 \text{ km s}^{-1}$  (Fig. 4.6 e, f) reach approximately the same value as the v40, v50 and v50b. In the case of the v60 model also the sawtooth pattern appears, but without any damping before the end of the simulation. The models with the fastest rotation speed show similar pattern, especially the v70 model, the evolution of the magnetic energy shows the exponential growth but at  $t = 5$  Gyr the amplification starts to saturate. The saturation also reveals for v70b model. The azimuthal flux also starts to saturate however strong oscillations appears at the end of the simulation.

The evolution of the azimuthal magnetic flux component for v40 model is showed in Figure 4.7. At the beginning of the simulation the galaxy is seeded via the magnetized supernovae explosions in the very first burst which occurs between  $t = 0.10$  and  $0.14$  Gyr. In the plot  $xy$  appear randomly positioned spots of positive (blue colour) and negative (red colour)  $B_\phi$  (at  $t = 0.15$  Gyr). In the  $xz$  plot similar pattern reveals but only very close to the disk midplane, i.e. there is no structures in the halo. After the next burst of SNe activity ( $t = 0.30 \div 0.34$  Gyr) also a randomly positioned blue, red spots appears due to the magnetized explosions, but some background spiral pattern starts to emerge. This effect is related to the magnetic diffusion, which cause the small "magnetic islands" to merge and form larger structures. The differential rotation shear the radially aligned structures and forms a spiral pattern. The  $B_\phi$  component is also present in the galaxy halo in the form of channels of oppositely directed azimuthal flux (alternating blue, red streams).

The spiral structure of oppositely directed  $B_\phi$  is prominent at  $t = 0.75$  Gyr. However in the central part of the galaxy the  $B_\phi$  have mostly negative sign. In the  $xz$  plot also the disk midplane is occupied by the negative  $B_\phi$ . However in the galaxy halo appear many patches of oppositely directed magnetic field. After the next 0.25 Gyr the positive azimuthal flux in the disk starts to disappear from the galaxy disk, but the structure in the halo is still very patchy. At  $t = 2.00$  Gyr the  $B_\phi$  have only the negative sign. In the halo however the patches of oppositely oriented fluxes are forming more coherent shape and the positive sign is more dominant.

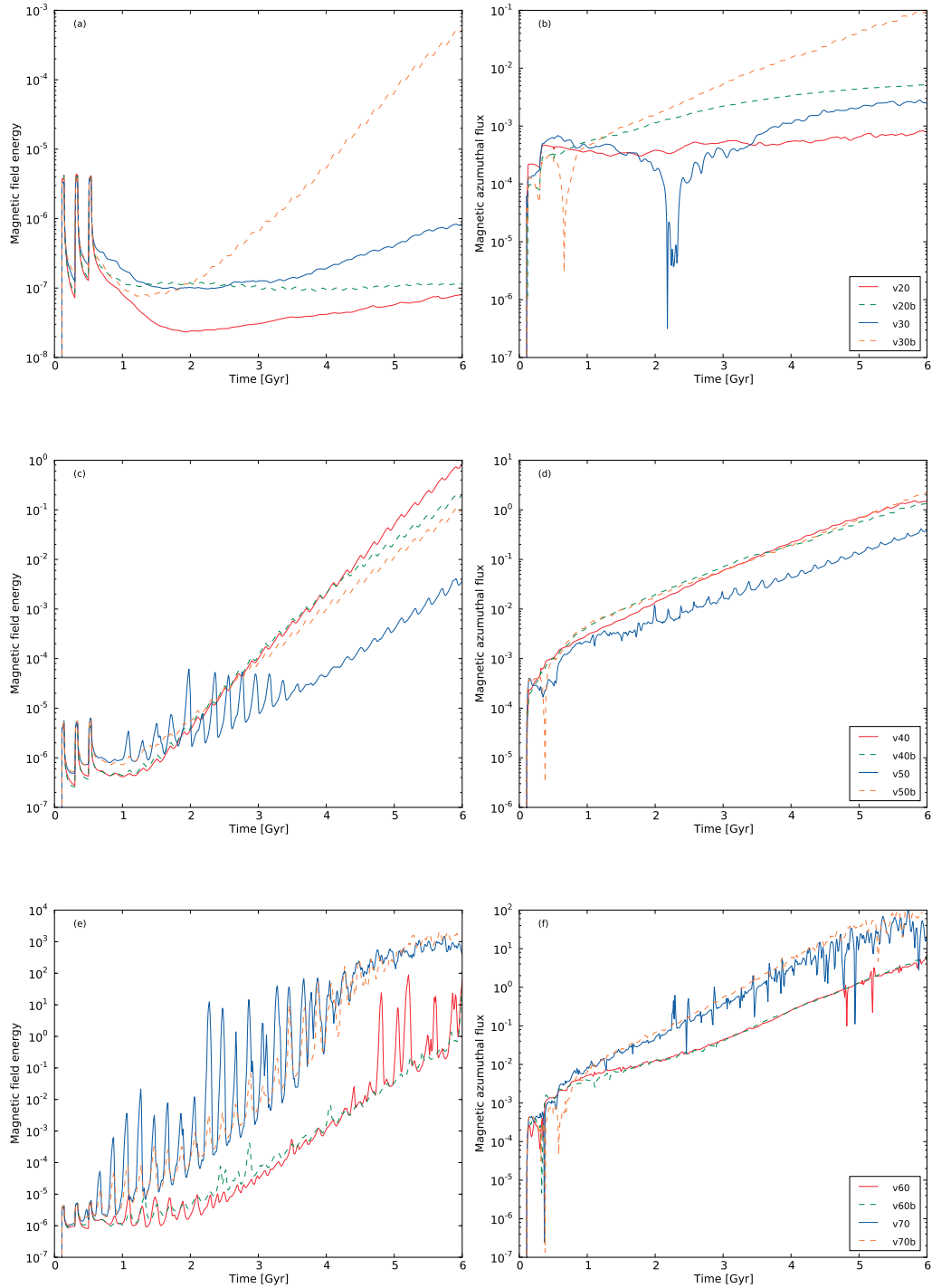


Figure 4.6: The evolution of the magnetic field for models with different rotation speed. The left panels show the total magnetic field energy evolution and the right ones the azimuthal magnetic flux evolution. The values are expressed in code units. To use the logarithmic scale for the azimuthal flux plot the absolute value is plotted, so if the flux starts to rapidly drop to very low values and then rapidly to grow this is a signature of sign turnover.

At the end of the simulation in the disk is only the negatively oriented magnetic azimuthal flux. The magnitude is the strongest in the central part and it slowly decrease with the radius. The negatively oriented flux is mostly located in the midplane of the galaxy, but it extends also to some vertical height in a form of a disk “corona”. The positively oriented magnetic flux is located in the halo, but only within the radius of the disk. This cylinder of positive magnetic flux reaches the top and bottom domain boundaries in the within the radius of 2 kpc from the galaxy centre.

To complete picture of the magnetic field structure evolution in the system the magnetic field energy is showed with over plotted arrows of its direction (Figure 4.8). At  $t = 0.15$  Gyr the system have mostly randomly oriented magnetic field and lots of spots of high  $B^2$  which correlates with the sites of the SNe explosions. In the  $xz$  plane the structure of the magnetic field is dominated by a few dipolar magnetic fields injected with the very first supernovae. Note that the values of the  $B^2$  in the halo are very low. After the next injection of the magnetized supernovae explosions ( $t = 0.35$  Gyr) the magnetic field in the disk plane and in the vertical cut is very random. A weak, first spiral arms of the  $B^2$  appear at the disk outskirts but with no relation to the magnetic field direction. In the  $xz$  plane one can see that some streams of the magnetic energy are formed reaching the top and bottom boundary of the domain. The next two panels at  $t = 0.75$  and  $1.00$  Gyr show that the magnetic field starts to be more ordered in the galactic disk plane. Spiral arms of the magnetic energy appear and the direction of the magnetic field is correlated with the spiral arms. Some spiral arms have oppositely oriented magnetic field with respect to the neighbouring ones. In the halo the magnetic field is still randomly oriented. The streams of the magnetic energy evolved and now occupy the space above and below the disk. At  $t = 2.00$  Gyr the magnetic energy spiral arms are winding up but now the orientation of the vectors are coherent, no oppositely directed magnetic filed in the spiral arms. In the halo the magnetic field is still randomly oriented. The final stage after the 6.00 Gyr of simulation show a magnetic field which is mostly azimuthal in the disk plane. The magnetic energy is the highest in the central part of the galaxy and it is decreasing with radius. In the  $xz$  plane the strongest magnetic field can be found in the disk plane. The orientation of the magnetic field in the halo is still random. The streams of the magnetic field energy in the halo are still very strong, but they are mostly present within a cylinder of 2 kpc radius.

The previously described model v40 is the one which is characterized by a positive dynamo action. One of the model which do not amplify the magnetic field energy is v20. The evolution of the magnetic field structure for this model is shown in Figure 4.9. Initially, at  $t = 1.0$  Gyr to structure of  $B_\phi$  and  $B^2$  is very similar to those found in the v40 model. However in the next timesteps we can see that the magnetic spiral arms have still oppositely oriented magnetic fields. The magnetic energy is mostly concentrated in the centre of the galaxy and it is dominated by the  $B_\phi$  component. Interesting results

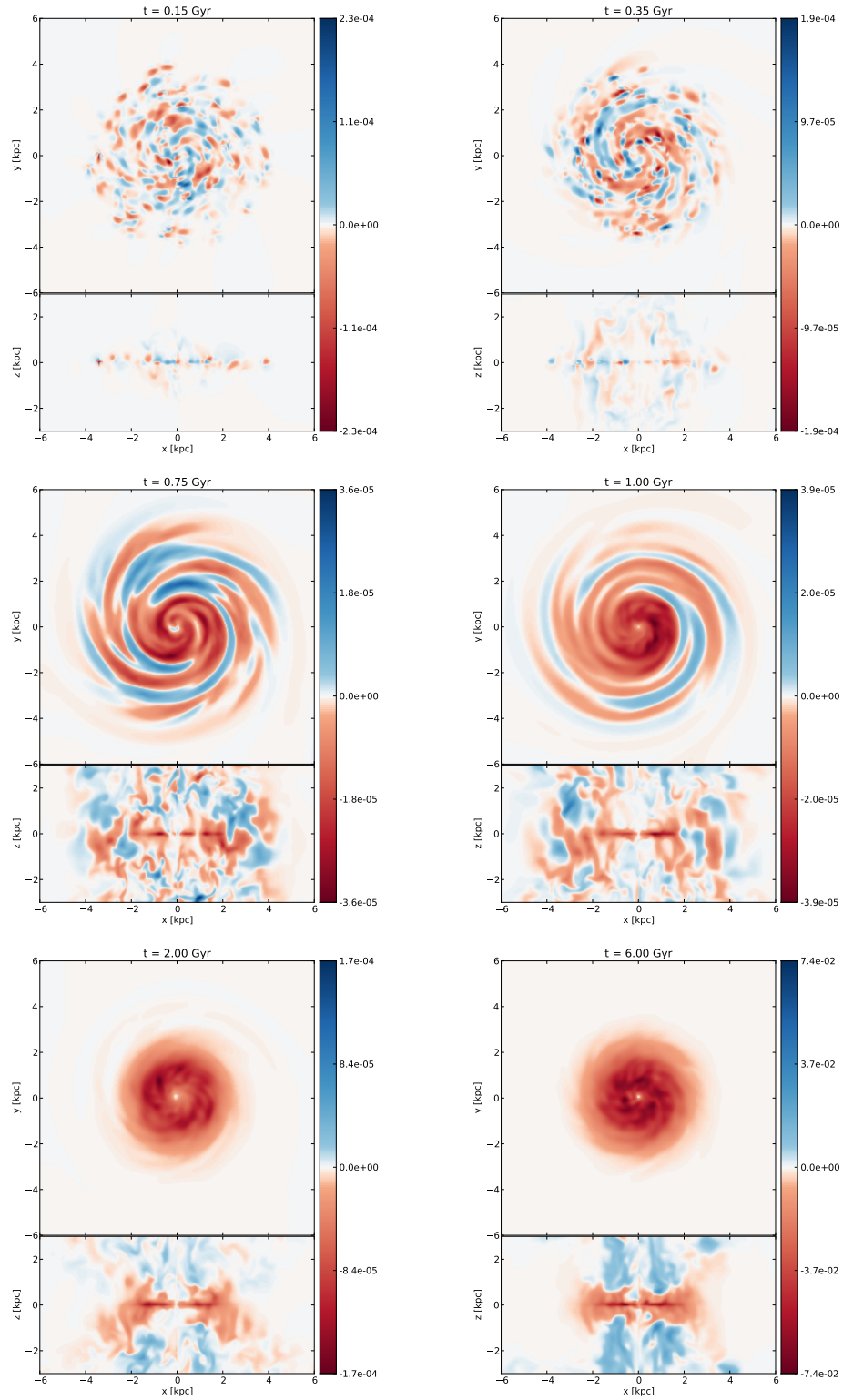


Figure 4.7: Evolution of the logarithm of magnetic azimuthal flux. The subsequent plots show the  $xy$  and  $xz$  cuts plane of the simulated domain for model v40 at  $t = 0.15, 0.35, 0.75, 1.00, 2.00, 6.00$  Gyr. The magnetic field is expressed in  $\mu\text{G}$ .

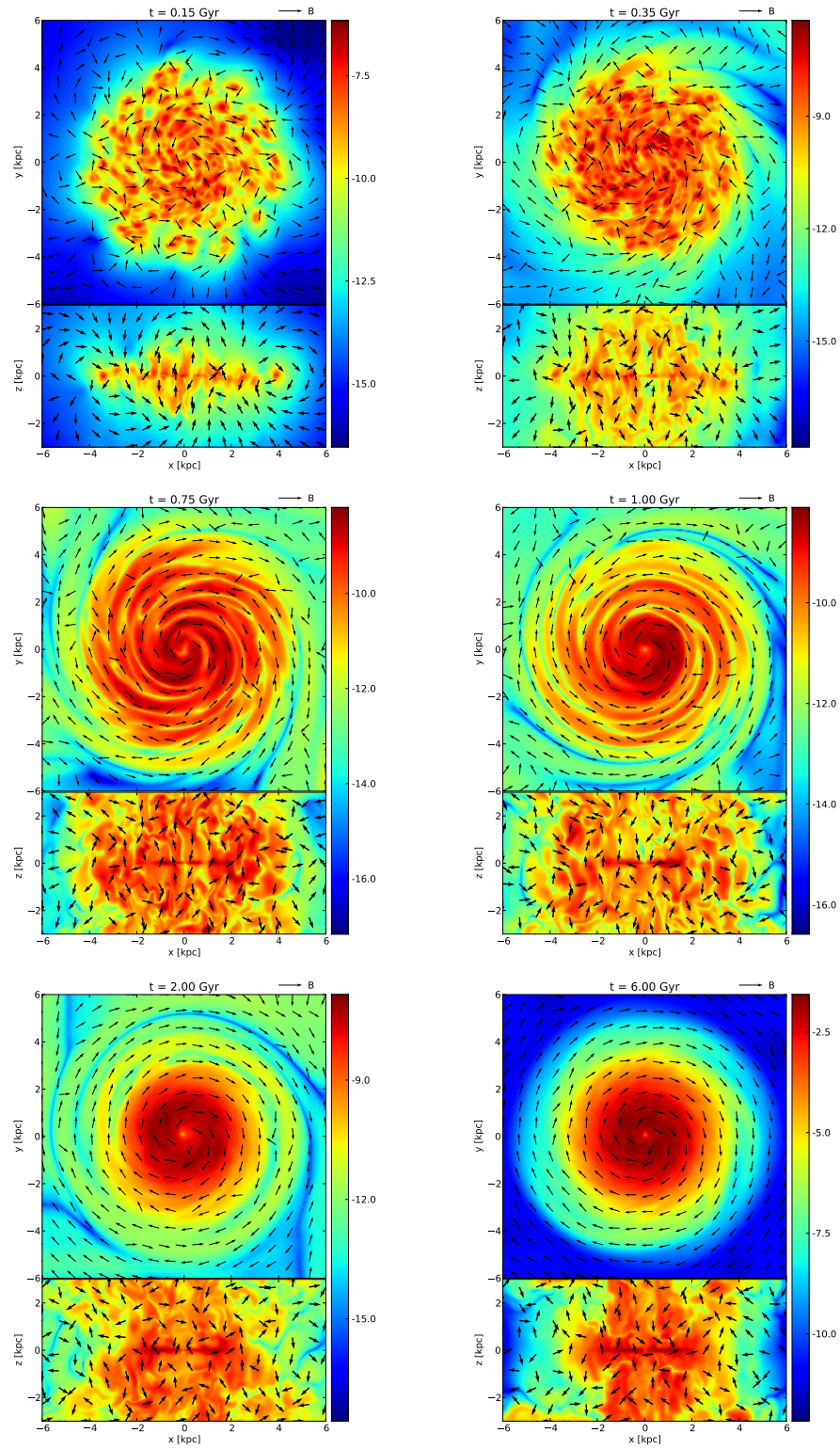


Figure 4.8: Evolution of the magnetic field. The subsequent plots show the  $xy$  and  $xz$  cut plane of the simulated domain for model v40 at  $t = 0.15, 0.35, 0.75, 1.00, 2.00, 6.00$  Gyr. The colors show the logarithm of magnetic field energy and the vectors of its direction. The length for all vectors is set to 1.

RESULTS FOR THE REFERENCE MODELS

Model	$t_{B^2}^e$ [Gyr]	$t_{\phi}^e$ [Gyr]	$\max(B_{\phi})$ [ $\mu\text{G}$ ]
v20	3.31	5.55	$1.27 \times 10^{-4}$
v20b	-104.77	2.64	$0.97 \times 10^{-4}$
v30	2.14	2.24	$4.93 \times 10^{-4}$
v30b	0.47	0.96	$2.14 \times 10^{-2}$
v40	0.33	0.81	0.76
v40b	0.37	0.88	0.38
v50	0.57	0.99	$3.46 \times 10^{-2}$
v50b	0.41	0.82	0.23
v60	0.27	0.68	28.94
v60b	0.28	0.65	26.50
v70	0.19	0.57	25.17
v70b	0.19	0.48	37.47

Table 4.1: The subsequent columns show: the model name, the  $e$ -folding time of the magnetic field energy ( $t_{B^2}^e$ ), the  $e$ -folding time of the magnetic azimuthal flux ( $t_{\phi}^e$ ) and the maximal value of the  $B_{\phi}$  in the galaxy disk.

seem to evolve in the vertical domain cut. In the disk midplane the  $B_{\phi}$  component is very weak. In the halo however very strong spots of azimuthal flux appear which are oppositely directed with respect to the disk midplane. For  $z > 0$  the  $B_{\phi}$  have positive sign and for  $z < 0$  negative. The magnetic field energy plots show that this components below and above the disk is very dominant.

A characteristic number of a magnetic dynamo is the  $e$ -folding time,  $t_e$ . It measures the growth rate of the magnetic field in a following manner:

$$t_e = \frac{t_2 - t_1}{\log(q(t_2)/q(t_1))}, \quad (4.1)$$

where  $t_1$  and  $t_2$  are the points in time for which the growth rate is measured, and  $q(t)$  is the investigated quantity, e.g. magnetic energy. The  $e$ -folding times for each model for magnetic field energy and the total azimuthal magnetic flux are presented in Table 4.1. The results show that models v20, and v30b have very long  $e$ -folding times of the order of few Gyr. The model v20b show that the  $B^2$  is almost constant for whole simulation but the  $B_{\phi}$  component is growing. This suggest that the dynamo do not enhanced the magnetic field but the global rotation is ordering the initially random magnetic field structure. The other models show the  $e$ -folding times between 0.19 and 0.57 Gyr for  $B^2$  and between 0.48 and 0.99 Gyr for the  $B_{\phi}$  component. In general the growth rate is faster for faster rotation objects. The generated regular magnetic field in the disk, which can be quantified by its maximal value of the  $B_{\phi}$  is about tens of  $\mu\text{G}$  and for faster rotating objects is above 25  $\mu\text{G}$ .

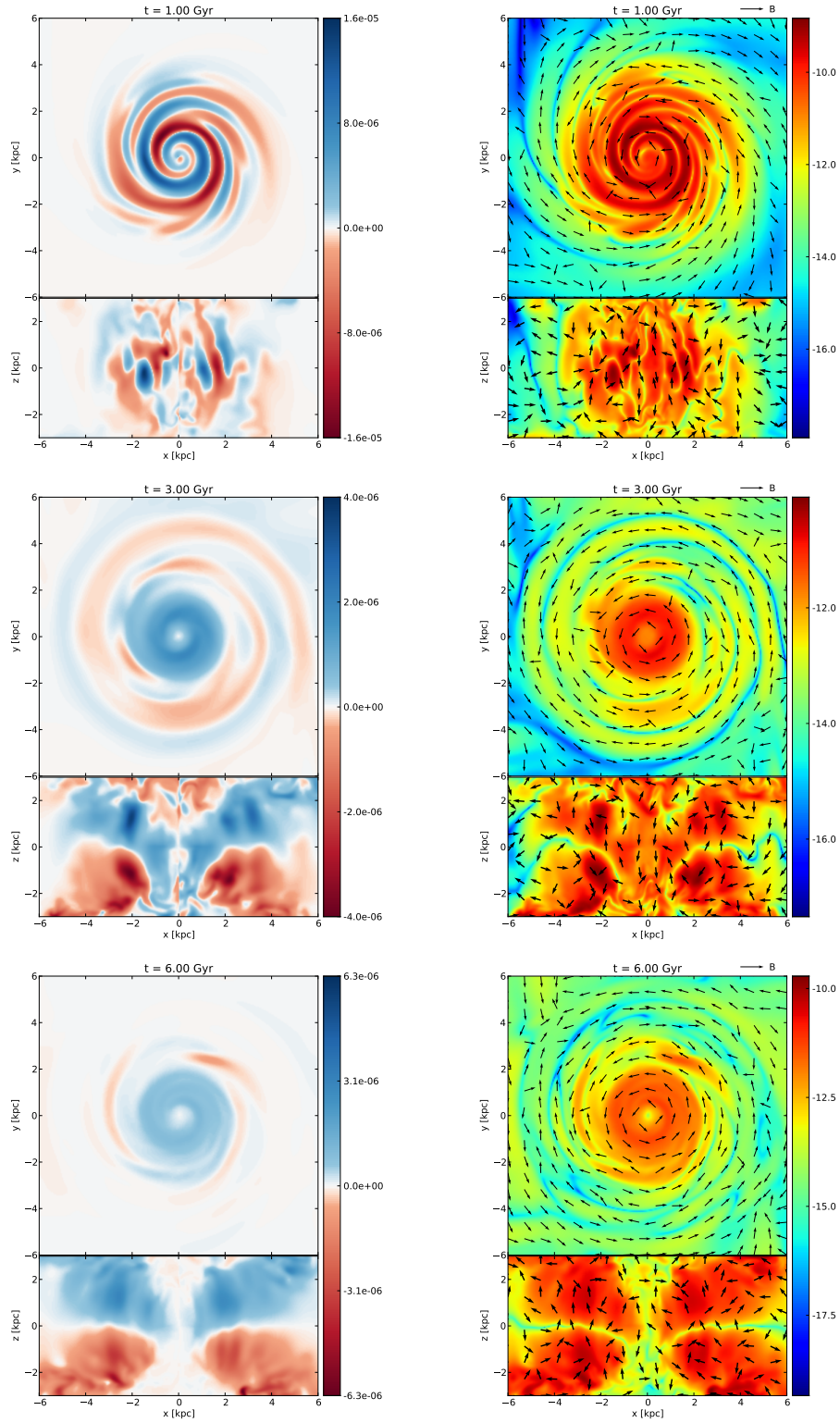


Figure 4.9: Evolution of the magnetic field for model v20. The subsequent plots show the  $xy$  and  $xz$  cuts of the magnetic azimuthal flux and magnetic energy at  $t = 1.0, 3.0, 6.0$  Gyr. The left panels show the evolution of  $\log(B_\phi)$  expressed in  $\mu\text{G}$ . The right panels show in colours the  $\log(B^2)$  and the vectors of the magnetic field. The length of all vectors is set to 1.

### 4.2.2 Dependence on the SN modulation

To test the dynamo dependence on the supernovae modulation models with different modulation types has been prepared. In this case the modulation period is common for all models but the duration of the SN activity is extended. The detailed parameters of these models are summarised in Table 3.4. The results of the simulations are shown in Figures 4.10 and 4.11 for models with DM halo described by “the modified isothermal sphere” (3.12) and Burkert’s profile (3.15), respectively.

The models a02v30, a06v30 and a08v30 show very similar evolution pattern in magnetic field energy and azimuthal flux (Fig. 4.10 a, b). However the magnetic energy in the case of the model a04v30 is amplified to greater value, by a factor of about 10. Also the azimuthal flux evolution do not show any strong dips, which are a mark of the field reversal. The corresponding models with Burkert’s DM profile show strong deviations from each other. The magnetic field energy and azimuthal flux for models a02v30b and a04v30b show very similar evolution pattern (Fig. 4.11 a, b). The weakest growth of the magnetic energy is found for model a06v30b. Also in the case of this model the azimuthal flux is reversed few times not only in the beginning of the simulation. The model a06v30b is in between the previous two models and the last one. The magnetic energy is amplified to a value by a factor of 12 lower than the a02v30b and a04v30b and the azimuthal flux only by a factor of 2.

The models with  $v_{\text{rot}} \simeq 40 \text{ km s}^{-1}$  show very similar evolution of magnetic energy and azimuthal flux (Fig. 4.10 c, d). The final values of  $E_B$  is about 0.1 and  $B_\phi$  about 1.0. The models with Burkert’s DM profile follows very closely the same evolution pattern. Only the models a04v40b and a06v40b (Fig. 4.11 c, d) amplifies the magnetic energy to a lower value by a one order of magnitude. This also applies to the magnetic azimuthal flux evolution.

In the case of the fastest rotating galaxies with  $v_{\text{rot}} \simeq 70 \text{ km s}^{-1}$  the evolution of  $E_B$  and  $B_\phi$  for different modulation times follows very closely the same evolution pattern (Fig. 4.10 e, f and 4.11 e, f). The final value at  $t = 6 \text{ Gyr}$  of the magnetic energy is  $10^3$  and the azimuthal flux  $10^2$ .

For these group of models also the  $e$ -folding times are calculated (Table 4.2). The results show that models with  $v_{\text{rot}} \simeq 30 \text{ km s}^{-1}$  have very different growth rate characteristics. The growth rate in the models a02v30, a08v30 and a06v30b are as long as 2-3 Gyr for the magnetic energy. The azimuthal flux is also generated in very slow way, and in the case of a08v30 even starts to decay. The  $e$ -folding times for  $E_B$  and  $B_\phi$  for models a04v30, a06v30, a08v30b is about 1 Gyr and 1.5 Gyr, respectively. The models a02v30b and a02v30b amplify the magnetic energy by a factor of  $e$  in about 0.5 Gyr and azimuthal flux in about 1.0 Gyr. These two models are the fastest from this group. The maximal azimuthal flux for this group of models is about  $10^{-3}$ – $10^{-2} \mu\text{G}$ .

Galaxies with  $v_{\text{rot}} \simeq 40 \text{ km s}^{-1}$  show very coherent evolution pattern with almost no

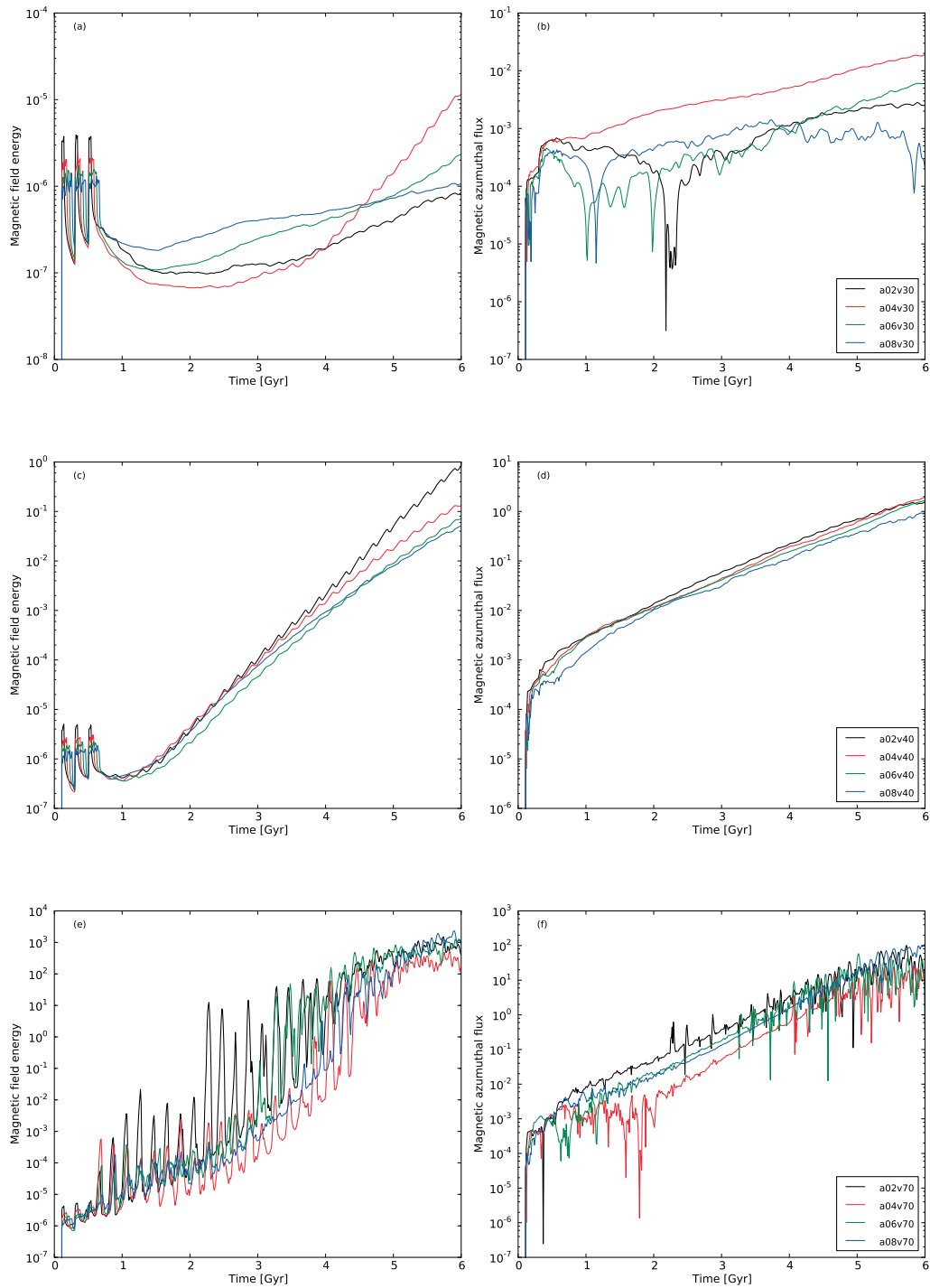


Figure 4.10: The evolution of the magnetic field for models with different rotation speeds and modulation times. The left panels show the total magnetic field energy evolution and the right ones the azimuthal magnetic flux evolution. The values are expressed in code units. To use the logarithmic scale for the azimuthal flux plot the absolute value is plotted, so if the flux starts to rapidly drop to very low values and then rapidly to grow this is a signature of sign turnover.

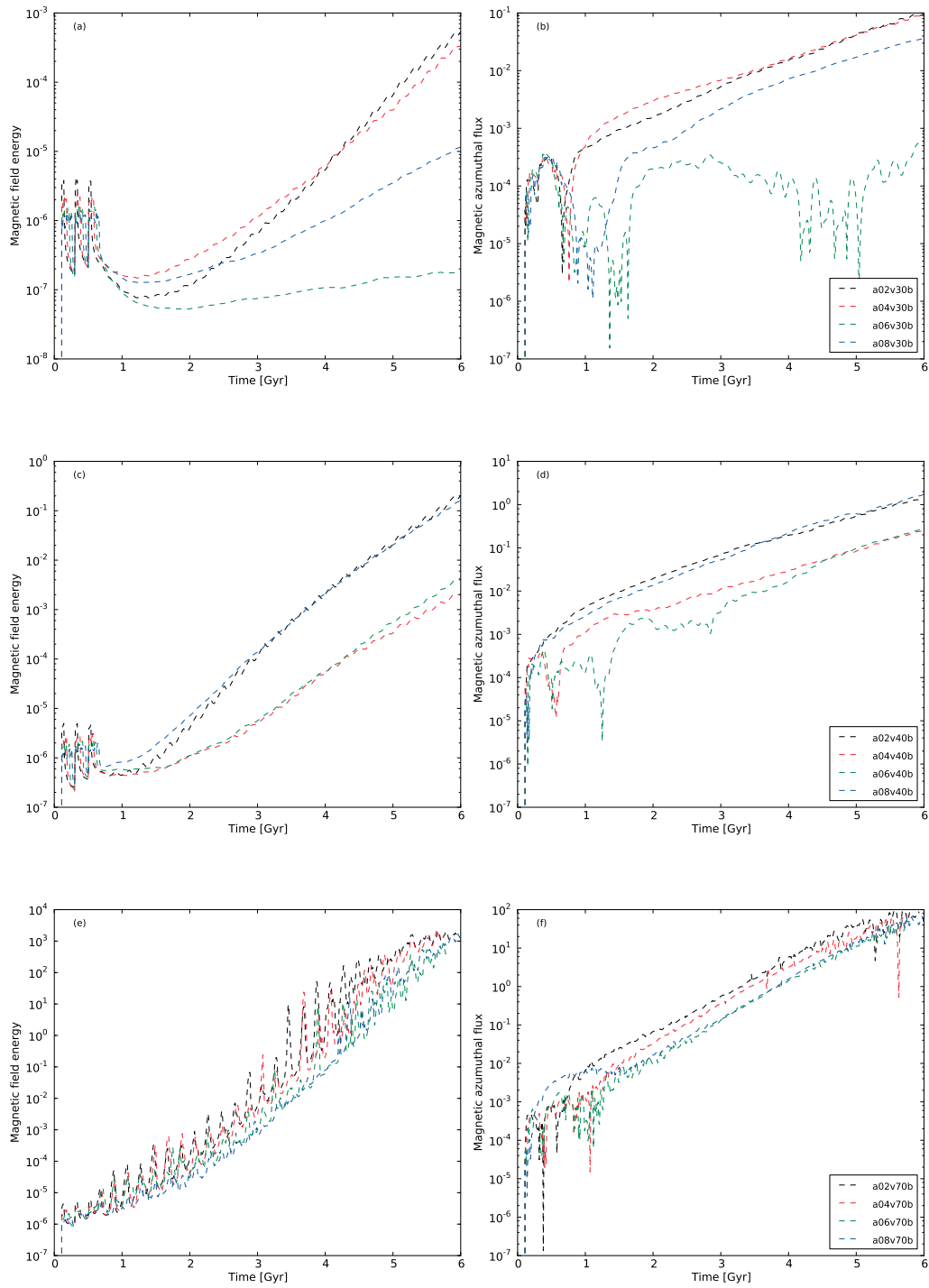


Figure 4.11: The evolution of the magnetic field for models with different rotation speeds and modulation times. The left panels show the total magnetic field energy evolution and the right ones the azimuthal magnetic flux evolution. The values are expressed in code units. To use the logarithmic scale for the azimuthal flux plot the absolute value is plotted, so if the flux starts to rapidly drop to very low values and then rapidly to grow this is a signature of sign turnover.

RESULTS FOR MODELS WITH DIFFERENT SN MODULATION			
Model	$t_{B^2}^e$ [Gyr]	$t_\phi^e$ [Gyr]	$\max(B_\phi)$ [ $\mu\text{G}$ ]
a02v30	2.14	2.24	$0.49 \times 10^{-3}$
a04v30	0.78	1.75	$2.73 \times 10^{-3}$
a06v30	1.37	1.72	$0.94 \times 10^{-3}$
a08v30	2.70	-5.32	$0.38 \times 10^{-3}$
a02v30b	0.47	0.96	$2.14 \times 10^{-2}$
a04v30b	0.56	1.16	$1.61 \times 10^{-2}$
a06v30b	3.28	4.22	$0.16 \times 10^{-3}$
a08v30b	0.94	0.98	$0.28 \times 10^{-2}$
a02v40	0.33	0.81	0.76
a04v40	0.39	0.78	0.26
a06v40	0.38	0.79	0.22
a08v40	0.42	0.89	0.16
a02v40b	0.37	0.88	0.38
a04v40b	0.53	0.93	$3.01 \times 10^{-2}$
a06v40b	0.48	0.79	$4.93 \times 10^{-2}$
a08v40b	0.40	0.82	0.30
a02v70	0.19	0.57	25.17
a04v70	0.18	0.46	17.52
a06v70	0.18	0.39	31.78
a08v70	0.17	0.44	29.72
a02v70b	0.19	0.48	37.47
a04v70b	0.20	0.51	32.17
a06v70b	0.23	0.45	23.43
a08v70b	0.21	0.44	29.75

Table 4.2: The subsequent columns show: the model name, the  $e$ -folding time of the magnetic field energy ( $t_{B^2}^e$ ), the  $e$ -folding time of the magnetic azimuthal flux ( $t_\phi^e$ ) and the maximal value of the  $B_\phi$  in the galaxy disk.

dependence on the supernovae modulation times. The  $e$ -folding times for magnetic energy is in range of 0.33–0.53 Gyr and for  $B_\phi$  0.78–0.93 Gyr. Mostly for all these models the maximal azimuthal flux is about 0.3  $\mu\text{G}$  except for a02v40 where it is 0.76  $\mu\text{G}$ . Only two models a04v40b, a06v40b reach the  $\max(B_\phi) \sim 10^{-2}$   $\mu\text{G}$ .

The fastest rotating models with  $\nu_{\text{rot}} \simeq 70$  km s $^{-1}$  also do not show any dependence on the supernovae modulation. The  $t_{B^2}^e$  is about 0.2 Gyr and  $t_\phi^e \sim 0.45$  Gyr. The maximal azimuthal flux generated in the system is between 17 and 37  $\mu\text{G}$ .

### 4.2.3 Dependence on the speed of sound

The model of the cosmic ray driven dynamo in dwarf galaxies is also simulated with different speed of sounds (see Sec. 3.7.3). The evolution of  $E_B$  and  $B_\phi$  for models with  $c_s = 5.8, 7.0$  and 8.1 km s $^{-1}$  and  $\nu_{\text{rot}}$  from 30–70 km s $^{-1}$  is shown in Figures 4.12 and 4.13.

The dwarf galaxy models which rotates as fast as about 30 km s $^{-1}$  (Fig. 4.12 a, b, c

and d) show that the magnetic field evolution depends on the  $c_s$  and the shape of the rotation curve, which is determined by the DM profile. The  $E_B$  in the c58v30 and c58v30b models follows the same evolution pattern, initially injected random magnetic field is exponentially amplified to a energy of 0.1 and the azimuthal flux about 1.0. The model c7v30b follows almost the same pattern, but the model c7v30 does not amplify the magnetic field. The only difference between them is that the DM profile in c7v30 is modelled by the “modified isothermal sphere” and c7v30b by phenomenological Burkert’s profile. The magnetic field in the models c81v30 and c81v30b is either very weak or not at all amplified.

The model c58v40 (Fig. 4.12 e) amplify the magnetic field energy to a value of  $10^{-4}$  and the  $B_\phi$  to  $10^{-2}$ . In the azimuthal flux evolution (Fig. 4.12 f) a one reversal event is present at  $t = 0.9$  Gyr. In the case of bigger speed of sound the  $E_B$  growth is faster than for  $c_s = 5.8$  km s $^{-1}$  and for model c7v40 reaches 1.0 and for c81v40 below 0.1. However the  $B_\phi$  evolution in both cases are very similar and the final value is about 1.0.

In the case of models with  $v_{\text{rot}} = 50$  km s $^{-1}$  the final  $E_B$  value is about  $10^{-3}$  and  $B_\phi$  about 0.1 for all investigated speeds of sound (Fig. 4.13 a, b). The sawtooth pattern in the  $E_B$  evolution is also apparent. The amplitude of the peaks of  $E_B$  evolution is much stronger for models with higher rotation speeds, i.e. 60 and 70 km s $^{-1}$  (Fig. 4.13 c, d, e and f), especially for models with  $c_s = 5.8$  km s $^{-1}$ , which can lead to unstable system behaviour, therefore the simulation can not be carried to 6 Gyr. In other cases the evolution is more stable and the  $E_B$  final value is about 1.0 for c7v60, 0.05 for c81v60,  $10^3$  for c7v70 and  $10^2$  for c81v70. The azimuthal flux seems to be not so much depended on the speed of sound in the ISM and for models which rotate about  $v_{\text{rot}} = 60$  km s $^{-1}$  can reach a value of 3, and for  $v_{\text{rot}} = 70$  km s $^{-1}$  up to 100.0.

In the Table 4.3 we can see that the growth rate of magnetic energy and azimuthal flux are comparable and do not show strong deviations with respect to different speeds of sound in the ISM. Only the model c81v30b seems to not amplifying the magnetic field at all and only it sustains the amount that was injected by the magnetized supernovae explosions. The  $e$ -folding times for magnetic energy is between 0.78 Gyr found in c58v40 and 0.19 Gyr found in c7v70. In the case of the magnetic azimuthal fluxes the growth rate is between 0.51 Gyr found in c81v70 and 1.21 Gyr in c58v40.

#### 4.2.4 Polarization maps

The result of each simulation is the 3D cubes of magnetic field and the CR energy density. Using the CR component as the proxy for the distribution of the relativistic electrons one can create a synthetic maps of total power and polarised synchrotron radiation (for details see Otmianowska-Mazur et al. 2009, Sec. 3). In the Figures 4.14 and 4.15 I show the polarization for models v40 and v20, respectively. The maps show the synthetic distribution of the polarised intensity at  $\lambda 6.2$  cm and the polarization angles, both superimposed

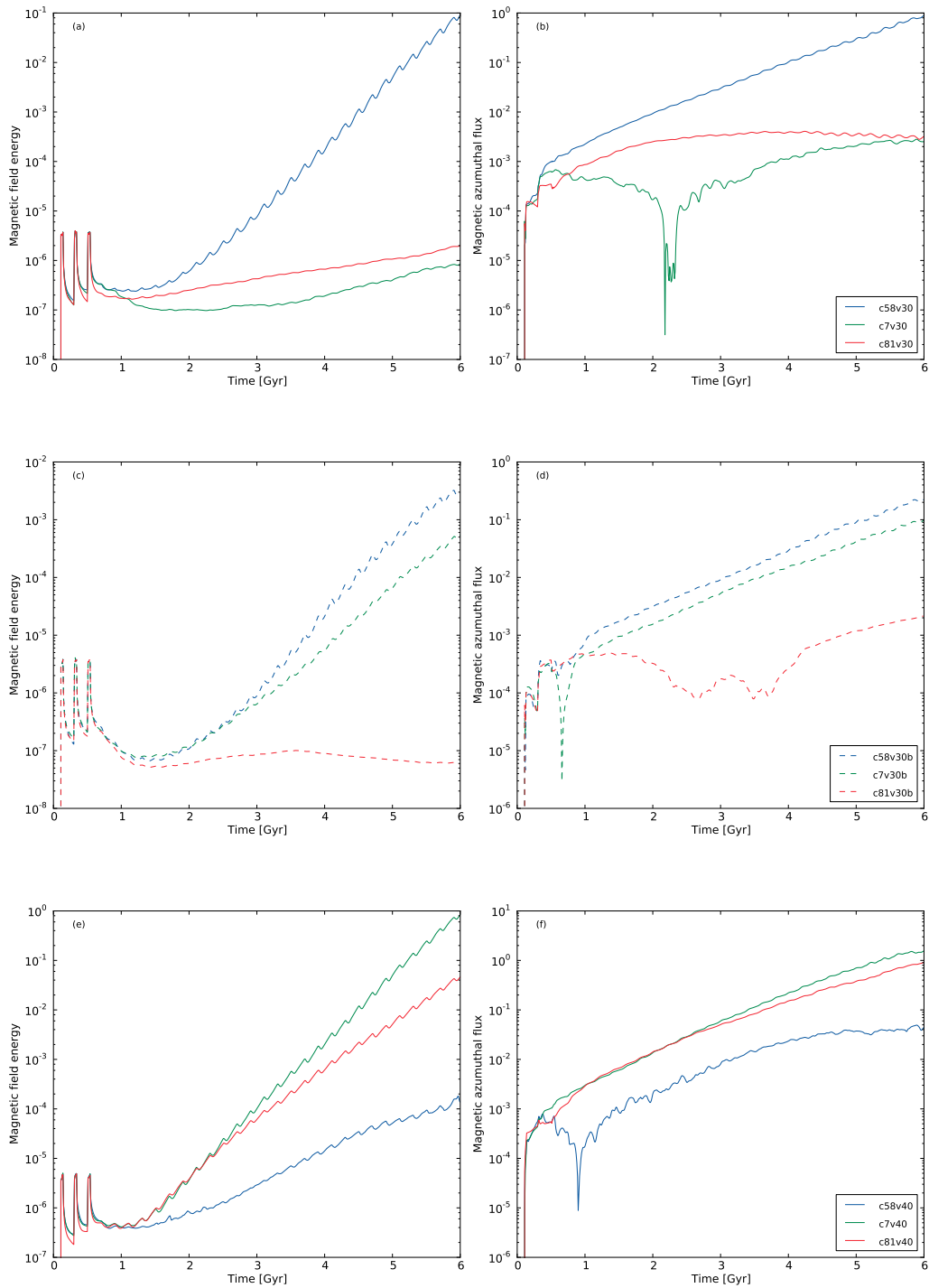


Figure 4.12: The evolution of the magnetic field for models with different rotation speed and speed of sound. The left panels show the total magnetic field energy evolution and the right ones the azimuthal magnetic flux evolution. The values are expressed in code units. To use the logarithmic scale for the azimuthal flux plot the absolute value is plotted, so if the flux starts to rapidly drop to very low values and then rapidly to grow this is a signature of sign turnover.

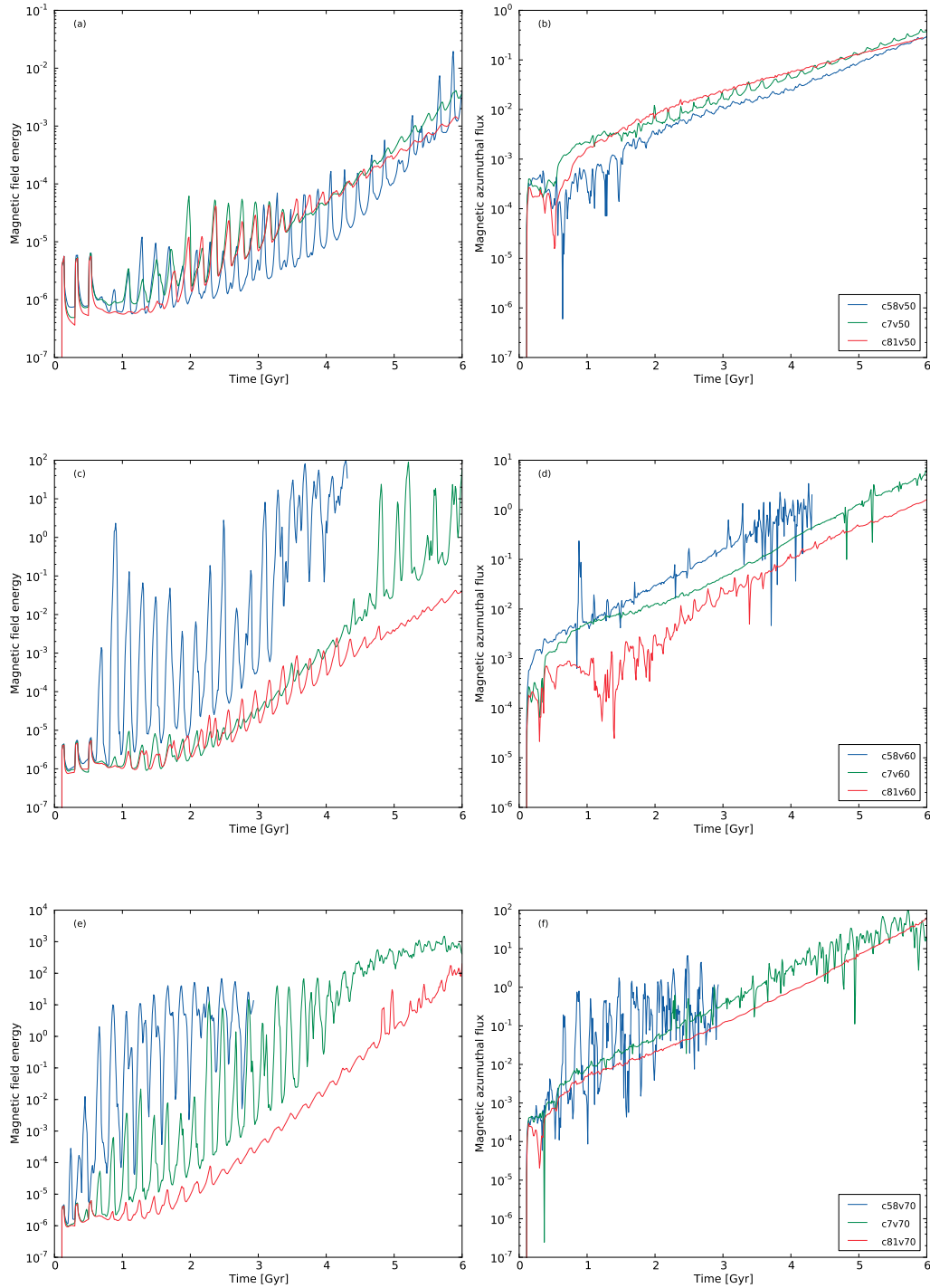


Figure 4.13: The evolution of the magnetic field for models with different rotation speed and speed of sound. The left panels show the total magnetic field energy evolution and the right ones the azimuthal magnetic flux evolution. The values are expressed in code units. To use the logarithmic scale for the azimuthal flux plot the absolute value is plotted, so if the flux starts to rapidly drop to very low values and then rapidly to grow this is a signature of sign turnover.

RESULTS FOR MODELS WITH DIFFERENT SPEEDS OF SOUND			
Model	$t_{B^2}^e$ [Gyr]	$t_{\phi}^e$ [Gyr]	$\max(B_{\phi})$ [ $\mu\text{G}$ ]
c58v30	0.39	0.83	0.40
c7v30	2.14	2.24	$0.49 \times 10^{-3}$
c81v30	2.05	3.82	$1.25 \times 10^{-3}$
c58v30b	0.41	0.92	$7.86 \times 10^{-2}$
c7v30b	0.47	0.96	$2.14 \times 10^{-2}$
c81v30b	36.23	2.92	$5.42 \times 10^{-5}$
c58v40	0.78	1.21	$1.02 \times 10^{-2}$
c7v40	0.33	0.81	0.76
c81v40	0.41	0.92	0.17
c58v50	0.53	0.89	0.64
c7v50	0.57	0.99	$3.46 \times 10^{-2}$
c81v50	0.58	1.05	$1.97 \times 10^{-2}$
c58v60 <sup>†</sup>	0.18	0.55	13.98
c7v60	0.27	0.68	28.94
c81v60	0.42	0.65	14.00
c58v70 <sup>†</sup>	0.21	0.26	9.60
c7v70	0.19	0.57	25.17
c81v70	0.25	0.51	24.31

Table 4.3: The subsequent columns show: the model name, the  $e$ -folding time of the magnetic field energy ( $t_{B^2}^e$ ), the  $e$ -folding time of the magnetic azimuthal flux ( $t_{\phi}^e$ ) and the maximal value of the  $B_{\phi}$  in the galaxy disk. Please note that the models marked with <sup>†</sup> are not simulated up to  $t = 6.0$  Gyr. They are only presented for the comparison, but are not taken into account in the results description.

onto the column gas density. The selected time steps correspond to those showed in previous plots in the Figures 4.7, 4.8 and 4.9.

At  $t = 0.15$  and  $0.35$  Gyr the system in the v40 model is just after the first and second burst of the magnetised SNe explosions. The column gas density in the face-on view is highly disturbed by the driven turbulence and the polarised intensity is very patchy. The polarisation angles already have strong toroidal component, but some deviations, especially it the first snapshot, can be seen. The polarization maps of the next time steps show that the patches of the polarised intensity merge and form smooth and concentric circles with the maximum located in the galaxy centre. The edge-on view of the galaxy show that most of the polarised emission also comes from the centre. However the initially inclined polarisation angles with respect to the disk mid plane at  $t = 0.75$  Gyr starts to be more parallel.

At the final snapshot the column gas density move slightly to the outer part of the galaxy. The polarised intensity in the disk region is very flat and have very strong gradient at the edge of the disk. Additionally some ‘‘spiral’’ structures of the polarised intensity appear in the disk edge, but with no counterpart in the gas density. This can be caused by

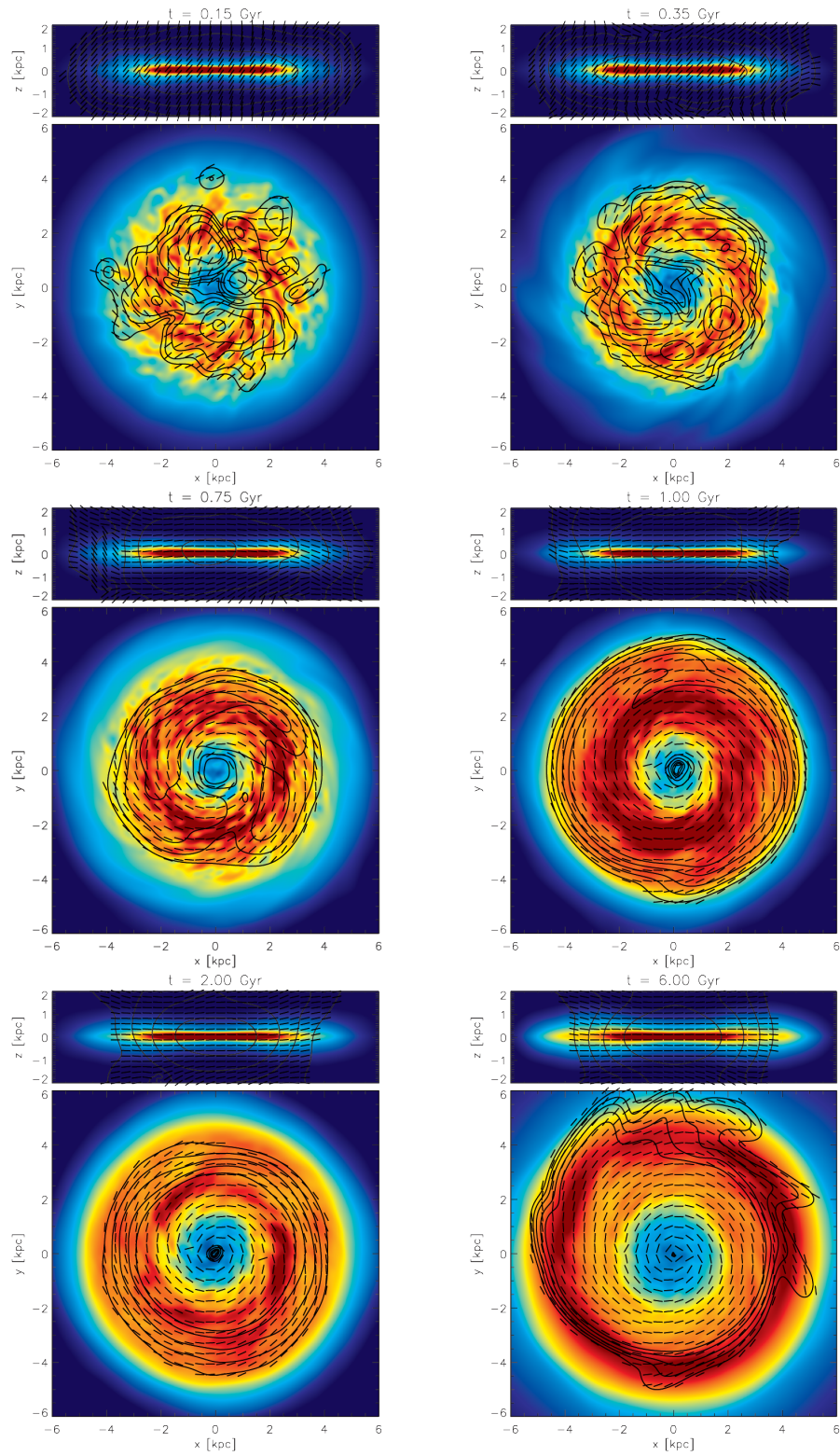


Figure 4.14: Polarization maps at  $\lambda 6.2$  cm for selected timesteps for the model v40. For each plot the top panel shows the edge-on and the bottom the face-on view of the galaxy. The contours of the polarization intensity and the dashes of the polarisation angles are superimposed onto the column density plot.

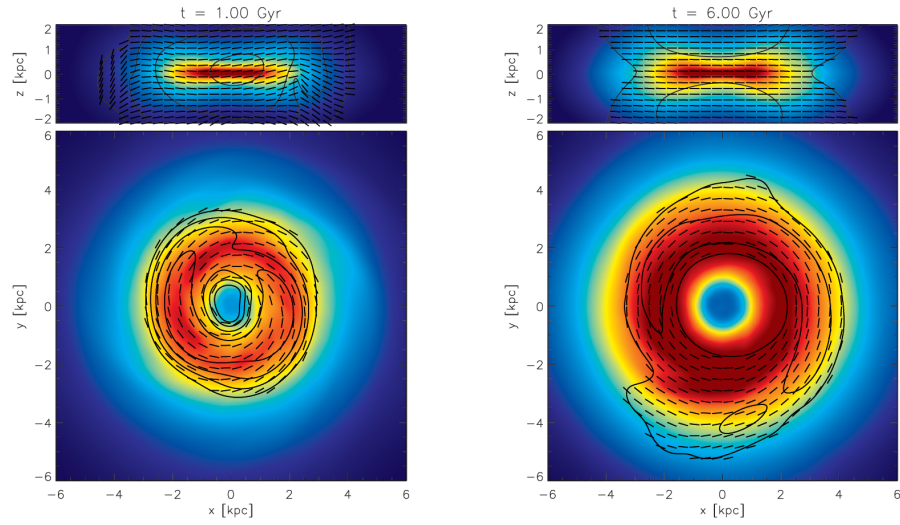


Figure 4.15: Polarization maps at  $\lambda 6.2$  cm for selected timesteps for the model v20. For each plot the top panel shows the edge-on and the bottom the face-on view of the galaxy. The contours of the polarization intensity and the dashes of the polarisation angles are superimposed onto the column density plot.

the fact that the disk radius is much bigger than in the previous time steps and the disk edge is very close to the boundaries, therefore the boundary conditions may have much more influence on the system. The edge-on view show that the polarisation angles are perfectly parallel to the disk plane.

The above picture of the evolution of the galaxy seen by the synthetic radio maps is common for all other models which have significant growth of the magnetic fields, i.e. where the dynamo operates. For the rest of the models, for example v20 this picture have some differences. The initially stage is very similar to this described in previous paragraphs. After the first 1 Gyr (Figure 4.15, left panel) the distribution of the polarised intensity is very similar to this found for the v40 model, but the maximum is not located in the galaxy centre. A hole in the polarization distribution can be easily see in the final snapshot (right panel). The polarised intensity is distributed in a form of a ring around the centre. Very interesting shape appear in the edge-on view. The polarisation angles are perfectly parallel to the disk plane, but the maximum is not located in the disk centre, instead it is just above and below the disk. This picture of the polarised intensity distribution seems to be created by a following structure: two blobs with maxima above and below the disk, but in the disk they are connected.

### 4.3 Pressure equilibrium

In the system of dwarf galaxy model there are 3 components which contribute to the total pressure, i.e. thermal gas, cosmic rays and magnetic fields. To show the pressure balance between each component following ratios are calculated:

$$\alpha \equiv p_{\text{mag}}/p_{\text{gas}} \quad \text{and} \quad \beta \equiv p_{\text{CR}}/p_{\text{gas}}. \quad (4.2)$$

The evolution of  $\alpha$  and  $\beta$  for the reference models are shown in Figure 4.16. The bare solid and dashed lines show the  $\beta$  ratio. In the initial state of the system  $\beta$  equals 1 and is determined by the initial conditions. The pressure of the cosmic rays during the evolution is slowly increasing because of the SNe injection. The final value of  $\beta$  is about 10.0 for each of the investigated models.

The evolution of  $\alpha$  ratio, which is crucial for the dynamo action is shown in the Figure by dots and triangles. The initial value, at  $t = 0$  is set to 0, and after the simulation starts the magnetic field is seeded by the magnetized SNe explosions. The pressure ratio  $\alpha$  after first injections is in a range of  $10^{-12}$  and  $10^{-10}$  and depends on the galaxy size. The magnetic field is supplied by the magnetized SNe explosions till about 0.6 Gyr, which manifests in the plots by a slight increase (the very first 3 points). After that time the injection of magnetized SNe is stopped and the SNe contributes only to the cosmic rays. The models with the slowest rotation speeds maintain the ratio in the level of  $10^{-12}$ . As the rotation speed increase up to  $60 \text{ km s}^{-1}$  the final value of the  $\alpha$  is bigger and spans from  $10^{-9}$  to  $10^{-3}$ . The growth of the  $\alpha$  in all cases is exponential and only in the v60 model some strong variation can be seen. In the case of the fastest rotation models the evolution follows the same pattern but after  $t = 5 \text{ Gyr}$  the growth rate starts to be much smaller as it is closing to a equilibrium, i.e.  $\alpha = 1$ .

To compare above results with models which have different ISM temperatures the similar evolution of pressure ratio is plotted for those which have  $c_s = 5.8$  and  $8.1 \text{ km s}^{-1}$  (Figure 4.17). In this case non of the models have reached the pressure equilibrium between magnetic field and thermal gas. The highest value is found for c81v70 model and the pressure ratio is about  $10^{-2}$ . The models c58v60 and c58v70 show very rapid increase of the magnetic fields and reach the value of the ratio of the order of  $10^{-3}$ . The other models show the pressure ratio between  $10^{-9}$  and  $10^{-6}$ . The exception is the model c81v30 which maintains the magnetic field on the same level as initially injected. The pressure ratio between the cosmic rays and thermal gas is slowly growing from 1 to about 10 for each of the model. This ratio evolution is very similar to those find in the models with  $c_s = 7.0 \text{ km s}^{-1}$ .

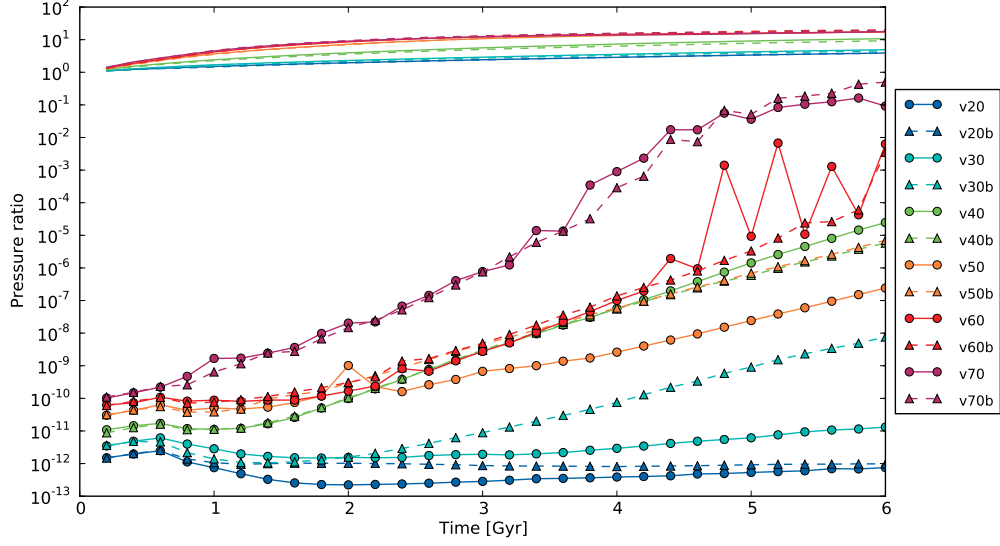


Figure 4.16: Evolution of the pressure ratios in the galaxy for the reference models. The pressure ratios  $p_{\text{CR}}/p_{\text{gas}}$  and  $p_{\text{mag}}/p_{\text{gas}}$  are marked by lines and lines with dots and triangles, respectively. Solid line and solid line with dots show the models with DM profile described by “modified isothermal sphere”, and dashed line and dashed line with triangles mark the models with Burkert’s profile.

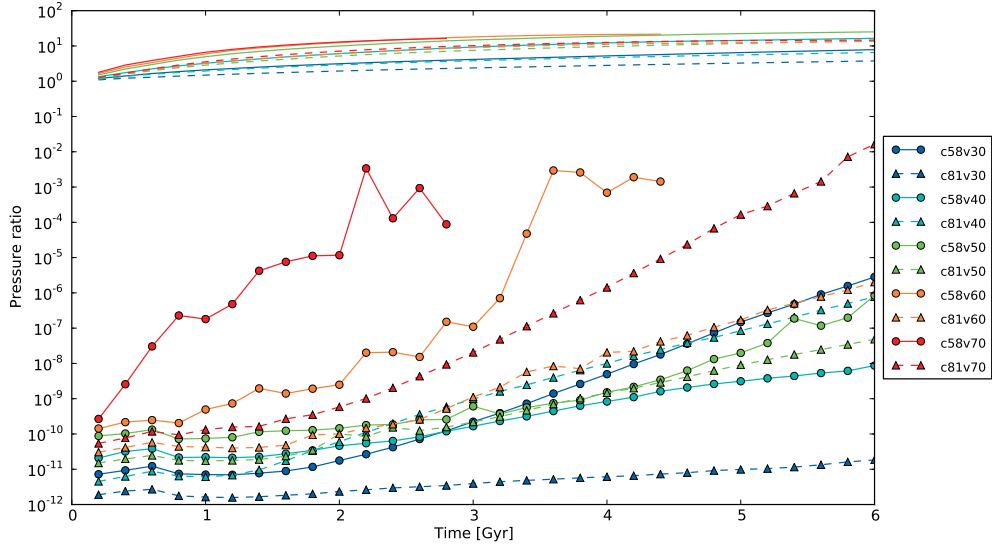


Figure 4.17: Evolution of the pressure ratios in the galaxy for the models with  $\hat{c}_s = 5.8$  and  $8.1 \text{ km s}^{-1}$ . The pressure ratios  $p_{\text{CR}}/p_{\text{gas}}$  and  $p_{\text{mag}}/p_{\text{gas}}$  are marked by lines and lines with points, respectively. Solid line and solid line with dots show the models with  $c_s = 5.8 \text{ km s}^{-1}$ , and dashed line and dashed line with triangles mark the models with  $c_s = 8.1 \text{ km s}^{-1}$ .

## Discussion

The results of the simulations of the cosmic ray driven dynamo in the dwarf galaxies show that magnetic field can be amplified by this process to a values which are found in observations of the magnetic field in galaxies. This amplification is driven by the SNe explosions and the in the beginning of the simulation the dynamo is seeded by the small magnetic dipoles associated with the very first SNe. Depending on the mass of the galaxy the final magnetic field have different values and some of them are close to this found in real objects. The dynamo is also responsible to the final structure of the magnetic field. The results of the simulation can be compared to the previous works on the cosmic ray driven dynamo, also in dwarf galaxies and to the observations of particular galaxies.

### 5.1 Cosmic ray driven dynamo in galaxies

#### 5.1.1 Growth rate of the magnetic field

A characteristic number of a magnetic dynamo process is the  $e$ -folding time (4.1) which measures the growth rate of the azimuthal magnetic flux in the system. Its value depends mostly on the rotation speed in the galaxy. The fast rotating objects ( $v_{\text{rot}} \geq 40 \text{ km s}^{-1}$ ) show very consistent results, which do not depends on other parameters like: DM profile, supernova rate or gas temperature. The  $e$ -folding times are in a range of 1.75 Gyr for slower rotators and 440 Myr for the fastest ones. This results is consistent with those found in other works about CR driven dynamo. The simulations of a more massive galaxy in the shearing box approximation (Hanasz et al. 2009a) show that the growth rate can be as fast as 150 or 190 Myr and depends on the SN frequency. In the case of global simulations of a spiral galaxies the growth is about 270 Myr (Hanasz et al. 2009b). Recently (Kulpa-Dybeł et al. 2011) found that for barred galaxies the  $e$ -folding time is about 300 Myr. Note, the more massive objects like spirals and barred galaxies rotates about

5 times faster than the dwarf galaxies models from this thesis. Above results show that the fast rotating dwarfs ( $v_{\text{rot}} \geq 60 \text{ km s}^{-1}$ ) with their  $t_{\phi}^e \simeq 400 \text{ Myr}$  and the spiral and barred galaxies have very similar growth rates of the magnetic field caused by the operation of the cosmic ray driven dynamo. If the rotation speed decreases below  $60 \text{ km s}^{-1}$  the  $e$ -folding times are much longer. This value of  $v_{\text{rot}}$  seems to be a threshold of the fast magnetic amplification. In the range of rotation speed between  $40$  and  $60 \text{ km s}^{-1}$  the amplification is still positive but the growth rates are a little bit longer, about  $810$ – $1210 \text{ Myr}$ . This result is compatible with those found in studies of cosmic ray driven dynamo in dwarf galaxies in the shearing box approximation (Siejkowski et al. 2010). The  $e$ -folding times for a object which rotates as fast as  $40 \text{ km s}^{-1}$  was  $840 \text{ Myr}$  and for  $60 \text{ km s}^{-1}$  is  $675 \text{ Myr}$ .

In the case of less massive objects which rotates as fast as  $30 \text{ km s}^{-1}$  the amplification depends also on other parameters. In general, the models with the DM distribution described by the Burkert’s profile amplifies the magnetic field faster than those modelled by “modified isothermal sphere” profile. In the most extreme case the  $e$ -folding time can be 5 times lower in the model with Burkert’s profile (v30b). Another parameter which influence the growth rate for slow rotating objects is the gas temperature. If the gas is too hot ( $T = 8000 \text{ K}$ ) the dynamo amplifies the magnetic field extremely slowly or not at all. However if the temperature is about  $4000 \text{ K}$  the amplification is quite fast,  $t_{\phi}^e = 830 \text{ Myr}$ . Supernova frequency modulation also influence the growth rate of the magnetic field. The longer the SNe are active within each period of modulation the slower the growth rate. This applies mostly to the models with Burkert’s DM profile, because the models with DM described by the “modified isothermal sphere” show very weak amplification.

The slowest rotating models from the sample described in this thesis do not amplify the magnetic field at all. The initially injected magnetic field via the magnetized SNe explosion is only sustained through the whole simulation time.

From above results a following picture of the magnetic field amplification with respect to the rotational velocity emerge: if  $v_{\text{rot}} \simeq 20 \text{ km s}^{-1}$  the cosmic ray driven dynamo do not amplify the magnetic field; for  $v_{\text{rot}} \simeq 30$  the  $e$ -folding times are in a range  $800$ – $1700 \text{ Myr}$  and depends on the gas temperature and the SNe explosions modulation; with the increase of the rotational velocity ( $\geq 40 \text{ km s}^{-1}$ ) the growth rate is between  $800$ – $1200 \text{ Myr}$ ; since the  $v_{\text{rot}} \geq 60 \text{ km s}^{-1}$  the  $e$ -folding time is about  $400 \text{ Myr}$ . For much more massive galaxies, which rotates as fast as  $200 \text{ km s}^{-1}$ , the growth rate only slightly increases up to  $300$ – $270 \text{ Myr}$ .

The azimuthal flux in the galaxy disk is attributed to the regular component of the magnetic field. In contrast to the turbulent magnetic field the regular component is responsible for the polarized radio emission. Additionally the creation of the regular magnetic field determines whether the dynamo is a large or small scale (Brandenburg & Subramanian 2005). The magnetic field energy represent the “sum” of the regular and

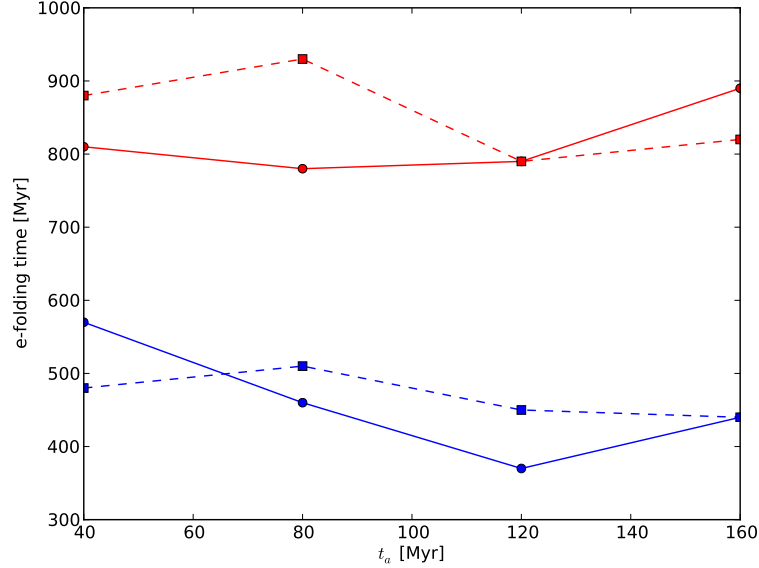


Figure 5.1: Dependence of the  $e$ -folding times of azimuthal flux evolution on the different times of supernovae frequency evolution. Note that the period of SN modulation,  $T_{\text{SN}}$  in all cases is constant and equals 200 Myr. Red and blue points mark the models with  $v_{\text{rot}} = 40 \text{ km s}^{-1}$  and  $70 \text{ km s}^{-1}$ , respectively. The dots regard to models with MIS DM profile and the squares with Burkert's profile.

turbulent magnetic field component and its growth rate is 2-3 times faster than the azimuthal flux. This is because the initially randomly oriented magnetic field is being ordered by the rotation, but its strength is not being amplified. For the other cases the newly created flux due to the Parker instability is regularised and contributes to the total azimuthal flux. The values of  $t_e^\phi$  are 2 or 3 times longer than growth rate of the magnetic energy for the same model. The process of regularization the magnetic field takes much more time than just the amplification.

### 5.1.2 Modulation of the supernova rate

The results presented in the Sec. 4.2.1 regards to simulations with different modulation times of the supernova rate. Shearing box simulations of the cosmic ray driven dynamo show that the efficiency of the magnetic field growth is much better when the supernovae explosions are periodically modulated (Hanasz et al. 2009a). Also in the case of the local simulations of dwarf galaxy by Siejkowski et al. (2010) reported about the dependence of the magnetic field on the time of halted SN activity. They found that the shorter the time of quiescent state the faster the growth of the regular component of the magnetic field. The results of the global galactic-disk simulation show that this dependence seems to be weak. The  $e$ -folding times of the azimuthal flux amplification are comparable with

respect to different durations of the SN activity within one period (Figure 5.1). For the fast rotating models,  $v_{\text{rot}} \geq 40 \text{ km s}^{-1}$ , the growth rate is about 900 Myr and increases up to 500 Myr for the fastest rotating models. Also in the case of models with  $v_{\text{rot}} = 30 \text{ km s}^{-1}$  the  $e$ -folding times are about 1–2 Gyr, but in this group also are present models which amplifies the magnetic field very slowly or not at all.

### 5.1.3 Dark matter profile and the magnetic fields

The dwarf galaxy model presented in this thesis consists of the static gravitational potential. This potential is a sum of two components: stars and dark matter halo. Typically in such modelling also the third component is added, especially in spiral galaxies, which is generated by the central bulge, but dwarf galaxies seems to not have this feature (Governato et al. 2010). The stellar component is usually described by the this Kuzmin's disk (Eq. 3.9) and the DM halo by the “modified isothermal sphere” (Eq. 3.12). However Burkert (1995) have found a purely phenomenological DM profile, which slightly differ from the previous one (Figure 3.1). While the stellar component is responsible for the shape of the rotation curve in the most central part of the galaxy, the DM halo shape the curve in the outer parts. The rotation curves generated using this two DM halo models are shown in Figure 3.5.

One of the crucial parameter of the dynamo action is the shearing rate and can be defined as follows:

$$q \equiv -\frac{d \ln \Omega}{d \ln R} = -\frac{d(v/R)}{dR} \frac{R^2}{v}, \quad (5.1)$$

where  $\Omega$  is the angular velocity,  $v$  is the rotation velocity and  $R$  is the radius. Using this formula one can find the shearing rate from the rotation curves generated in the models. The shearing rate is about 0.40 at 3 kpc and 0.25 at the 6 kpc radius for the models with DM halo modelled by Burkert's profile. The models with “modified isothermal sphere” (MIS) profile within the radius range has shearing rate about 1.0 (flat rotation curve). The results show that only the slow rotating objects ( $v_{\text{rot}} = 30 \text{ km s}^{-1}$ ) with Burkert's profile generate much stronger magnetic fields than those modelled, which have DM profile describe by MIS. In the other cases the results are comparable. This have been also reported by Siejkowski et al. (2010). They look in the local simulations of dwarf galaxy for dependence of the final magnetic field on different values of  $q$ . The conclusion was that the dynamo does not depend on the shearing rate if only it does not equal zero. In this case the dynamo do not amplify the magnetic field at all. The results of global simulation support this conclusion with only a possible exception for slow rotating objects.

#### 5.1.4 Equilibrium in the ISM

The issue of the pressure balance in the system between thermal gas, cosmic rays and magnetic fields has been investigated by Hanasz et al. (2009a) in the local simulations of cosmic ray driven dynamo in massive galaxies. They found that the evolution of  $p_{\text{cr}}/p_{\text{gas}}$  depends on the CR diffusion coefficients and if the latter are higher the ratio after the simulation is lower. In this thesis the adopted value of the CR diffusion is 10% of the realistic values because of the time step limitations. The explicit algorithm of the CR diffusion causes that the time step is significantly short when the realistic values of diffusion coefficients are used. The simulation results show that in the case of global dwarf galaxy simulation the CR pressure is about 10 times higher than thermal gas. Similar result for the same values of diffusion coefficient has been found by Hanasz et al. (2009a). Such excess of CRs pressure in the numerical simulation has been also reported by Snodin et al. (2006). It also seems that the ratio of CR to other forms of pressure in the ISM is not yet well constrained by the observations (Strong et al. 2007; Stepanov et al. 2012).

#### 5.1.5 Magnetic field structure

The large scale dynamo process amplifies the magnetic field and simultaneously orders it. As the result of the dynamo the magnetic field should have a coherent direction within a galaxy disk. To verify whether the cosmic ray driven dynamo can create such magnetic field in the disk a plots of  $B_\phi$  evolution and the orientation of the magnetic field have been made (Figure 4.7, 4.8, 4.9). In the case of a model where the dynamo works, e.g. v40, the initially random magnetic field is being ordered, and after 2 Gyr the direction of the magnetic field is coherent within the disk. Comparing the maps of  $B_\phi$  (Figure 4.7) and  $B^2$  (Figure 4.8) one can see that the distribution of the azimuthal flux correlates with the magnetic energy. This suggest that the  $B_\phi$  component is dominant and contributes significantly to the total magnetic field. Within the first 1 Gyr the random magnetic field is transformed into spiral arms of azimuthal flux with oppositely directed signs. This is manifested in the plots by the alternately positioned red and blue spiral arms. Such an evolution of the  $B_\phi$  component is common in other global simulations of cosmic ray driven dynamo (Hanasz et al. 2009b; Kulpa-Dybeł et al. 2011).

In the evolution of the azimuthal magnetic flux sometimes occurs the turnovers of its direction. This effects has been found also in other studies of cosmic ray driven dynamo (e.g. Siejkowski et al. 2010). This can occurs mostly in the beginning of the simulation, where the magnetic field is not strong enough to resist against the turbulence driven by SNe explosions. At later stages of the evolution the global reverse of the azimuthal flux occurs only in models in which the dynamo action is very weak and slow.

The final orientation of the magnetic field in the disk plane (Figure 4.7, last panel) suggests that the magnetic field has axissymmetric configuration (ASS). This results is

the same for all models which manifests strong magnetic field amplification. Such configuration is also found by Hanasz et al. (2009b) and Kulpa-Dybeł et al. (2011) and also in observations of M 31 (Beck 1982) and IC 342 (Krause et al. 1989b). The dominance of the ASS configuration in the simulation is not surprising, because this configuration is the easiest one to be excited in the galaxy disk (Krause 2003).

The edge-on view of the azimuthal flux in the galaxy disk can tell about the vertical symmetry about the magnetic field. The orientation of the magnetic field above and below the disk is the same. This configuration corresponds with the quadrupolar vertical field (Figure 2.9) and has been also found in the studies of cosmic ray driven dynamo in spiral and barred galaxies. Theoretical investigations (Ruzmaikin et al. 1988), observational works (Heesen et al. 2009) and numerical simulations (Brandenburg et al. 1993) support the idea that the even symmetry of the vertical magnetic field configuration can be found in most of the disk galaxies.

In the edge-on view a very interesting structure appears. The disk is penetrated by a coherently oriented toroidal magnetic field, but from the galaxy disk arise “streams” of oppositely directed magnetic azimuthal flux. These “streams” spans from the disk up to the upper and lower boundary. Such a feature has been also found in simulations of dynamo in spiral galaxies by Hanasz et al. (2009b), however they found it only in the galaxy centre. In the case of dwarf galaxies these structure can be as wide as the disk itself.

The models in which the dynamo is not amplifying the magnetic field the structure of the magnetic field is totally different. In the first 1 Gyr the galaxy evolves similarly to the above-described picture, but then the toroidal component of the magnetic field is not amplified, as well as the total magnetic energy. The configuration of the field found in the disk plane after 6 Gyr has very weak toroidal magnetic field (Figure 4.9). In the edge-on view one can see a “butterfly structure” of the azimuthal magnetic flux. The flux above the disk is oppositely directed with respect to this found below the disk. This configuration have the odd symmetry (Figure 2.9), but in this case the magnetic fields are not amplified. Looking at the edge-on view one can understand why the toroidal magnetic field is very weak in the disk mid plane, i.e. the magnetic field reverse its direction.

## 5.2 Comparison between models and observations

The simulations of the cosmic ray driven dynamo in dwarf galaxies presented in this thesis aim to find possible relations between the strength of the magnetic field and the characteristics of the galaxy, like rotation, star formation rate and ISM temperature. Such investigation in the observational side has been recently done by Chyży et al. (2011). The observational sample however is very limited due to the lack of enough sensitivity of current radio telescopes and the study regards to objects from our Local Group with

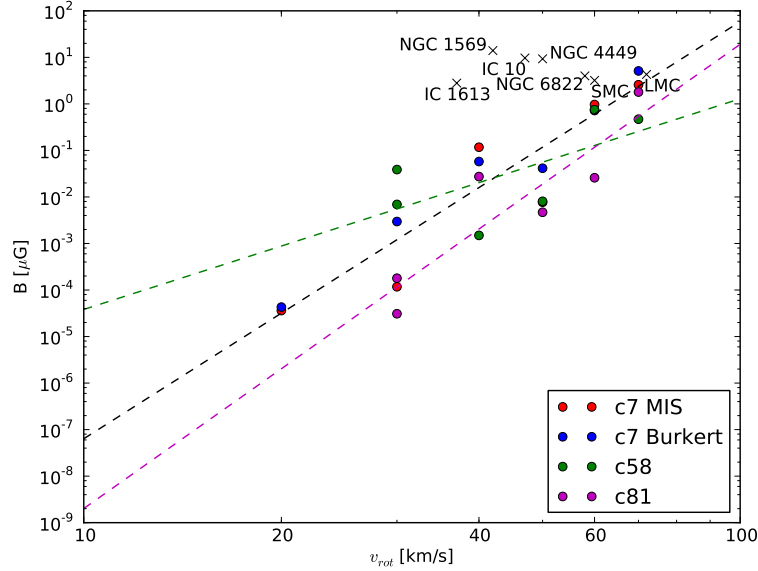


Figure 5.2: Relation between the  $v_{\text{rot}}$  and total magnetic field in the model after 6 Gyr. The models with DM profile described by the “modified isothermal sphere” (MIS) and the Burkert’s profile are mark by red and blue dots, respectively. Additionally the results for models with speed of sound set to  $c_s = 5.8$  (green dots) and  $8.1 \text{ km s}^{-1}$  (pink dots) are plotted. The fit to the data is marked by the black, green and pink dashed lines for models with  $c_s = 7.0$ ,  $5.8$  and  $8.1 \text{ km s}^{-1}$ , respectively. The crosses show the data of galaxies: IC 10, IC 1613, NGC 1569, NGC 4449, NGC 6822, SMC and LMC, taken from Chyży et al. (2011).

some few objects from more distant Universe.

The results of the simulations of the models with different rotation speeds show clearly that the final value of the amplified magnetic field depends on the rotational velocity. This regards to the magnetic energy evolution and also its toroidal component. The results are summarised in Figure 5.2, where for each reference model the mean magnetic field is plotted against the rotational velocity. The relation show that magnetic is power law dependent on the rotational velocity. What is more also the shape of the rotation curve determined by using the different DM profiles influence this relation, especially for slowly rotating objects.

The above relation have a correlation coefficient  $r = 0.94$  and can be quantified by the power law fit,  $B \propto v_{\text{rot}}^{8.96 \pm 0.99}$ . For the fit the data are used from both types of models regarding the different DM profiles. To compare this result the real galaxies are also plotted in the figure, for which the total magnetic field is known. Only two galaxies follows closely this relation, namely SMC and LMC. The others are above the fitted curve. In the case of IC 10, NGC 1569 and NGC 4449, they are currently undergoing strong starburst and therefore might be unsettled. Especially the NGC 4449 is more massive than LMC,

but its rotation curve is highly disturbed (Figure 2.8, right panel) and the observational  $v_{\text{rot}}$  can be underestimated, so probably it might shift a little to the right. The NGC 6822 and IC 1613 however are in their quiescence state, and quite close to the modelled trend. Additionally the data from observations can be influenced by the selection effect. There are only 7 objects which have strong enough magnetic fields to be observed by current radio telescopes. For the other 9 objects from the Chyży et al. (2011) sample only the upper limits are found. The upper limits are about few  $\mu\text{G}$  but the  $v_{\text{rot}}$  spans from 13 up to 37  $\text{km s}^{-1}$ , so if we have enough sensitivity to measure the magnetic field in these objects they can be plotted in the figure and probably might follow the found trend.

To compare the results of the simulations of the models with different speed of sounds also the final results for models with  $c_s = 5.8$  and  $8.1 \text{ km s}^{-1}$  are plotted. The fits are following:

- for  $c_s = 5.8 \text{ km s}^{-1}$ ,  $B \propto v_{\text{rot}}^{4.53 \pm 2.66}$ ,  $r = 0.65$ ;
- for  $c_s = 8.1 \text{ km s}^{-1}$ ,  $B \propto v_{\text{rot}}^{9.97 \pm 2.38}$ ,  $r = 0.90$ .

The result for  $8.1 \text{ km s}^{-1}$  is consistent with this found for  $c_s = 7.0 \text{ km s}^{-1}$ . The indices are very close and match within its uncertainties. However for the models with hotter gas the final value of magnetic field is about 1.5-2 order of magnitude lower. In the case of  $c_s = 5.8 \text{ km s}^{-1}$  the result is very uncertain, because the points for  $v_{\text{rot}} = 60$  and  $70 \text{ km s}^{-1}$  are calculated in models, which were not simulated until 6 Gyr (see Sec. 4.2.3). This is also reflected by the low correlation coefficient. However from this analysis one can see that, especially for slow rotating models ( $v_{\text{rot}} \leq 40 \text{ km s}^{-1}$ ) the galaxies with cooler gas can amplify the magnetic field to much greater values.

### 5.2.1 NGC 1569

The observations of NGC 1569 by Kepley et al. (2010) have shown that it has strong magnetic field. The total magnetic field is about 10–15  $\mu\text{G}$ , with a maximum of 38  $\mu\text{G}$  in the central part. The regular component is between 3–9  $\mu\text{G}$ . Using the models from the sample presented in this thesis the most corresponding model is the v40 or v40b, according to the rotational velocity. These two models have very similar final results, so both can be taken into account. The final total magnetic field in the simulation is about 0.1  $\mu\text{G}$  and the regular component 0.06  $\mu\text{G}$ . The maximum value of the azimuthal flux is as high as 1  $\mu\text{G}$ . Apparently the magnetic field in v40 and v40b models are too weak to explain the observed values by the cosmic ray driven dynamo. The models which have faster rotation of about 60  $\text{km s}^{-1}$  can generate such magnetic fields. In these cases the total magnetic field is about 1  $\mu\text{G}$  and the maximum value of  $B_\phi$  is about 28  $\text{km s}^{-1}$ .

The models v40, v40b and v60 and v60b are set to explode SNe with frequency  $f_{\text{SN}} = 3000 \text{ kpc}^{-2} \text{ Gyr}^{-1}$  and is approximately equivalent to  $\Sigma\text{SFR} = 4.7 \times 10^{-4} M_\odot \text{ yr}^{-1} \text{ kpc}^{-2}$ .

The observed current  $\Sigma\text{SFR}$  in NGC 1569 is about  $0.1 M_{\odot} \text{ yr}^{-1} \text{ kpc}^{-2}$ . The difference is 2.5 order of magnitude, but the galaxy is currently undergoing very strong starburst, and therefore the observed value is enormously high. Such  $\Sigma\text{SFR}$  can not last for very long time about few Gyr, because of limited reservoir of gas, which can be converted into stars and therefore this event can be treated as an exception. The assumed value in simulation compared to the other objects is in the mid range of other galaxies (Figure A.1).

Kepley et al. (2010) reported that the magnetic field in NGC 1569 is mostly perpendicular to the plane of sky. This is what is found in the synthetic polarization maps (Figure 4.14). The edge-on view show that the magnetic field is almost perfectly parallel to disk plane. The configuration of the magnetic field in the observations have strong radial component, whereas the synthetic polarization maps show almost only toroidal magnetic field. In the observations only in the eastern part of the galaxy a spiral arm is apparent, but it is probably related with an inflow/outflow event. The difference in the magnetic field configuration in the disk plane can be cause by the strong starburst event, which can drive significant amount of turbulence in to the system and therefore influence the configuration. This galaxy also interacts intensively with the surrounding environment. Lots of gas is expelled from the galaxy, but there is also an infalling matter (Stil & Israel 2002; Recchi et al. 2006). Such phenomena are known to disturb the galaxy structure as well as the magnetic field configuration.

### 5.2.2 NGC 4449

Chyży et al. (2000) reported about the magnetic fields in NGC 4449. This galaxy have the total magnetic field equals to  $9.3 \pm 2.0 \mu\text{G}$  with a regular component between 6 and  $8 \mu\text{G}$ . Its rotation speed is very difficult to estimate, because this galaxy is rapidly forming stars. The rotation curve even have some counter rotating parts (Figure 2.8). Defining the  $\nu_{\text{rot}}$  as the maximum of rotational velocity and 2 times the velocity dispersion gives a result of  $50 \text{ km s}^{-1}$  (Woo et al. 2008; Hunter et al. 1999). However if one compare the mass of the galaxy with LMC, which rotates as fast as  $72 \text{ km s}^{-1}$ , one can find the NGC 4449 is 3.5 times more massive. This suggest that the observed  $\nu_{\text{rot}}$  is underestimated and therefore a one of the model from v70 class can be attributed to describe this galaxy. The v70 and v70b are the only two models which reach almost the equipartition level. The final magnetic field is about  $10 \mu\text{G}$  with a regular component about  $8 \mu\text{G}$ . The maximal azimuthal flux is between 25 and  $37 \mu\text{G}$ .

The observed structure of the magnetic field show very strong toroidal component of regular field. The maximum of the total power emission is located at the central part of the galaxy. Such configuration is also found on the synthetic polarization maps (Figure 4.14). The dominant component of the magnetic field is the toroidal one, and the maximum is also found in the galaxy centre. The rotation measure observations imply the magnetic field to be unidirectional (Chyży et al. 2000) rather than stretched and com-

press random magnetic field. This is also the case in the simulation results, see Figure 4.8. The initially random magnetic field is being transformed into ordered one, but the neighbouring regions have oppositely directed magnetic vectors. Due to the dynamo action the configuration is regularised and the vectors are oriented in the same direction. The opposite evolution is found in the object where the magnetic field is not being amplified (Figure 4.9). In the final snapshot the magnetic field has strong azimuthal component, but still the vectors are oppositely oriented in neighbouring regions.

### 5.2.3 IC 10 and NGC 6822

These two galaxies are the members of the Local Group. Their rotation speed is about  $47 \text{ km s}^{-1}$  in IC 10 (Wilcots & Miller 1998) and is rapidly forming stars. The NGC 6822 is in its quiescent state and rotates about  $60 \text{ km s}^{-1}$  (Weldrake et al. 2003). The observations reveal that the regular magnetic field in both galaxies is about  $2\text{-}3 \mu\text{G}$  (Chyży et al. 2003). The total magnetic field in IC 10 and NGC 6822 is about  $10 \mu\text{G}$  and  $4 \mu\text{G}$ , respectively. These two examples show that with high star formation rate the total magnetic field is stronger than in the case of low SFR. However the ratio of regular magnetic field to total magnetic field is higher for objects in quiescent state. The simulations presented in this thesis show that the magnetic field is dominated by the regular component. Note that the applied  $\Sigma\text{SFR}$  is very low when compared to the numbers found in those two galaxies. NGC 6822 can be compared to the v60 or v60b models. The magnetic field found in these models is about  $1 \mu\text{G}$ , but the maximum of the azimuthal flux is between  $25\text{-}29 \mu\text{G}$ . These models seem to explain the observed magnetic fields in this galaxy by operation of the cosmic ray driven dynamo. In the case of IC 10 the corresponding models which rotate as fast as  $50 \text{ km s}^{-1}$  do not reproduce the observed magnetic fields. The final magnetic fields are two orders of magnitude lower than the observations show. However the much higher star formation rate in the real object than the assumed in the models can lead to such a difference. The magnetic field structure in both galaxies is difficult to quantify with respect to those found in simulations because of lack of enough spatial resolution in observations.

## Conclusions

I present a global model of the cosmic ray driven dynamo in a dwarf galaxy. The model consists of (1) exploding SNe which supply the cosmic ray energy input and are distributed according to the local density of gas, (2) seeding the dynamo by randomly oriented dipoles injected with first bursts of SNe, (3) the “modified isothermal sphere” and Burkert’s dark matter profiles and (4) the ISM resistivity. The main findings of this thesis are:

- The cosmic-ray driven dynamo operating in a dwarf galaxy can amplify the magnetic fields exponentially in time. Besides the total magnetic energy also the regular component,  $B_\phi$  is significantly amplified.
- The magnetic field is amplified for all models with different DM profile, ISM temperature, supernova modulation if only  $v_{\text{rot}} \geq 40 \text{ km s}^{-1}$ . For slower rotating models only few of them can effectively amplify the magnetic field, but no simple relation has been found. The rotation speed set to  $20 \text{ km s}^{-1}$  seems to be not enough to initiate a dynamo action.
- The  $e$ -folding time of the azimuthal magnetic flux is 1 Gyr for models with  $v_{\text{rot}} = 40 \text{ km s}^{-1}$  and 400 Myr for the fastest rotators. As well the magnetic energy is amplified and its the growth rate is about 2 or 3 times faster.
- There is no dependence of the magnetic field growth rate on the duration of the quiescent state in the supernovae modulation. Such relation has been previously reported by Hanasz et al. (2009a) and Siejkowski et al. (2010) in the shearing box simulations, but in the global simulation seems to be not applicable.
- The dynamo efficiency do not depends on the shearing rate caused by the differential rotation. Similar result has been found by Siejkowski et al. (2010), but addi-

tionally they indicate that the shear needs to be present, i.e. the rotation curve can not be for a solid body.

- Only the fastest rotating models reach the dynamical equilibrium state between magnetic fields and thermal gas. The cosmic ray pressure is about 10 times higher than the thermal gas pressure. This seem to be due to the lower values of the cosmic ray diffusion coefficients than the realistic values. This issue has been reported also by Snodin et al. (2006) and Hanasz et al. (2009a).
- The dominant component of the magnetic field amplified by the dynamo is the toroidal one. The magnetic field configuration do not show any spiral structure as well as the vertical component is not developed. The magnetic field have axisymmetric symmetry in the disk plane and quadrupolar in the edge-on view.
- For slow rotating models, where the dynamo do not operate effectively, the vertical structure is dipolar. The azimuthal flux is much stronger above and below the galactic disk than this found in the midplane.
- A relation between the rotation speed and the final magnetic field strength is found showing that  $B \propto v_{\text{rot}}^\alpha$ , where  $\alpha$  can be about 9 and 10 for models where the ISM temperature is 6000 K and 8000 K, respectively. For colder ISM,  $T = 4000$  K the index is 4.5, but the result is burdened with considerable uncertainty.
- The magnetic fields observed in NGC 6822 and LMC can be explained by the operation of the cosmic ray driven dynamo. The other objects however seem to be very exceptional mainly because of their extremely high star formation rates and disturbed kinematics.

This thesis shows that the magnetic field in quiet objects can be explained in terms of the cosmic ray driven dynamo. The vertical and azimuthal configuration of the amplified magnetic field is comparable to those found in observations. The presented discussion indicates a possible relation between the growth rate of the magnetic field and the rotation speed of the galactic disk. The global model of the dwarf galaxy provide a reliable framework for further investigation of magnetic dynamo as well as other processes related to the magnetic field evolution and cosmic rays in dwarf galaxies.

## Star formation rate and supernova rate

Star formation rate (SFR) is a quantity which informs about the amount of mass converting into the newborn stars. Often a derivative quantity is used, namely the surface density of SFR,  $\Sigma\text{SFR}$ . Both quantities are easy to derive from observations and can be an input parameter for modelling. A quantity which obviously depends on the SFR is the supernova rate, which informs about the number of stars exploding as a supernova. In the cosmic-ray driven dynamo model a key parameter is the surface density of frequency of supernova explosions defined as follows:

$$f_{\text{SN}} = \frac{v_{\text{SN}}}{A}, \quad (\text{A.1})$$

where,  $v_{\text{SN}}$  is the number of SNe explosions which occurs per year in the area  $A$ . To find the relation between  $f_{\text{SN}}$  and  $\Sigma\text{SFR}$  or  $N_{\text{SN}}/t$  and SFR one can use the initial mass function. The initial mass function (IMF) is an empirical function that describes the mass distribution (the histogram of stellar masses) of a population of stars in terms of their theoretical initial mass. The IMF underlays both the SFR and SNR and often is approximated by:

$$\Psi(M) = kM^{-\gamma}, \quad (\text{A.2})$$

where,  $M$  is the mass express in solar mass unit,  $k$  and  $\gamma$  are constants. The number of stars formed which have mass between  $M_{\text{min}}$  and  $M_{\text{max}}$  is:

$$N_* = \int_{M_{\text{min}}}^{M_{\text{max}}} \Psi(M) dM, \quad (\text{A.3})$$

and the amount of mass converted into stars (SFR) is:

MODELS OF THE IMF								
Ref.	$\gamma$	$M_{\min}$	$M_{\max}$	$S_{\min}$	$S_{\max}$	$f_M$	$\bar{M}$	$\tilde{M}$
Condon (1992)	2.5	5	100	8	100	0.73	17.6	19.4
Kennicutt (1998)	2.35	0.1	100	8	100	0.13	18.7	21.6

Table A.1: The first column shows the reference for the model. All masses are given in  $M_{\odot}$ .  $\bar{M}$  and  $\tilde{M}$  are the mean and median mass, respectively.

$$\text{SFR} = \int_{M_{\min}}^{M_{\max}} M\Psi(M)dM, \quad (\text{A.4})$$

Assuming that  $S_{\min}$  and  $S_{\max}$  are the mass limits for stars which explode as supernovae, we can find what mass fraction  $f_M$  is “converted” into the SNe, by:

$$f_M = \frac{\int_{S_{\min}}^{S_{\max}} M\Psi(M)dM}{\int_{M_{\min}}^{M_{\max}} M\Psi(M)dM} \quad (\text{A.5})$$

To find a representative mass of a star which ends as a supernova, one can calculate the mean mass:

$$\bar{M}_{\text{SN}} = \frac{\int_{S_{\min}}^{S_{\max}} M\Psi(M)dM}{\int_{S_{\min}}^{S_{\max}} \Psi(M)dM}, \quad (\text{A.6})$$

or the median mass:

$$\tilde{M}_{\text{SN}} = \frac{\int_{S_{\min}}^{S_{\max}} M\Psi(M)dM}{\int_{S_{\min}}^{S_{\max}} \Psi(M)dM}, \quad (\text{A.7})$$

Knowing the SFR from observation now we can easily find the corresponding SNR, i.e.:

$$v_{\text{SN}} = \text{SFR } f_M / M_{\text{SN}}, \quad (\text{A.8})$$

where  $M_{\text{SN}}$  is the mean (Eq. A.6) or median (Eq. A.7) mass of star which explodes of supernova. We can find the  $f_{\text{SN}}$  by substituting the SFR by  $\Sigma\text{SFR}$ :

$$f_{\text{SN}} = \Sigma\text{SFR } f_M / M_{\text{SN}}. \quad (\text{A.9})$$

To close this equation one need to assume the values of mass limits for stars and SNe and the IMF index  $\gamma$ . The constant  $k$  reduces from both of the above the equations, so in this case is no need to find it. These parameters can be find in the literature, but they vary from model to model. The two commonly used IMF models and the resulting  $f_M$ ,  $\bar{M}$  and  $\tilde{M}$  are shown in Table A.1. The relation between  $f_{\text{SN}}$  and the  $\Sigma\text{SFR}$  for described IMF models is shown in Figure A.1.

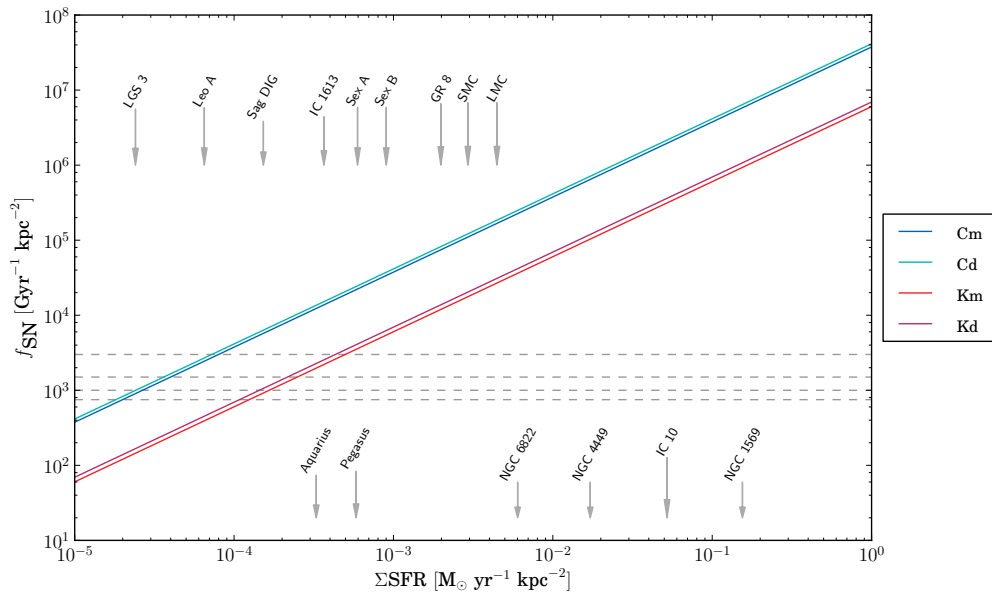


Figure A.1: Relation between  $\Sigma\text{SFR}$  (an observed quantity) and the  $f_{\text{SN}}$  (a parameter of the CR driven dynamo). The Cm and Cd lines show the relation described by Eq. (A.9) for IMF parameters from Condon (1992), where  $M_{\text{SN}}$  is defined as the mean and median SN mass, respectively. Analogously for Km and Kd lines, which uses the IMF model from Kennicutt (1998). The horizontal dashed lines show the  $f_{\text{SN}}$  values used in the dwarf galaxy simulations presented in this work. They mark the following values, from top: 3000, 1500, 1000 and 750  $\text{kpc}^{-2} \text{Gyr}^{-1}$ . The arrows show the observed  $\Sigma\text{SFR}$  values for particular dwarf galaxies taken from Chyży et al. (2011).

# Bibliography

- Alted, F., Vilata, I., et al. 2002–, PyTables: Hierarchical Datasets in Python, <http://www.pytables.org>
- Ashour-Abdalla, M., El-Alaoui, M., Goldstein, M. L., et al. 2011, *Nature Physics*, 7, 360
- Balbus, S. A. 2009, *Scholarpedia*, 4, 2409
- Beck, R. 1982, *A&A*, 106, 121
- Beck, R. 2005, in *The Magnetized Plasma in Galaxy Evolution*, ed. K. T. Chyzy, K. Otmianowska-Mazur, M. Soida, & R.-J. Dettmar, 193–200
- Beck, R. 2007, *Scholarpedia*, 2, 2411
- Beck, R., Fletcher, A., Shukurov, A., et al. 2005, *A&A*, 444, 739
- Beck, R. & Hoernes, P. 1996, *Nature*, 379, 47
- Belokurov, V., Zucker, D. B., Evans, N. W., et al. 2007, *ApJ*, 654, 897
- Bernet, M. L., Miniati, F., Lilly, S. J., Kronberg, P. P., & Dessauges-Zavadsky, M. 2008, *Nature*, 454, 302
- Bertone, S., Vogt, C., & Enßlin, T. 2006, *MNRAS*, 370, 319
- Binney, J. & Tremaine, S. 2008, *Galactic Dynamics: Second Edition*, ed. Binney, J. & Tremaine, S. (Princeton University Press)
- Biskamp, D. 1993, *Nonlinear magnetohydrodynamics*
- Blanton, M. R., Hogg, D. W., & SDSS Collaboration. 2002, in *Bulletin of the American Astronomical Society*, Vol. 34, American Astronomical Society Meeting Abstracts #200, 679
- Blumenthal, G. R., Faber, S. M., Primack, J. R., & Rees, M. J. 1984, *Nature*, 311, 517
- Boulares, A. & Cox, D. P. 1990, *ApJ*, 365, 544

- Brandenburg, A., Donner, K. J., Moss, D., et al. 1993, *A&A*, 271, 36
- Brandenburg, A. & Subramanian, K. 2005, *Phys. Rep.*, 417, 1
- Burkert, A. 1995, *ApJ*, 447, L25
- Chapman, B., Jost, G., & Pas, R. v. d. 2007, *Using OpenMP: Portable Shared Memory Parallel Programming (Scientific and Engineering Computation)* (The MIT Press)
- Chyży, K. T., Beck, R., Kohle, S., Klein, U., & Urbanik, M. 2000, *A&A*, 355, 128
- Chyży, K. T., Knapik, J., Bomans, D. J., et al. 2003, *A&A*, 405, 513
- Chyży, K. T., Weżgowiec, M., Beck, R., & Bomans, D. J. 2011, *A&A*, 529, A94
- Condon, J. J. 1992, *ARA&A*, 30, 575
- Courant, R., Friedrichs, K., & Lewy, H. 1967, *IBM Journal of Research and Development*, 11, 215
- Davis, Jr., L. & Greenstein, J. L. 1951, *ApJ*, 114, 206
- Del Zanna, L., Bucciantini, N., & Londrillo, P. 2003, *A&A*, 400, 397
- Dorfi, E. A. 2000, *Ap&SS*, 272, 227
- Drzazga, R. T., Chyży, K. T., Jurusik, W., & Wiórkiewicz, K. 2011, *A&A*, 533, A22
- Dubois, Y. & Teyssier, R. 2010, *A&A*, 523, A72
- Eddy, J. A. 1976, *Science*, 192, 1189
- Ferrière, K. M. 2001, *Reviews of Modern Physics*, 73, 1031
- Fletcher, A., Beck, R., Shukurov, A., Berkhuijsen, E. M., & Horellou, C. 2011, *MNRAS*, 412, 2396
- Foukal, P. V. 2004, *Solar Astrophysics*, 2nd, Revised Edition
- Frick, P., Stepanov, R., Shukurov, A., & Sokoloff, D. 2001, *MNRAS*, 325, 649
- Gabriel, E., Fagg, G. E., Bosilca, G., et al. 2004, in *Proceedings, 11th European PVM/MPI Users' Group Meeting, Budapest, Hungary*, 97–104
- Gaensler, B. M., Haverkorn, M., Staveley-Smith, L., et al. 2005, *Science*, 307, 1610
- Giacalone, J. & Jokipii, J. R. 1999, *ApJ*, 520, 204
- Godunov, S. K. 1959, *Math. Sbornik*, 47, 271

- Goedbloed, J. P. H. & Poedts, S. 2004, Principles of Magnetohydrodynamics, ed. Goedbloed, J. P. H. & Poedts, S.
- Governato, F., Brook, C., Mayer, L., et al. 2010, *Nature*, 463, 203
- Grebel, E. K. 2001, *Astrophysics and Space Science Supplement*, 277, 231
- Gressel, O., Elstner, D., Ziegler, U., & Rüdiger, G. 2008, *A&A*, 486, L35
- Griffiths, D. J. 1999, *Introduction to Electrodynamics (3rd Edition)*, 3rd edn. (Benjamin Cummings)
- Hale, G. E. 1908, *ApJ*, 28, 315
- Han, J. L., Manchester, R. N., Lyne, A. G., Qiao, G. J., & van Straten, W. 2006, *ApJ*, 642, 868
- Hanasz, M., Kowal, G., Otmianowska-Mazur, K., & Lesch, H. 2004, *ApJ*, 605, L33
- Hanasz, M. & Lesch, H. 2003, *A&A*, 412, 331
- Hanasz, M., Otmianowska-Mazur, K., Kowal, G., & Lesch, H. 2006, *Astronomische Nachrichten*, 327, 469
- Hanasz, M., Otmianowska-Mazur, K., Kowal, G., & Lesch, H. 2009a, *A&A*, 498, 335
- Hanasz, M., Wóltański, D., & Kowalik, K. 2009b, *ApJ*, 706, L155
- Harten, A., Lax, P. D., & Van Leer, B. 1983, *SIAM Review*, 25, 35
- Heesen, V., Krause, M., Beck, R., & Dettmar, R.-J. 2009, *A&A*, 506, 1123
- Heiles, C. & Crutcher, R. 2005, in *Lecture Notes in Physics*, Berlin Springer Verlag, Vol. 664, *Cosmic Magnetic Fields*, ed. R. Wielebinski & R. Beck, 137
- Hunter, D. A., van Woerden, H., & Gallagher, J. S. 1999, *AJ*, 118, 2184
- Hunter, J. D. 2007, *Computing In Science & Engineering*, 9, 90
- Jackson, J. D. 1975, *Classical electrodynamics*
- Joos, M., Hennebelle, P., & Ciardi, A. 2012, *A&A*, 543, A128
- Kennicutt, Jr., R. C. 1989, *ApJ*, 344, 685
- Kennicutt, Jr., R. C. 1998, in *Astronomical Society of the Pacific Conference Series*, Vol. 142, *The Stellar Initial Mass Function (38th Herstonceux Conference)*, ed. G. Gilmore & D. Howell, 1
- Kepley, A. A., Mühle, S., Everett, J., et al. 2010, *ApJ*, 712, 536

- Klein, U., Haynes, R. F., Wielebinski, R., & Meinert, D. 1993, *A&A*, 271, 402
- Klein, U., Hummel, E., Bomans, D. J., & Hopp, U. 1996, *A&A*, 313, 396
- Knapik, J., Soida, M., Dettmar, R.-J., Beck, R., & Urbanik, M. 2000, *A&A*, 362, 910
- Kowal, G., Falceta-Gonçalves, D. A., & Lazarian, A. 2011, *New Journal of Physics*, 13, 053001
- Kowal, G., Lazarian, A., Vishniac, E. T., & Otmianowska-Mazur, K. 2009, *ApJ*, 700, 63
- Kraus, J. D. 1966, *Radio astronomy*
- Krause, M. 2003, *Acta Astronomica Sinica*, 44, 123
- Krause, M. 2009, in *Revista Mexicana de Astronomía y Astrofísica*, vol. 27, Vol. 36, *Revista Mexicana de Astronomía y Astrofísica Conference Series*, 25–29
- Krause, M., Beck, R., & Hummel, E. 1989a, *A&A*, 217, 17
- Krause, M., Hummel, E., & Beck, R. 1989b, *A&A*, 217, 4
- Kravtsov, A. 2010, *Advances in Astronomy*, 2010
- Kronberg, P. P., Lesch, H., & Hopp, U. 1999, *ApJ*, 511, 56
- Kulpa-Dybeł, K., Otmianowska-Mazur, K., Kulesza-Żydzik, B., et al. 2011, *ApJ*, 733, L18
- Larmor, J. 1919, *Report of the British Association for the Advancement of Science*, 87th Meeting, 159
- Lazarian, A. & Cho, J. 2005, in *Astronomical Society of the Pacific Conference Series*, Vol. 343, *Astronomical Polarimetry: Current Status and Future Directions*, ed. A. Adamson, C. Aspin, C. Davis, & T. Fujiyoshi, 333
- Lazarian, A. & Vishniac, E. T. 1999, *ApJ*, 517, 700
- Leitherer, C., Robert, C., & Drissen, L. 1992, *ApJ*, 401, 596
- LeVeque, R. J. 2002, *Finite-Volume Methods for Hyperbolic Problems* (Cambridge University Press)
- Li, H.-B. & Henning, T. 2011, *Nature*, 479, 499
- Li, L.-X. 2003, *Phys. Rev. D*, 68, 024022
- Łokas, E. L., Kazantzidis, S., & Mayer, L. 2012, *ApJ*, 751, L15
- Londrillo, P. & Del Zanna, L. 2000, *ApJ*, 530, 508

- Longair, M. S. 2010, High Energy Astrophysics
- Mac Low, M.-M. & Ferrara, A. 1999, ApJ, 513, 142
- Manchester, R. N. 1974, ApJ, 188, 637
- McKee, C. F. & Ostriker, E. C. 2007, ARA&A, 45, 565
- Mignone, A. 2007, Journal of Computational Physics, 225, 1427
- Mo, H., van den Bosch, F. C., & White, S. 2010, Galaxy Formation and Evolution, ed. Mo, H., van den Bosch, F. C., & White, S.
- Moffatt, H. K. 1978, Magnetic field generation in electrically conducting fluids
- Moss, D. & Shukurov, A. 1996, MNRAS, 279, 229
- Nalewajko, K., Giannios, D., Begelman, M. C., Uzdensky, D. A., & Sikora, M. 2011, MNRAS, 413, 333
- Navarro, J. F., Frenk, C. S., & White, S. D. M. 1996, ApJ, 462, 563
- Niklas, S. 1995, PhD thesis, PhD Thesis, Univ. Bonn, (1995)
- O’C. Drury, L. 2012, ArXiv e-prints
- Oliphant, T. E. 2007, Computing in Science & Engineering, 9, 10
- Otmianowska-Mazur, K., Kulpa-Dybeł, K., Kulesza-Żydzik, B., Siejkowski, H., & Kowal, G. 2011, in IAU Symposium, Vol. 274, IAU Symposium, ed. A. Bonanno, E. de Gouveia Dal Pino, & A. G. Kosovichev, 381–384
- Otmianowska-Mazur, K., Soida, M., Kulesza-Żydzik, B., Hanasz, M., & Kowal, G. 2009, ApJ, 693, 1
- Ouyed, R. & Pudritz, R. E. 1997a, ApJ, 482, 712
- Ouyed, R. & Pudritz, R. E. 1997b, ApJ, 484, 794
- Pacholczyk, A. G. 1970, Radio astrophysics. Nonthermal processes in galactic and extragalactic sources
- Parker, E. N. 1957, J. Geophys. Res., 62, 509
- Parker, E. N. 1965, ApJ, 142, 584
- Parker, E. N. 1971, ApJ, 163, 255
- Parker, E. N. 1992, ApJ, 401, 137

- Petschek, H. E. 1964, NASA Special Publication, 50, 425
- Priest, E. & Forbes, T. 2000, Magnetic Reconnection
- Randall, C. E., Harvey, V. L., Manney, G. L., et al. 2005, *Geophys. Res. Lett.*, 32, 5802
- Recchi, S., Hensler, G., Angeretti, L., & Matteucci, F. 2006, *A&A*, 445, 875
- Rüdiger, G. & Hollerbach, R. 2004, *The magnetic universe : geophysical and astrophysical dynamo theory*
- Ruzmaikin, A., Sokolov, D., & Shukurov, A. 1988, *Nature*, 336, 341
- Rybicki, G. B. & Lightman, A. P. 1986, *Radiative Processes in Astrophysics*
- Ryu, D., Kim, J., Hong, S. S., & Jones, T. W. 2003, *ApJ*, 589, 338
- Ryu, D., Schleicher, D. R. G., Treumann, R. A., Tsagas, C. G., & Widrow, L. M. 2012, *Space Sci. Rev.*, 166, 1
- Scannapieco, E. & Brüggén, M. 2010, *MNRAS*, 405, 1634
- Schlickeiser, R. & Lerche, I. 1985, *A&A*, 151, 151
- Schmidt, M. 1959, *ApJ*, 129, 243
- Shukurov, A. & Sokoloff, D. 2008, in *Les Houches, Vol. 88, Dynamos*, ed. P. Cardin & L. Cugliandolo (Elsevier), 251 – 299
- Siejkowski, H., Soida, M., Otmianowska-Mazur, K., Hanasz, M., & Bomans, D. J. 2010, *A&A*, 510, A97
- Snodin, A. P., Brandenburg, A., Mee, A. J., & Shukurov, A. 2006, *MNRAS*, 373, 643
- Soida, M., Beck, R., Urbanik, M., & Braine, J. 2002, *A&A*, 394, 47
- Soida, M., Krause, M., Dettmar, R.-J., & Urbanik, M. 2011, *A&A*, 531, A127
- Sokoloff, D., Shukurov, A., & Krause, M. 1992, *A&A*, 264, 396
- Sparke, L. S. & Gallagher, III, J. S. 2007, *Galaxies in the Universe: An Introduction* (Cambridge University Press)
- Stepanov, R., Shukurov, A., Fletcher, A., et al. 2012, *ArXiv e-prints*
- Stil, J. M. & Israel, F. P. 2002, *A&A*, 392, 473
- Strong, A. W., Moskalenko, I. V., & Ptuskin, V. S. 2007, *Annual Review of Nuclear and Particle Science*, 57, 285

- Sun, X. H., Reich, W., Waelkens, A., & Enßlin, T. A. 2008, *A&A*, 477, 573
- Sweet, P. A. 1958, in *IAU Symposium, Vol. 6, Electromagnetic Phenomena in Cosmical Physics*, ed. B. Lehnert, 123
- Valdez-Gutiérrez, M., Rosado, M., Puerari, I., et al. 2002, *AJ*, 124, 3157
- Vishniac, E. T. & Cho, J. 2001, *ApJ*, 550, 752
- Wang, H.-H., Klessen, R. S., Dullemond, C. P., van den Bosch, F. C., & Fuchs, B. 2010, *MNRAS*, 407, 705
- Wei, Y., Fraenz, M., Dubinin, E., et al. 2012, *Journal of Geophysical Research (Space Physics)*, 117, 3208
- Weldrake, D. T. F., de Blok, W. J. G., & Walter, F. 2003, *MNRAS*, 340, 12
- Widrow, L. M. 2002, *Reviews of Modern Physics*, 74, 775
- Wielebinski, R. & Beck, R., eds. 2005, *Lecture Notes in Physics*, Berlin Springer Verlag, Vol. 664, *Cosmic Magnetic Fields*
- Wilcots, E. M. & Miller, B. W. 1998, *AJ*, 116, 2363
- Woo, J., Courteau, S., & Dekel, A. 2008, *MNRAS*, 390, 1453
- Zweibel, E. G. & Yamada, M. 2009, *ARA&A*, 47, 291